FROM ANTARCTIC SEA ICE UNLEASHING GLACIERS TO ALASKAN ICEFALLS RELEASING OGIVES: INVESTIGATIONS OF GLACIER PROCESSES USING REMOTE SENSING, FIELD DATA, AND NUMERICAL MODELING

by

NAOMI ELAINE OCHWAT

B.A., University of Colorado, Boulder, 2016

M.Sc., University of Calgary, Canada, 2019

A thesis submitted to the

Faculty of the Graduate School of the

University of Colorado in partial fulfillment

of the requirement for the degree of

Doctor of Philosophy

Department of Geology

2024

Committee Members:

Dr. Theodore Scambos

Dr. Robert S. Anderson

Dr. Etienne Berthier

Dr. Waleed Abdalati

Dr. Bradley Markle

Ochwat, Naomi Elaine (Ph.D., Geological Sciences)
From Antarctic sea ice unleashing glaciers to Alaskan icefalls releasing ogives: investigations of glacier processes using remote sensing, field data, and numerical modeling

Thesis directed by senior research scientist Dr. Theodore Scambos and Distinguished Professor Robert S. Anderson

Earth's glaciers, ice sheets, and ice shelves are changing significantly due to our warming climate. Glaciers that drain the Antarctic Ice Sheet have become more susceptible to rapid speed-up and retreat, especially once their floating portions become unstable or collapse. The world's mountain glaciers are experiencing substantial melting and changing dynamics. Yet, the cryosphere is riddled with unsolved instabilities, unexplored tipping points, and unresolved ice-dynamic mysteries. This dissertation presents three studies that address three key topics in glaciology: drivers of ice shelf/fast-ice collapse, causes of rapid tidewater glacier retreat, and controls on mountain glacier waves called 'ogives.'

First, in Chapter 2, I analyze and discuss the causes of the break-up of the decade-old Larsen B fast-ice that occurred in mid-January 2022. My study uses a plethora of satellite remote-sensing datasets, including optical imagery (primarily Landsat, MODIS, Sentinel-2, Worldview), synthetic aperture radar data (Sentinel-1), passive microwave data (AMSR-E/2), laser altimetry data (ICESat-2), aerial photography, and Worldview-derived digital elevation models (DEMs). I include ERA-5 and WaveWatch-III climate and ocean reanalysis data, and ice velocity measurements from in-situ GNSS data. By synthesizing all of these datasets, I diagnose the drivers of the fast-ice collapse and the initial glacier responses. Although 2022 was an anomalously warm year, the primary cause of the collapse was a large oceanic swell that broke up the fast-ice, the timing of which was associated with a corridor of low sea ice concentration in the northwestern Weddell Sea. Following the fast-ice break-out, the tributary glaciers and their ice tongues that earlier flowed into the embayment responded immediately. Crane, Hektoria, and Green Glacier lost their 300+ meter-thick floating ice tongues over the course of several weeks and then began calving at their grounding lines. Within a year, Crane Glacier accelerated by 50% and retreated 11 km.

In Chapter 3, I investigate Hektoria Glacier's unprecedented rapid retreat and extended dynamical response to the break-out. For this analysis, I include ASTER and SPOT-5 HRS stereo-image-derived DEMs, ICEBridge radar data, and POLENET seismological data. I find that Hektoria and Green Glaciers accelerated by 600%, increased their thinning rate by 30-fold and Hektoria Glacier ultimately retreated by 25 km, 10 km of which was over a lightly grounded "ice plain" (an area of bedrock with a very low slope). I propose that the geometry of the ice plain preconditioned the thinning glacier for a rapid buoyancy-driven retreat. Until now, this process has not been recorded in the modern day glaciological record.

In Chapter 4, I investigate a set of ogives formed on the Gilkey Glacier, Alaska. Ogives are topographic wave trains that can form where an icefall connects to a valley glacier below. I employ a combination of remote sensing and in-situ observations, such as the ITS_LIVE velocity dataset, GNSS station data, Worldview imagery and DEMs, and Landsat imagery, to characteristize ice plateau-icefall-glacier systems. Those constrain parameter values in a finite difference numerical model that simulates ogive formation by calculating ice thickness changes resulting from varying mass balance and/or ice velocity. I use this model to test two main ogive formation processes using both an idealized glacier and the Gilkey Glacier. My results suggest that the most plausible explanation for ogive formation is a steady icefall velocity encountering a receiving glacier with significant seasonal velocity variation. During the summer, the lower glacier accelerates, inducing thinning at the base of the icefall. As the glacier decelerates in winter, it induces thickening at the base of the icefall, thus resulting in annual waves (aka 'ogives'). Taken together, all three studies in this dissertation emphasize the importance of curiosity-driven science and the innate pursuit of knowledge.

DEDICATION

I dedicate this work to all of the dogs in the world. Every dog I have had the pleasure of interacting with, whose cuteness, unconditional love, and playfulness has brought much joy to my life, especially during my PhD. To my childhood dog "Doctor Zeus" and my dog during college Matilda "Mattie" Bear. And to the dogs that I've been lucky to cross paths with: Odi, Artemis, Baxley, June, Kat, Nilla, Mighty, Otis, Farley, Annie, Penny, Jesse, Henry, Reese, the affectionate dogs on trails and in friends' homes, the street dogs of Chilé, and the endless dogs on the internet.

ACKNOWLEDGEMENTS

Growing up, I never knew I could be a scientist, and yet here I am. Therefore, the work presented in this dissertation would not have been possible without the support and guidance of many individuals, not only throughout the last 3.5 years, but also for the sinuous decade(s) prior.

I would first like to express my immense gratitude for my advisors and committee. I am not sure there are words to describe the appreciation I have for my advisor Ted Scambos, who took me under his mentorship after pestering him for a job after my master's degree. Not only did he ignite my love of remote sensing and Antarctic glaciology, but he also taught me how to think about, address, and tell the story of glaciological problems. He supported me through funding and scientific inquiry, and also provided opportunities that far surpassed my highest expectations. I am profoundly thankful for my advisor Bob Anderson, who has been a mentor since my first days as a geology undergrad. He inspired my initial interest in glaciology and has been persistently at my side while I navigated the fluctuations and uncertainties regarding my career and life direction. And, it was in his lessons that I learned how to quantitatively describe and understand Earth's processes through calculus. I feel so grateful to have been mentored by both of these truly phenomenal people.

During my PhD there have been a number of other important people that have directed my research or impacted my scientific aspirations. I must thank my committee members for their unrelenting support through this process and for the important roles they played on my development as a scientist. Alison Banwell, for consistently providing enthusiasm and interest in all of my research endeavours and for her manuscript comments that been some of the most thoughtful I have ever seen. Etienne Berthier for demonstrating the true meaning of international collaboration by providing continuous support and guidance and for the warm welcome I received in France. Brad Markle for first introducing me to the Juneau Icefield back at AGU in 2018 and for making my dreams of collecting field data on ogives with JIRP possible. And Waleed Abdalati for asking essential questions on the importance of my scientific objectives.

I am deeply appreciative of several people outside of my committee. Yoram Terleth for being on board with taking our ogive project to the next level and being an integral part in making that happen. Martin Truffer for supporting Yoram and I's endeavour and asking the question in the first place. Anna Crawford for providing hundreds of hours of her time to teach me everything she knows about modelling and for being an exceptional role model to look up to. I would like to thank the TARSAN science team for the weekly meetings that I attended for a significant time during my PhD that provided me with a sense of community and support. The TARSAN field team 2022 for introducing me to collaborative Antarctic field science, and Emelie Madhavian for being the best tent-mate ever. I am sincerely grateful for Erin Pettit's inspiration and leadership. Before I even knew about glaciology, her Radiolab episode on "supercool ice" fueled my interest in studying ice. I am grateful to have worked with her on TARSAN. I am forever grateful for Professor Shemin Ge, who was the first to introduce me to geology and research as a career path; during my first year as an undergrad at CU when debating to switch my major from business to geology she said "yes, you can do it!" I have to also thank Dr. Lon Abbott for not letting me drop out of geology after failing Chem 101 my second year!

I am grateful for my friends and colleaugues that have had unwavering support, from the important discussions revolving around life career choices and academia, to getting me out of the house for activities, to listening and grounding me throughout this journey: Jasmine Vidrio, Ashley Moore, Mallory Larson, Julia Shates, Robert Kelleher, Tasha Snow, Elisa McGhee, Sierra Melton, Meghan Sharp, Michelle MacLennan, Lilo Margonari, Noah Hoffman, Annika

Horlings, Nicole Varner, my dad Tom Ochwat, my grandma KT, my grandma Mary, my late grandpa Bob, my boyfriend Franco Saravalli, and all of my extended family.

I have a special thanks to the JIRP organization and community, for providing me with an opportunity of a lifetime and supporting my aspirations to conduct fieldwork. I thank all of the faculty, field staff, and especially the students – “Trench Camp Forever!”

Thank you to CIRES Travel, CIRES IT, and Dawn Williams for their support in making everything happen. And thank you to CIRES CEEE, Anne Gold and Katie Boyd, for providing an opportunity to work on climate change education programs. Thank you to Kara Bajdas in Geological Sciences. Thank you to the USAP program for a successful Thwaites field season in 2022 and to the Instituto Antártico Argentino, Sebastian Marinsek, and Argentinian Air Force for a successful field season at Crane Glacier 2023.

Thank you to all who have contributed in any way shape or form to this work and my personal journey getting here.

Lastly, this work was supported by the NASA ROSES Cryosphere award, USGS Landsat Science Team award, NSF ITGC TARSAN award, and the CIRES Innovative Research Proposal Award.

Table of Contents

CHAPTER 1 .... **1**

1 Introduction **1**

2 Ice-Ocean systems **1**

2.1 Antarctica 1
2.2 Larsen B Embayment 3

3 Land-Ice systems **5**

4 Tying it all together **7**

CHAPTER 2 .... **8**

Abstract **8**

1 Introduction **9**

2 Study area **11**

3 Data and Methods **13**

3.1 Reanalysis Data 13
3.2 Satellite Data 14

4 Results **19**

4.1 Multi-year fast ice in the Larsen B embayment 19
4.2 Potential Attributions of the 2021-2022 Fast Ice Breakout 22
4.3 Initial glacier response to fast ice break-out 28

5 Discussion **37**

5.1 Meteorological Conditions and Modes of Atmospheric Variability 39
5.2 The fast ice break-out event 42
5.3 The initial glacier response 43

6 Conclusions **47**

Acknowledgements **49**

Author Contributions **49**

Data Availability **50**

CHAPTER 3 .... **51**

Abstract **51**

1 Introduction **51**

2 Results **55**

2.1 Assessment of the phases of the 2022-2023 retreat 55
2.2 Grounding line constraints from elevation profiles 59
2.3 Grounding line constraints from surface texture and calving style 60
2.4 Glacier earthquakes 61
2.5 Glacier response following the fast ice break-out 62

3 Discussion **63**

3.1 Grounding Line Controversy 63
3.2 Record pace of Hektoria Glacier retreat across the ice plain 2022-2023 67
3.3 Broader implications 68

4 Methods **69**

4.1 Satellite image time-series for morphological evolution 69
4.2 Image-derived elevation and velocity changes 70
4.3 Ice flow speeds 71
4.4 Laser Altimetry 72
4.5 Airborne radar profiles 72
4.6 Glacial-Earthquake Event-Detection, Location, and Waveform Modeling. 73

Acknowledgements 74

Author contributions 74

CHAPTER 4 75

1 Introduction 75

2 Study Area 77

3 Methods 78
3.1 Satellite remote sensing 79
3.2 Field data collection 80
3.3 Modeling ogives 83

4 Results 86
4.1 Gilkey Glacier characteristics from Worldview-derived DEMs, velocity data, and math! 86
4.2 Icefall and ogive location analysis 91
4.3 Modeling results 92

5 Discussion 101
5.1 Characterization of Gilkey Glacier 101
5.2 Theories of ogive formation 102
5.3 Why do ogives not form under all icefalls? 106

6 Conclusions 108
Acknowledgements 108
Data and materials availability 109

CHAPTER 5 110

1 Implications of the Larsen B fast-ice and tributary glacier dynamics 110

2 Broader impact of ice dynamics of ogives in Alaska 113

3 Commonalities between ice dynamics at the Larsen B embayment and ogives in Alaskan valley glaciers 116

REFERENCES 118

APPENDIX I 137

APPENDIX II 147

TABLES

Table 4.1: Summary of velocities in key sections of the Gilkey Glacier..................................... 97

Table A1-S1: Date and sensor of Worldview images used for this study. 137

Table A2-S2: Event times, estimate force magnitudes, and directions for GEQs..................... 154

FIGURES

Chapter 2

Figure 2.1: Overview of Larsen B embayment before and after 2022 fast-ice break-out 12
Figure 2.2: Scar Inlet Ice Shelf ice flow speeds from AMIGOS GPS from 2010 to 2017........... 21
Figure 2.3: ERA-5 surface air temperature anomalies around the Antarctic Peninsula. 23
Figure 2.4: ERA-5 analysis of an atmopsheric river event. 24
Figure 2.5: Cumulative melt days derived from AMSR-E/2 passive microwave melt data......... 25
Figure 2.6: Pack sea ice concentration and distribution map on 19 January 2022 27
Figure 2.7: ERA-5 significant wave height and peak period 28
Figure 2.8: Crane and Hektoria Glacier termini positions and grounding lines 31
Figure 2.9: Monthly averaged ice flow speeds along the IceBridge flight centerlines................. 34
Figure 2.10: Crane Glacier near-centerline elevation changes through time 35
Figure 2.11: Hektoria and Green Glacier system elevation changes through time 37
Figure 2.12: Chronology of events from 2001-2023 of the Larsen B embayment. 39

Chapter 3

Figure 3.1: The retreat of Hektoria and Green Glaciers 2022 55
Figure 3.2: Hektoria Glacier retreat rates and area loss from Feb 2022 until Aug 2023.............. 56
Figure 3.3: Elevation and velocity changes of Hektoria and Green Glacier 2017-2022 57
Figure 3.4: Elevation and velocity changes of Hektoria and Green Glacier 2011-2022. 59
Figure 3.5 Schematic of an idealized glacier and Hektoria Glacier’s rapid retreat 64

Chapter 4

Figure 4.1: Gilkey Glacier region, Alaska and ogive elevation and wavelengths. 77
Figure 4.2: Ice thickness of the Gilkey Glacier from four different sources 89
Figure 4.3: Velocity estimates from satellite remote sensing and in-situ data 90
Figure 4.4: Timelapse camera velocities of the lower Vaughan Lewis Icefall. 91
Figure 4.5: Map of Juneau Icefield icefalls and glaciers and velocities. 92
Figure 4.6: Parameter values for idealized glacier surface mass balance 94
Figure 4.7: Idealized glacier model runs depicting final ice thicknesses 95
Figure 4.8: Parameter values for idealized glacier velocity 96
Figure 4.9: Paramter values for the Gilkey Glacier model simulation 99
Figure 4.10: Gilkey Glacier model runs depicting final ice thicknesses 100

Appendix I

Figure A1-S1: ICESat-2 elevation of HGE floating tongue.. 138
Figure A1-S2: Freeboard of tabular icebergs in October 2022.. 139
Figure A1-S3: Precipitation and windspeed anomalies for the AP region 140
Figure A1-S4: ERA-5 climate variables on hourly time scale during January 2022.................. 142
Figure A1-S5: Larsen B cumulative melt day maps from 2012/2013 to 2020/2021.................. 142
Figure A1-S6: Melt pond evolution from November 2021 to January 2022. 143
Figure A1-S7: Time series of sea ice concentrations in Weddell Sea on 20 January................. 143
Figure A1-S8: WaveWatch III ocean wave-field data time series. 144
Figure A1-S9: WaveWatch III peak period and significant wave height 145
Figure A1-S10: Jorum Glacier speeds from December 2020 to March 2023. 145
Figure A1-S11: Jorum and Punchbowl elevation changes 146

Appendix II

Figure A2-S1: Iceberg distribution size during two episodes of retreat. 147
Figure A2-S2: Map of IceBridge dataset acquired over Hektoria Glacier in 2017. 148
Figure A2-S3: IceBridge bed and internal reflection powers over Hektoria Glacier. 149
Figure A2-S4: Image and DEM depicting terminus of Hektoria Glacier on 3 October 2022. ... 150
Figure A2-S5: Green Glacier velocity from January 2022 to December 2023 148
Figure A2-S6: Example glacial earthquake location and waveforms on Hektoria Glacier 152
Figure A2-S7: Example of waveform modeling for Dec 25, 2022 Event. 153

CHAPTER 1

1 Introduction

The cryosphere is the part of Earth that is frozen, which includes snow and ice on land, ice caps and ice sheets, glaciers, ice shelves, permafrost, and sea ice. As the climate continues to warm, the deterioration of Earth's icy masses will persist and likely intensify, causing significant changes in Earth's systems. Large bodies of ice on land, such as glaciers and ice sheets, as well as floating ice, such as ocean terminating glaciers, ice shelves, and sea ice, are undergoing extreme changes, ultimately resulting in sea level rise and the loss of some of Earth's most fascinating and aesthetic features. Understanding the fate of the glaciers, ice shelves, and ice sheets and how their changes will impact society requires an in-depth understanding of the processes that control their changes. In this dissertation, I attempt to illuminate key processes in both ice-ocean systems as well as ice-land systems.

2 Ice-Ocean systems

2.1 Antarctica

The Antarctic ice sheet is Earth's largest freshwater reservoir, storing ~58 m of total sea level rise (SLR; Fretwell et al., 2013). By 2100, anywhere from 0.28 to 1.01 m of SLR may occur, depending on what emissions and socioeconomic pathways we take, and how ice sheet processes unfold (IPCC, AR6, 2021). Unknowns in ice sheet processes, especially glacier and ice shelf instabilities, contribute to the uncertainty in SLR projections. Therefore, it is vital to study Antarctic glacier and ice shelf instability processes in order to narrow down the likelihood of different potential instabilities.

An instability involves a feedback in which the process reinforces itself. Tipping points or thresholds also occur, whose crossing can incite a sudden irreversible shift in a system in which no further forcing towards the new state is required. In the ice-ocean system there are several instability processes that are still controversial as to whether they can occur in nature and to what extent they can dramatically affect glacier or ice sheet evolution. In order to better understand these processes we can investigate the cryosphere system in Antarctica.

In Antarctica, the enormous ice sheet flows off of the continent via glaciers and ice streams. Over 75% percent of Antarctica is fringed with ice shelves, a floating portion of the outlet glaciers that can provide a backstress (a longitudinal compressive stress) to the glacier(s) behind it (Fürst et al., 2016). One significant risk is surface meltwater-induced ice shelf break-up, in which melt ponds cause the ice to fracture and then disintegrate, as discussed in greater detail below. Marine ice sheet instability (MISI) is the concept that the grounding line, the point at which the glacier goes afloat, will retreat on a retrograde bedrock slope, causing further retreat and a greater discharge of ice (Schoof, 2007). This has been occurring at Pine Island Glacier (Reed et al., 2024), yet the complex bedrock geology and geometries has made it difficult to predict whether MISI will occur elsewhere, and if so, to what extent (Sergienko, 2022). Marine ice cliff instability (MICI) is the theory that ice cannot support a subaerial ice cliff above ~100 m tall and would collapse, thus exposing a higher ice cliff behind, creating a runaway retreat (Bassis and Walker, 2012; Deconto and Pollard, 2016). This may happen if an ice shelf rapidly disintegrates, exposing high cliffs before the glacier can thin due to internal deformation.

These and other potential instabilities may pose an extreme threat to large glacier systems in Antarctica. For example, the infamous “Doomsday Glacier”, otherwise known as Thwaites, has the ability to raise sea level by 65 cm and holds back up to 10 m from the rest of the interior of West Antarctica (Scambos et al., 2017). Remember, that’s 65 cm globally, meaning any coastal town in the world that is within a meter of present sea level will become ocean, not to mention the impact on storm surges (Calafat et al., 2022). However, before we can say whether or not these processes will occur at Thwaites, or anywhere else for that matter, we must investigate places where abrupt changes in the ice-ocean system have already happened.

2.2 Larsen B Embayment

The Larsen B embayment had an ice shelf that rapidly disintegrated over six weeks in 2002 (Scambos et al., 2004; Rack and Rott, 2004). This was due an extreme summer melt season (van den Broeke, 2005) and may have been exacerbated by an albedo feedback mechanism, in which the lower albedo of wet snow and melt ponds caused more melting. The catalyst of the collapse was likely a long-period wave action reaching the ice front (Massom et al., 2018) that initiated rapid hydrofracture calving, including a chain reaction of supraglacial drainage in which flexural response to the drainage of one lake initiated further hydrofracture drainage of adjacent lakes (Banwell et al., 2013). The sudden loss of the ice shelf exposed the glaciers to catastrophic changes in their dynamics, with greatly increased calving, rapid elevation loss, and retreat (Scambos et al., 2004). The glaciers of the northern Larsen B dumped 6-9 Gt yr^{-1} of ice into the ocean over the next ten years as a result of the increased flux (Berthier et al., 2012; Rott et al., 2018). For perspective, that's 11 olympic sized swimming pools of ice put into the ocean every day from only these few glaciers. In 2011, landfast sea ice occupied the embayment (sea ice that is attached to the shoreline, hereafter 'fast-ice'), persisting for the next 11 years, which stabilized the glaciers and allowed them to readvance. But in 2022, that decade-long period of stabilization ceased when the sea ice broke out, yet again causing substantial changes in the glaciers (Ochwat et al., 2024).

The Larsen B region is a near-perfect location for researching instability processes that plague uncertainties about the future of global sea level rise. In addition, the area represents a natural experiment for understanding the role of fast-ice stabilization of glaciers. In Chapter 2 and 3 of this dissertation, I investigate the processes of abrupt, irreversible, glacier change, exploring what can cause these changes and the consequential aftermath.

Chapter 2 examines the fast-ice break-out at the Larsen B embayment in 2022. It illuminates the drivers of the collapse and the initial glacier response. Scientists have suggested several mechanisms that can cause the break-up of ice shelves, including hydrofracture from melt ponding, thinning causing weakening and subsequent deterioration of strength, and ocean swells flexing the shelf (Massom et al., 2018). In this study, we found that the fast-ice broke up due to a combination of factors: it was weakened by anomalously warm temperatures, there was an open sea ice corridor from the Atlantic ocean down the Weddell Sea coast, and then a large wave swell reached the embayment and broke-up the fast-ice (Ochwat et al., 2024). My study emphasizes ice shelf and sea ice susceptibility to wave-driven break-up and brings to light this increased vulnerability due to diminishing sea ice pack ice conditions. This ultimately raises the risk of ice shelf collapse. To complete the story, we investigated the immediate glacier response in the 14 months following the event. We considered the potential for glacier instabilities, such as the proposed MISI and MICI theories. We found that the glaciers in the embayment increased in speed (> 2-fold), thinned, and Crane and Hektoria glaciers dramatically retreated, 11 and 25 km, respectively.

Never before has a glacier retreated 25 km, 10 km of which was grounded ice, over the course of just two months. This unprecedented rapid retreat of Hektoria Glacier begged for a deeper analysis to investigate the retreat through the lens of known glacier instabilities. In Chapter 3 (Ochwat et al., submitted), we analyzed the characteristics of the retreat and propose a mechanism by which Hektoria Glacier retreated at the observed rate. Due to controversy in Hektoria’s grounding line location, we spent the first part of the chapter establishing evidence for the location of the grounding line using several lines of reasoning and geophysical datasets. We then characterized the retreat in detail using geophysical observations including satellite imagery, elevation data, and seismic events. We used these results to rule out MICI as the mode of rapid runaway retreat. Ultimately, we proposed that a major factor in facilitating the rapid retreat was the presence of an ice plain. Once the fast-ice broke out, rapid thinning ensued, resulting in a large ice plain coming to near-flotation virtually instantaneously. This section calved via rapid slumping and toppling of calved blocks from the ice front over the ensuing two months. Batchelor et al. (2023) was the first to propose rapid buoyancy-driven retreat due to ice plain geometry. However, her study focuses on a paleo-glaciological example from the Scandinavian Ice Sheet. Chapter 3 documents our modern example of this catastrophic retreat process and sheds light on a minimally studied instability process.

3 Land-Ice systems

Antarctica and Greenland get the news coverage for SLR. However, it is the land-terminating mountain glaciers of the world that are imminently dying (Rounce et al., 2023). These land-ice systems, in areas such as the Alps, Andes, Himalayas, and Alaska, have substantial impacts on societies. Furthermore, glaciers in Alaska are contributing more to SLR than any other icy region, including Greenland and Antarctica (Hugonnet et al., 2021). As we discussed tipping points and feedbacks above, Alaska's ice is particularly susceptible to climatic changes due to the presence of large volumes of hypsometrically top-heavy or plateau icefields geometry (McGrath et al., 2017, Davies et al., 2022, Millan et al., 2022; Davies et al., 2024). An ice plateau occurs where there is a large plateau of ice that drains by icefalls connecting to large valley glaciers below. The equilibrium line altitude (ELA; a contour that separates the area of the glacier that is accumulating mass from the area of the glacier that is losing mass), is usually near the elevation of the icefalls, such that as the climate continues to warm, icefalls may disconnect from the valley glaciers below, essentially causing the plateau to become “dead.” As the ELA continues to rise, it encompasses a larger volume of ice, creating a larger area of ablation and more run-off affecting the entire plateau (Pendleton et al., 2017). This process is known to be a tipping point in land-ice systems where there is a melt-acceleration feedback as the ELA increases in altitude (Davies, et al., 2024; Pendleton et al., 2017).

The Juneau Icefield is an ideal place to study these dynamics, and is home to one of the interesting features that result from this kind of glacier geometry. At the base of icefalls that flow off the plateau, there are often topographic waves in the ice, known as ogives. Ogives have been a glaciological spectacle since being described in the mid 1800s (Forbes, 1845), yet it is unclear how they form and what their presence, or lack thereof can tell us about the unique glaciological conditions of a region. In addition to being sentinels of change, they can also act as relics of the icefalls before they disappear.

In Chapter 4, we investigate the formation of ogives, using the Gilkey Glacier in the Juneau Icefield, Alaska as a study site. The Gilkey Glacier is one of several outlet glaciers that funnel ice from the plateau-like icefield into lower elevations, and generates a train of ogives on the glacier at the base of the icefall. We combine remote sensing data and in-situ observations to constrain the annual speed on the ice plateau, icefall, and valley glacier. Using a finite difference model, we test two hypotheses of ogive formation and then integrate the Gilkey Glacier observational data to test whether we can explain the observed train of ogives and what the results tell us about our model. Our results suggest that the plausible main driver of ogive formation is the large seasonal velocity variation of the lower glacier. Our study contributes to answering fundamental questions about glacier dynamics in ice-plateau settings.

4 Tying it all together

Though we often think of land-ice systems and ocean-ice systems as separate, the physics of ice is a key commonality. Chapter 5 synthesizes the conclusions from Chapters 2, 3, and 4. In this chapter, first I will summarize crucial findings from investigating ice-ocean systems and glacier instabilities. Then, I will discuss Chapter 4 and remaining questions regarding ogives and ice-plateau-icefall dynamics. Lastly, I will synthesize the three studies and their implications on our icy world and ice-less future.

CHAPTER 2

Triggers of the 2022 Larsen B multi-year landfast sea ice breakout and initial glacier response

This chapter was originally published in The Cryosphere.

Citation: Ochwat, N. E., Scambos, T. A., Banwell, A. F., Anderson, R. S., Maclennan, M. L., Picard, G., Shates, J. A., Marinsek, S., Margonari, L., Truffer, M., and Pettit, E. C.: Triggers of the 2022 Larsen B multi-year landfast sea ice breakout and initial glacier response, The Cryosphere, 18, 1709–1731, https://doi.org/10.5194/tc-18-1709-2024, 2024

Abstract

In late March 2011, landfast sea ice (hereafter, 'fast ice') formed in the northern Larsen B embayment and persisted continuously as multi-year fast ice until January 2022. In the 11 years of fast ice presence, the northern Larsen B glaciers slowed significantly, thickened in their lower reaches, and developed extensive mélange areas leading to the formation of ice tongues that extended up to 16 km from the 2011 ice fronts. In situ measurements of ice speed on adjacent ice shelf areas spanning 2011 to 2017 show that the fast ice provided significant resistive stress to ice flow. Fast ice breakout began in late January 2022, and was closely followed by retreat and break-up of both the fast ice mélange and the glacier ice tongues. We investigate the probable triggers for the loss of fast ice and document the initial upstream glacier responses. The fast ice break-up is linked to the arrival of a strong ocean swell event (>1.5 m amplitude; wave period waves >5 s) originating from the northeast. Wave propagation to the ice front was facilitated by a 12-year low in sea ice concentration in the northwestern Weddell Sea, creating a near-ice-free corridor to the open ocean. Remote sensing data in the months following the fast ice break-out reveals an initial ice flow speed increase (> 2-fold), elevation loss (9 to 11 m), and rapid calving

of floating and grounded ice for the three main embayment glaciers Crane (11 km), Hektoria (25 km), and Green (18 km).

1 Introduction

As the climate warms, ice shelves in Antarctica are predicted to become more susceptible to collapse (Mercer, 1978; Gilbert and Kittel, 2021). In the late 1980s and mid 1990s several ice shelves along the Antarctic Peninsula (AP) coast retreated and eventually disintegrated, including the Wordie, Prince Gustav, Larsen Inlet, Larsen A ice shelves, and in March 2002, the northern two-thirds of the Larsen B Ice Shelf (Rott et al., 1996; Glasser and Scambos, 2008; Cook and Vaughan, 2010). In 2008 and 2009, several smaller break-up events occurred on the Wilkins Ice Shelf (Braun et al., 2009; Scambos et al., 2009). There has been significant research elucidating the causes of these collapses, focusing on both ice-shelf thinning due to basal and surface melting (Smith et al., 2020), as well as lake drainage mechanisms related to surface meltwater-induced ice-shelf flexure and hydrofracture (Doake and Vaughan 1991; Scambos et al., 2000; Scambos et al., 2003; Banwell et al., 2013; Banwell and MacAyeal, 2015) partly attributed to warmer climate conditions (Rott et al., 1998), plate-bending stresses on the ice-shelf front (Scambos et al., 2009), and ocean swell flexure (Massom et al., 2018). Massom et al. (2018) further implicate loss of fast ice and ocean swell in the Wilkins Ice Shelf breakup events, following loss of a protective pack ice buffer offshore – due to the vulnerability of fast ice to ocean swells (Crocker and Wadhams, 1989; Langhorne et al., 2001). While fast ice is consolidated sea ice that remains stationary attached to the coast and can be annual or perennial (Fraser et al., 2021), pack ice refers to sea ice that is comprised of separate floes and is under the influence of winds and ocean currents. The loose structure of pack ice has a strong damping effect on ocean swell (Squire, 2007).

Intense surface melt events on the eastern Antarctic Peninsula have been linked to atmospheric rivers (ARs; Wille et al., 2019; Wille et al., 2022) and foehn winds (Cape et al., 2015; Datta et al., 2019; Laffin et al., 2022). ARs are long narrow bands of warm and moist air that can cause extreme warm temperatures, increase surface melting, advect sea ice away from the ice edge, reduce sea ice concentrations, and generate foehn events (Bozkurt et al., 2018; Wille et al., 2022; Liang et al., 2023). Foehn events occur when a moist air mass ascends on the windward side of a mountain range or ridge and cools at the (lower) wet-adiabatic rate, while losing moisture to precipitation. It then descends over the lee side, adiabatically warming at the higher dry-air rate, resulting in an increase in temperature. The loss of ice shelves can substantially reduce the stability of tributary outlet glaciers, leading to acceleration, increased calving, thinning, and ultimately, sea level rise. For example, when the Larsen B collapsed in 2002, Crane Glacier thinned by 25 m yr^{-1} over much of its length (Needell and Holschuh, 2023) and immediately sped up by roughly 3-fold (Rignot et al., 2004) and the Hektoria-Green-Evans (hereafter, HGE) Glacier system ice flow speed increased by up to 8-fold (Rignot et al., 2004). After the collapse of the Larsen B in 2002, the embayment was frequently filled by seasonal sea ice (landfast and pack ice). However, in late March 2011, landfast sea ice (hereafter 'fast ice') formed in the Larsen B embayment, and the interior two-thirds of the embayment was continuously covered by multi-year fast ice until January 2022. On 19 January 2022, this fast ice cover was suddenly fractured and began to drift out, leading within days to retreat and break-up of the tributary glacier mélange and floating ice tongue areas (Fig. 2.1). Fast ice has been shown to stabilize outlet glaciers by reducing calving (Amundson et al, 2010; Robel 2017) and suppressing wave action against the outlet glacier (Murty, 1985; Langhorne et al., 2001) causing the glacier terminus to advance (Reeh et al., 2001). When fast ice or mélange breaks up, ice-shelf calving resumes, sometimes releasing several decades of accumulated ice flux, and exposing the new terminus to ocean dynamics (Reeh et al., 2001; Cassotto et al., 2015).

Several studies have suggested that break-up of fast ice can reduce the structural integrity of ice shelves and ultimately lead to their collapse (Khazendar et al., 2007; Massom et al., 2010; Borstad et al., 2013; Banwell et al., 2017; Massom et al., 2018). There have been many examples of tributary glacier acceleration and significant ice front retreats following the removal of fast ice or pack ice in Greenland and Antarctica (Miles et al., 2017, Miles et al., 2018, Gomez-Fell et al., 2022). Others (Sun et al., 2023; Surawy-Stepney et al., 2023) suggest that fast ice does not provide sufficient buttressing (resistive stress to impact the system dynamics.

Here we investigate the climatic and oceanic drivers that led to the rapid break-out of the decade-old Larsen B fast ice in January 2022, while also drawing parallels to previous fast ice and ice shelf collapses. We then assess the initial glacier dynamic response to the loss of the buttressing fast ice by evaluating changes in velocity, terminus position, and elevation of the Crane, Jorum, Punchbowl, and HGE glaciers. A preliminary assessment of the cause of the fast ice break-up was discussed as a sidebar in the NOAA State of the Climate 2022 report (Ochwat et al., 2023b). However, the current study evaluates the events in much greater detail and includes a quantitative look at the glacier response.

2 Study area

The Larsen B embayment (65.24° S, and 61.00° W; Fig. 2.1) is located on the eastern side of the AP, between Graham Land and the northwestern Weddell Sea and is ~7000 km^2 in area. North of the embayment is the Seal Nunataks Ice Shelf (Shuman et al., 2016) and to the south is a remnant of the Larsen B Ice Shelf; the Scar Inlet Ice Shelf. Prior to 1995, the eastern coast of Graham Land was almost entirely flanked by ice shelves (e.g., Skvarca et al., 1999;

Cook and Vaughan, 2010), but after a series of disintegrations, only the Scar Inlet and Larsen C Ice Shelf remain.

Due to the elevated narrow ridge of the northern AP (Graham Land) and the prevailing westerly wind, the climate of the Larsen B embayment region differs greatly between the western and eastern flanks. The ridge obstructs the Southern Hemisphere westerlies and induces strong orographic lifting and precipitation on the western side, while the eastern side is much drier and cooler (King et al., 2003; Van Wessem et al., 2015). The climate is heavily influenced by the phase of the Southern Annual Mode (SAM; Leeson et al., 2017; Fogt and Marshall, 2020). When the SAM index is positive, warming events occur more frequently on the eastern side of the Peninsula due to an increase in westerly flow across the Peninsula (Orr et al., 2008; Van Lipzig et al., 2008).

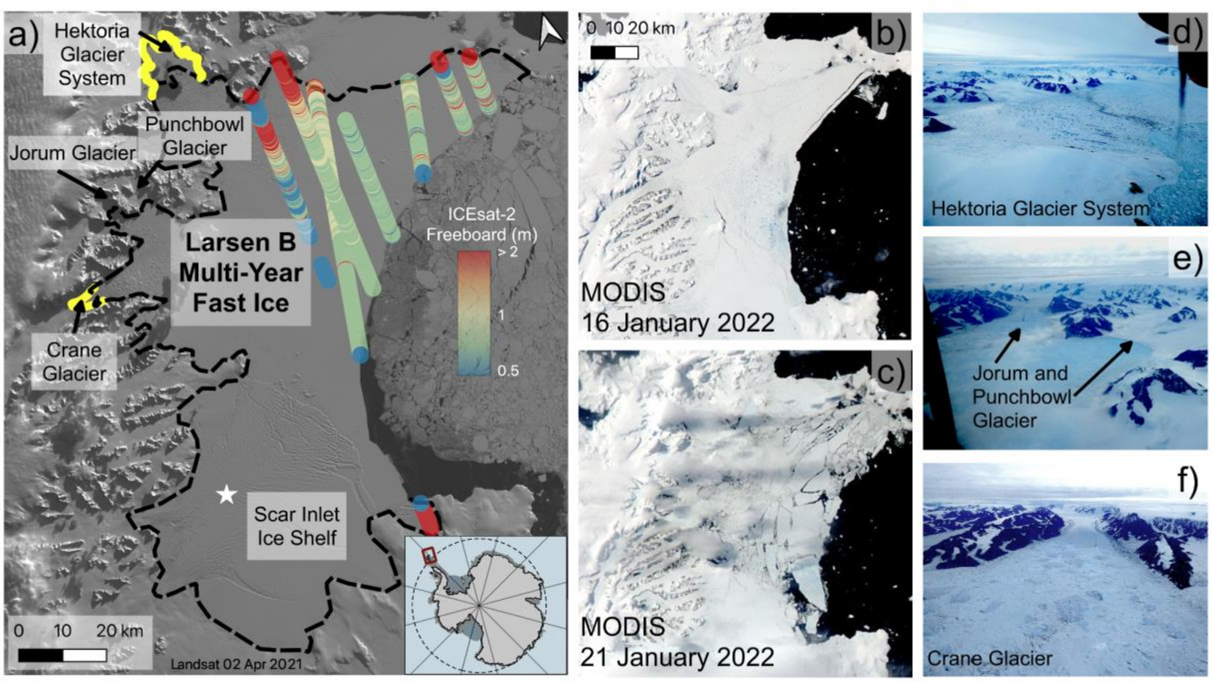

Figure 2.1: a) Freeboard thickness from ICESat-2 data from 1 January 2021 to 1 January 2022. The yellow dashes show the TanDEM-X determined 2016 grounding zone (Rott et al., 2018) and black dashes are a slope change and calving-morphology inferred 2021 grounding zone (this study). An AMIGOS GPS installation on Scar Inlet Ice Shelf is indicated by the white star. The

background image is from Landsat 8 2 April 2021. b) MODIS image from 16 January 2022. c) MODIS image from 21 January 2022, two days after initial rifts in the fast ice formed. d, e, f) Images captured by a British Antarctic Survey overflight on 31 January, 11 days after the fast ice break-out event.

3 Data and Methods

The following datasets are used in various capacities to evaluate the triggers of the fast ice break-out as well as the initial glacier response. Reanalysis data is used to evaluate both potential atmospheric and oceanic triggers. Passive microwave data is used to determine sea ice extent and surface melt conditions. Optical satellite imagery from a number of satellite systems, and synthetic aperture radar data, are used for assessing glacier ice, fast ice, elevation changes, and determining glacier speeds. Laser altimetry data is also used for assessing initial glacier and fast ice elevation. Lastly, GNSS data is used to look at Scar Inlet Ice Shelf speeds.

3.1 Reanalysis Data

We used ERA-5 Reanalysis data (Hersbach et al., 2020) at both monthly and hourly temporal resolution to assess temperature and precipitation anomalies in 2017 to 2022, as well as foehn wind occurrence in the months prior to and including January 2022. To investigate the presence of foehn winds, we followed Laffin et al. (2022), who determined that foehn winds that produce surface melt require a temperature > 0°C, a wind speed of > 2.85 m s^{-1}, humidity < 79%, and a wind direction from the north or northwest. These thresholds agree with Cape et al. (2015)'s determination of the onset of "foehn days" (foehn conditions for greater than 6 hours).

To identify ARs during the last two weeks of January 2022, we use hourly ERA-5 to examine vertically integrated water vapor transport (IVT) bands that extend from the extra-tropics towards the Antarctic ice sheet (Bozkurt et al., 2018; Wille et al., 2019). IVT is calculated as the vector magnitude of eastward integrated water vapor transport (uIVT) and northward integrated water vapor transport (vIVT). We identify an AR event during the breakout as a continuous, extended region of locally high IVT that reaches a peak intensity of almost 300 kg m^{-1} s^{-1}, consistent with Wille et al. (2022).

Following Massom et al. (2018) and Teder et al. (2022), we investigate the occurrence of open-ocean corridors across the sea ice zone, using ERA-5 and WaveWatch III wave data. We used significant wave height as a proxy for wave energy (Teder et al., 2022), calculated to be four times the square root of the zeroth moment of the energy density spectrum (Massom et al., 2018). We used peak wave period as an indication of longer swell wavelengths, which can transmit more energy into the fast ice plate (Robinson and Haskell, 1992; Massom et al., 2018). Mean wave direction is used to assess alignment with the corridor axis and propagation toward the ice front. We examined the hourly time series of ocean wave variables for January 2022 at two different locations, within the corridor and near the Larsen B fast ice front.

3.2 Satellite Data

3.2.1 Passive Microwave Data

We combined passive microwave data from two successive sensors, namely the Advanced Microwave Scanning Radiometer for the Earth Observing System (AMSR-E) on the Aqua Satellite, and the Advanced Microwave Scanning Radiometer 2 (AMSR-2) on the 'Shizuku' (GCOM-W1) satellite. Together, these passive microwave sensors provide nearly continuous daily data from 2002 until present (apart from a gap from October 2011 to June 2012 between the two satellites' operation). The daily overall sea ice concentration data product (Spreen et al., 2008) was used to assess overall sea ice extent and concentration on the same day (January 19th) for the 12-year period.

We also used AMSR-E/2 data to investigate fast ice melt extent for each melt season (October 1 to March 31) from 2011 to 2022. To do this, we followed the algorithm from Torinesi et al. (2003) and methods of Picard et al. (2007). For each 12.5 km grid cell and each day, the liquid water is detected as present if the 19 GHz horizontally-polarized brightness temperature is higher than a threshold that is empirically determined in each cell and for each year by using the brightness temperatures during the winter (dry snow) season. ‘Melt days’ are defined as days when meltwater is present on or near the ice surface, but active melting is not necessarily taking place. Finally, we calculated the total number of melt days for each melt season. We used the same fully automatic algorithm as used recently in Banwell et al. (2021, 2023) for Antarctic ice shelves. However, for the current study, a careful visual evaluation of the passive microwave data (brightness temperature timeseries) was done for all the pixels in proximity to the open ocean. This was necessary because the real footprint of the measurements acquired by the radiometer is larger than the pixel size and of elliptical shape (14 x 22 km) (Meier et al., 2018). The ellipse’s position and orientation changes from track to track with respect to the pixels. As a consequence, the fast ice pixel near the shore may be contaminated by signal coming from the nearby open ocean, hence potentially perturbing the detection of the melt. Our manual selection prevents this effect.

3.2.2 Optical Imagery and Synthetic Aperture Radar

We used MODIS (Moderate-Resolution Spectroradiometer), Landsat 8 and 9, Worldview (WV) -1, 2, and 3, and Synthetic Aperture Radar (SAR; Sentinel 1) to investigate changes in glacier characteristics and dynamics. The MODIS sensor, on the Aqua and Terra satellites, has a data archive from 2002 to present and was used to determine the dates of fast ice formation, seasonal area changes, break-up timing and extent of retreat. The Landsat 8 and 9 Operational Land Imager product was used to assess melt patterns during the 2021/2022 austral season and to determine ice flow speeds using a Python-based image cross-correlation software, PyCorr (Fahnestock et al., 2016). PyCorr measures ice displacement between two images by finding the peaks in normalized cross-correlation surfaces between image chips extracted in a grid pattern over both images. For images separated by one year, using Landsat 8 and 9 panchromatic images (15 m spatial resolution) error is ~±7.5 m yr^{-1}, however shorter time intervals result in higher errors (Fahnestock et al., 2016). WV-1, 2, and 3 satellite images have very high resolution (< 0.5 m) and were used for investigating the morphology of icebergs and the creation of digital elevation models (DEMs). Worldview in-track stereo-image DEMs (Table A1-S1) were obtained from the Polar Geospatial Center (PGC). The DEMs have a spatial resolution of 2 m and absolute accuracy of ~4 m in horizontal and vertical dimensions (from PGC documentation). We corrected for the geoid using EGM 2008 and then assessed the mean elevation difference (i.e., bias) for six bedrock regions in each of the WV DEMs relative to the REMA DEM (Howat et al., 2022) and applied the mean offset to the WV DEMs, similar to the method used with the ArcticDEM for the Hunt Fjord Ice Shelf in Greenland (Ochwat et al., 2023a).

We assessed calving styles and approximate grounding zone positions using the imagery and DEM data. In Figure *2.*1a, the yellow dashes show Rott et al.'s (2018) 2016 grounding line, determined by surface elevation changes from TanDEM-X differencing. The black dashes show a slope change and calving-morphology inferred 2021 grounding line (this study). Our grounding zone is estimated from a break in slope in the DEMs and morphological changes, such as the appearance of broad surface undulations suggestive of bottom crevassing and changes in calving style at the glacier front. We do not suggest the grounding line advanced between the two estimates, but arise from the two different determination methods. Our grounding zone position is similar to the partial grounding zone proposed by Sun et al. (2023) and Tuckett et al. (2020); where a presence of an ice plain can explain why there are multiple determinations of a grounding zone (Friedl et al., 2019). Calving styles of grounded ice often show surface slumping or tilting prior to separation, indicative of listric faulting (Parizek et al., 2019), super-buoyancy

(Murray et al., 2015) or ice-cliff stresses (Bassis et al., 2021; Crawford et al., 2021). Further analysis of the evolution of the grounding zone position and the evolution of calving styles for the lower HGE Glaciers will be assessed in a later study.

We used Sentinel-1A and -1B SAR data to estimate ice flow speeds. The Alaska Satellite Facility HyP3 Pipeline uses speckle tracking to create velocity rasters using SAR image pairs. The HyP3 pipeline utilizes GAMMA and auto-RIFT algorithms through the Vertex On-Demand Processing Tool (Gardner et al., 2018; Lei et al., 2021). The autoRIFT code includes an iterative process for determining the flow velocity, with varying relative errors that have an average of 4% for both X and Y direction velocity (Lei et al., 2021). Sentinel-1A and -B have a repeat time of 6 days when used in combination, and 12 days if only 1A or 1B pairs are used. Sentinel-1B malfunctioned in December 2021, leaving only Sentinel-1A data available after that date.

We extracted ice speed profiles in a band centered on the Airborne Thematic Mapper (ATM) profiles from Operation IceBridge for Crane, Jorum, Green, and Hektoria glaciers, generating five profiles that span the central 1 km near the approximate glacier centerlines. To approximate the mean monthly speed, we averaged the speed profile of two 12-day Sentinel-1 cycles.

3.2.3 Laser Altimetry

To study changes in surface ice elevation, we combined the WV image-derived DEMs with ICESat-2 altimetry data. We used the ICESat-2 ATL06 version 5 product, which provides a linear surface approximation of 40 m overlapping segments along each ground track (Smith et al., 2021) with a 91-day repeat cycle (clouds permitting). We correct for the geoid prior to estimating the initial thickness of the fast ice, glacier tongues, and elevation of the glaciers. We used ICESat-2 data for the period January 2021 to December 2021 (Fig. 2.1) to determine the initial fast ice and glacier tongue freeboard. To account for tidal variations, we only used tracks that crossed open water (as assessed in MODIS or Sentinel 1 imagery). For Figure 2.1, we applied offsets to each track according to the reported elevation of the open sea surface at the time of acquisition. Assuming the proportion of snow relative to ice thickness is low, we calculated fast ice thicknesses from the freeboard using the standard hydrostatic equilibrium floating ice relationship using a density of 1028 kg m^{-3} for sea water and 900 kg m^{-3} for ice. For analyzing glacier elevation changes, we extracted ICESat-2 data from where tracks cross < 200 m of near-centerline tracks flown by Operation IceBridge using the ATM sensor, and averaged the data. Standard error analysis was performed on the individual WV and ICESat-2 elevations. We use the square-root of the sum of the squares of the error, where the errors are the standard error of the mean and the instrument error of WV or ICESat-2.

3.2.4 GNSS data from AMIGOS station on Scar Inlet

An Automated Meteorology-Ice-Geophysics Observing System (AMIGOS) unit with a dual-channel GPS receiver was placed on the Scar Inlet Ice Shelf in February of 2010 (Scambos et al., 2013) as part of the Larsen Ice Shelf System, Antarctica project (LARISSA; Wellner et al., 2019). The system provided hourly position data spanning February 2010 through August 2017, with several data gaps due to power and system malfunctions, that were periodically repaired during re-visits. Precision of the hourly position data was approximately ±20 cm due to wind on the tower mounting of the GPS antenna. We used daily, weekly, and monthly averaged data to evaluate ice flow of the Scar Inlet Ice Shelf over the formation and thickening period of the adjacent fast ice.

3.2.5 Aerial photography

To evaluate how the fast ice break-up occurred and the potential calving styles of the outlet glaciers, we also analysed airborne photography. On 31 January 2022, the British Antarctic Survey flew a Twin Otter over the study area with a digital camera (Panasonic DMC-

TZ80e) and a series of photos of the glacier fronts and ice tongue areas were taken along with approximate geolocation.

4 Results

4.1 Multi-year fast ice in the Larsen B embayment

4.1.1 Formation and evolution of Larsen B multi-year fast ice

The fast ice that formed in March 2011 had a few partial retreats during the 11 years that the interior embayment region was continuously covered. Portions of the fast ice broke out and reformed in May 2011 and March 2012. From March 2012 onwards, the fast ice maintained a minimum area of ~3975 km^2 (based on MODIS imagery). From 2012 to 2016 the fast ice cover was relatively stable with a maximum area of ~6280 km^2 in 2016. After 2016, the eastern portion of the fast ice, ~1200 km^2 in area, seasonally re-formed and broke out. The lowest extent in the MODIS record was in February 2019, when a slightly larger area (2000 km^2) broke out. In late 2021 the outer portion broke out again, returning to the 2019 areal extent, and by early 2022 the extent was similar to the 2019 minimum (Supplemental Video. 1). Lateral rifts appeared in ~2016 near the confluence of Scar Inlet Ice Shelf and Crane Glacier extending north and south from Cape Disappointment. Early assessments of the fast ice thickness in the Larsen B embayment near the oceanward ice front were 2.5 to 4 m (Scambos et al., 2017). In the inner embayment, altimetry data indicate a thickness of tens to hundreds of meters in areas of mélange containing fast ice and glacier tongue ice (Fig. 2.1; Fig. A1-S1 and A1-S2).

4.1.2 Upstream glacier response to fast ice formation

During the 2011-2022 period of fast ice presence in the embayment, changes in the glacier extents and GNSS data suggests that the fast ice stabilized the Larsen B tributary glaciers and buttressed the Scar Inlet Ice Shelf, relative to the state prior to the fast ice occupation. This corroborates the findings of Christie et al. (2022). MODIS and Landsat images show that the glacier tongues readvanced into the embayment, and the fjords became a floating composite of glacier ice, large icebergs, and fast ice (hereafter, ‘mèlange’). The ice reached thicknesses of up to 320 m near the glacier tongue termini (inferred from freeboard estimates in Fig. 2.1). Crane Glacier’s terminus and associated mélange advanced at ~1 km yr^{-1} (11 km total) and the main trunk of the glacier thickened (Rott et al., 2018; Needell and Holschuh, 2023). The HGE floating tongue and mélange reformed into an ice-shelf-like feature with a central freeboard exceeding 40 m. HGE advanced approximately 20 km from February 2011 to January 2022, with the new floating mixed-ice-type area covering ~250 km^2. Jorum Glacier advanced ~4.5 km over the same period, while Punchbowl Glacier only readvanced ~0.5 km and did not create an extensive mélange or glacier tongue.

GPS data from Scar Inlet Ice Shelf (Fig. 2.2) show an acceleration of ice shelf flow speed from installation of the GPS in early 2010 to late 2012, followed by a cyclical variation in flow speed that varied by season. This indicates that the ice shelf was accelerating prior to the formation and thickening of the multi-year fast ice. From late 2012 onwards, the acceleration of the ice shelf was halted, and an annual cycle with faster flow during late summer-early autumn and a springtime minimum flow speed was observed. We infer that significant buttressing of the ice shelf by the fast ice mitigated the acceleration of the shelf. Moreover, the seasonal cycle of flow speed, with highest flow speed during mid-summer, is interpreted as an effect of seasonal weakening of the fast ice plate due to summer warmth (Pettit et al., in prep).

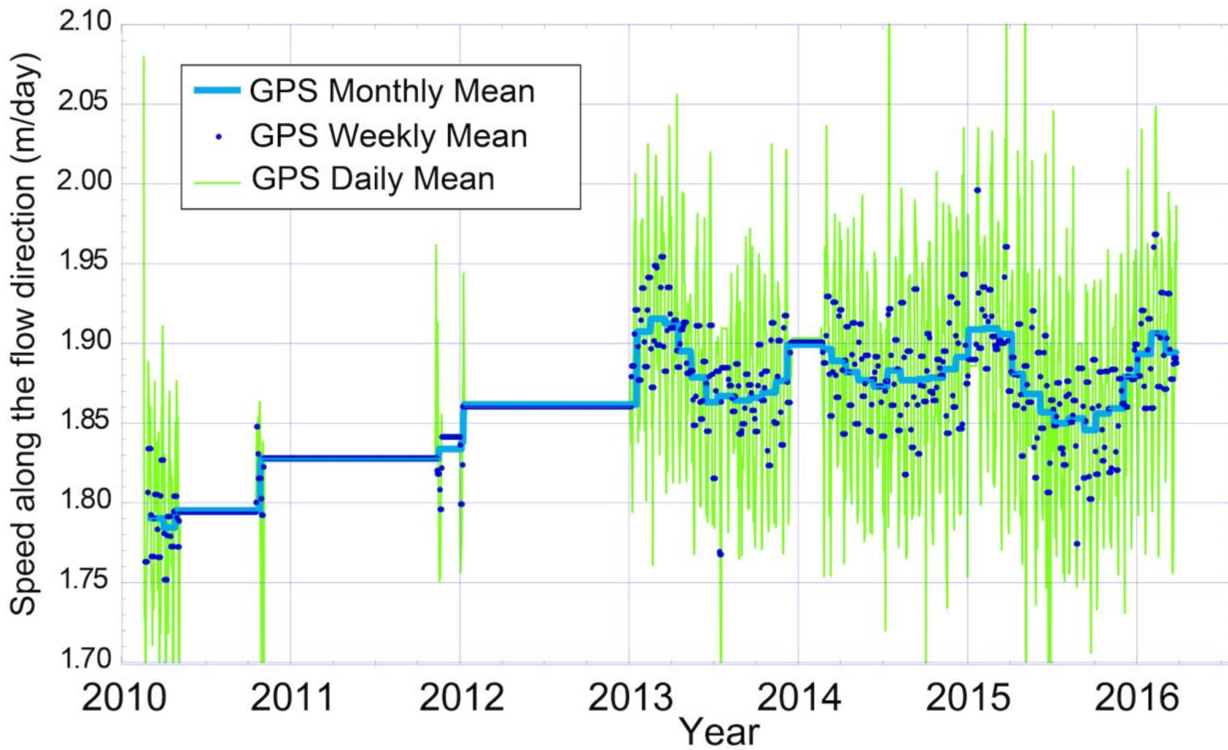

Figure 2.2: Scar Inlet Ice Shelf ice flow speeds from AMIGOS GPS from 2010 to 2017. Blue line is the monthly mean, blue dots are the weekly means, and green vertical lines are the daily means.

4.1.3 Multi-year fast ice break-up

MODIS imagery shows that new narrow fractures started to form in the fast ice between 18 and 19 January 2022, widening thereafter, and by 20 January the fast ice area was densely fractured and no longer coherent. By 21 January, floes derived from the fast ice plate had drifted 9 to 16 km northeast into the Weddell Sea, exposing the tributary glacier fronts to open water (Fig. 2.1c). The fast ice floes continued to drift away, fully clearing the embayment by 8 February.

Pack ice began to reappear in the embayment in March 2022, but overall sea ice cover was not persistent through the next 12 months. Over the course of the late austral summer into the autumn and winter, MODIS images indicate overall sea ice cover in the embayment varied in extent and apparent coherency. Open water conditions in the embayment and the area adjacent to the AP and James Ross Island persisted through March 2022. Landfast ice did not form in the embayment during the southern hemisphere autumn and winter 2022. In October 2022 the sea ice in the embayment varied in spatial extent, and began to decrease significantly in November 2022, and by December 2022 there were minimal floating bergs or pack ice floes. From January to March 2023 the embayment was devoid of floating ice and remained open ocean. However, by the end of March 2023, pack ice and fast ice started to reform in the embayment.

4.2 Potential Attributions of the 2021-2022 Fast Ice Breakout

4.2.1 Seasonal meteorological conditions

For November 2021 to January 2022, there is no substantial precipitation anomaly in our study area (Fig. A1-S3A). The wind speed anomaly composites indicate a slightly higher than average wind speed during the 2021/2022 melt season, with December having the largest anomaly, primarily in the Bellingshausen Sea (Fig. A1-S3B). The temperature anomaly over this period indicates the Bellingshausen Sea was slightly warmer (~2°C) than the 1979 to 2022 climatological average, whereas the Larsen B embayment was up to 4°C warmer (Fig. 2.3).

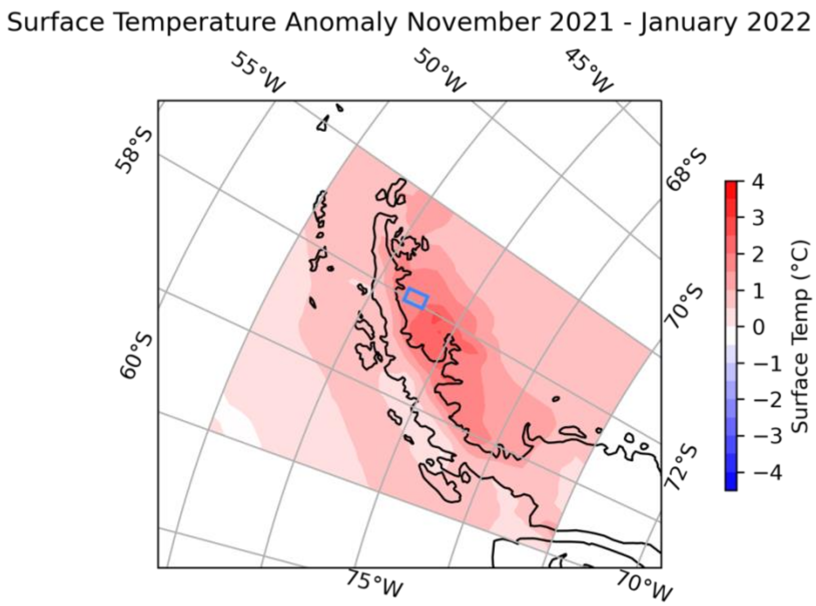

Figure 2.3: ERA-5 surface air temperature anomalies around the Antarctic Peninsula. The blue box is the area of grid cells used for the foehn wind analysis (Fig. A1-S4).

We also looked at the January 2022 mean hourly values of several meteorological variables that indicate foehn wind events: temperature, windspeed, wind direction, relative humidity and net ablation for the Larsen B region (blue box, Fig. 2.3), (Fig. A1-S4). Five identified foehn events occurred from 17 to 21 January 2022, two prior to the fast ice break-out, one during that event, and two after it. These events likely enhanced surface melting on the fast ice, potentially augmenting the break-up of the ice in the post-break-up days (19 and 21 January) and dispersing the fast ice floes northeastward in the following weeks.

Since ARs can be linked to foehn events and therefore to increased surface melting (Bozkurt et al., 2018), we also investigated AR occurrence in the period of the fast ice break-out event. A time series of IVT in the Larsen B region indicates that IVT associated with an AR event from the northwest begins to increase on 19 January and peaks on 20 January 11:00 UTC (Fig. 2.4a and b; Wille et al., 2022). IVT remained high until 22 January, when the AR weakened and dissipated. This event occurred simultaneously as the series of foehn events from 19 to 22

January, suggesting the AR led to the foehn winds that occurred just after the initiation of the break-out.

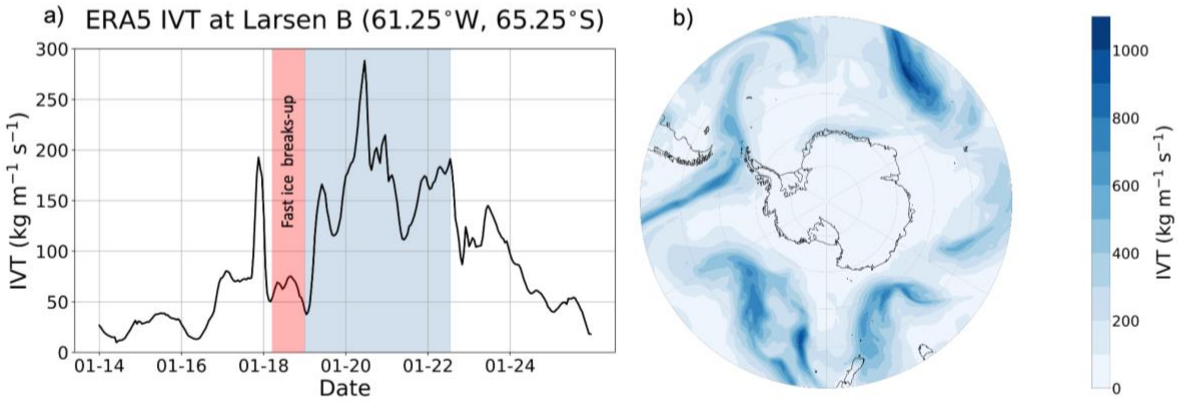

Figure 2.4: a) time series of IVT for January 2022 at 65.25°S, 61.25°W. b) map of ERA-5 IVT in the southern hemisphere at 11:00 UTC on 20 January 2022, during the peak IVT at Larsen B. The AR is identified as a long filament of high IVT that extends from the eastern Pacific across the Antarctic Peninsula and into the Atlantic Ocean. Red shading indicates the arrival of the swell and fast ice break-up. Blue shading indicates the duration of the AR event over Larsen B.

4.2.2 Surface melt

Figure *2*.5 shows cumulative melt days for each melt season from 2012/2013 to 2020/2021 over the Larsen B multi-year fast ice and Scar Inlet Ice Shelf, derived from AMSR-E/2 passive microwave data. Figure *2*.5a shows a map of the grid cells used in the analysis, as well as cumulative melt days for the 2019/2020 season, 2020/2021 season (i.e. the two melt seasons preceding the break-up event), and the mean cumulative melt days for each season from 2012/2013 to 2020/2021. We do not include the 2021/2022 melt day data in Figure *2*.5a because of the mid-season break out of the fast ice in that summer. Maps of cumulative melt days for all melt seasons are available in Figure A1-S5. Figure 2.5b shows the spatially-averaged melt days over the study area, as well as the cumulative days when the melt area was 100% of the study area, for nine melt seasons leading up to the break-up event, as well as the melt season with the fast ice break-out (2021/2022).

The 2021/2022 season did not have a particularly long or spatially more extensive melt season relative to the previous nine melt seasons. Of the years studied, 2019/2020 had both the longest melt season and the one with the highest number of days with 100% melt area; nonetheless the fast ice survived this season, as well as the preceding high-melt years.

In addition to our analysis of passive microwave data (above), which may indicate the presence of surface meltwater ponding (e.g. Picard et al., 2022), we also analyzed optical satellite images for evidence of surface meltwater ponding. Landsat 8 images in November and December 2021 show the surface of the fast ice was extensively covered with melt ponds (Fig. A1-S6). However, by January 2022, the surface melt ponds on the fast ice appeared to have refrozen, and melt pond extent was reduced (Fig. A1-S6).

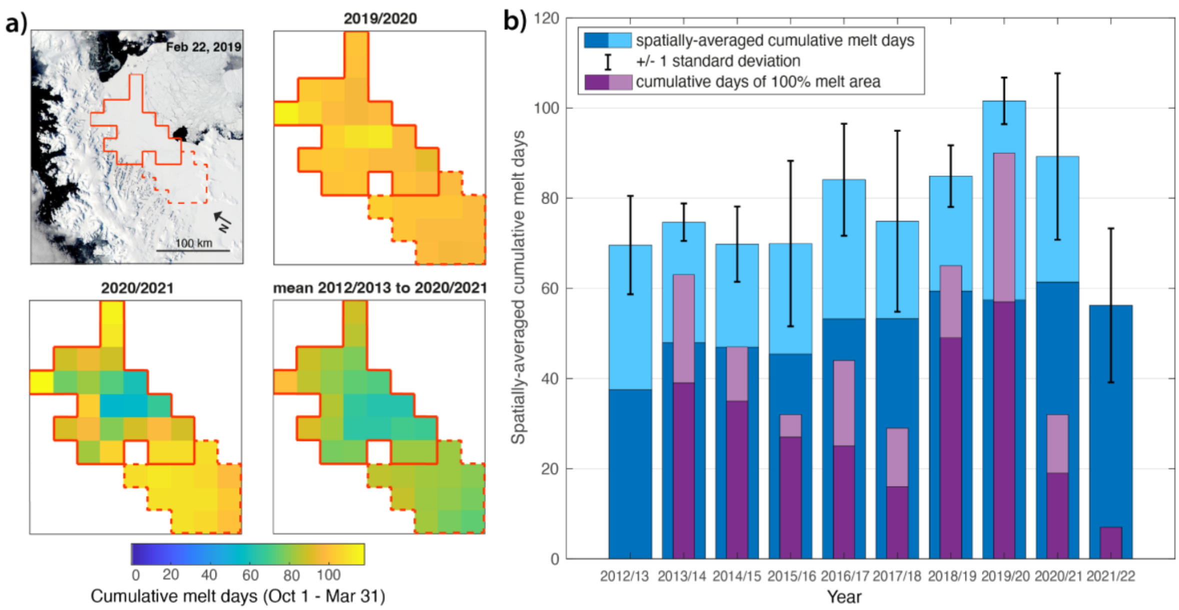

Figure 2.5: Cumulative melt days derived from AMSR-E/2 passive microwave melt data. a) Cumulative melt days over the fast ice area in the Larsen B embayment (area within solid red lines) and over the Scar Inlet Ice Shelf (area within dashed red line) for the 2019/2020 and 2020/2021 melt seasons, and the mean from 2012/2013 to 2020/2021. b) Spatially-averaged

melt days (blue shades) and cumulative days of 100% melt area (purple shades) over just the Larsen B embayment fast ice (solid red lines in panel a) from 2012/2013 to 2021/2022. The dark purple and dark blue bars show cumulative melt days from just 1 October through 18 January (i.e. the data available for the 2021/2022 season), and the light purple and light blue bars show cumulative melt days from 1 October through 31 March.

4.2.3 Regional Sea ice Cover

Figure *2.*6a displays a mapping of sea ice concentration from AMSR-E/2 data in the Weddell Sea on 19 January 2022. Figure 2.6b shows a time series of overall sea ice area (concentration that is greater than 15% multiplied by area of pixel) for the date of 19 January for each year from 2010 to 2022 in a selected region (gray box in Fig. *2.*6a; 2011/2012 did not have AMSR-E/2 sensor data on this date; MODIS imagery shows extensive sea ice cover in the Larsen B fast ice front area through this time). The selected region represents a potential ocean swell corridor leading to the Larsen B embayment from 2010 to 2022 (see Section 5.2; also Teder et al., 2022). For the 8-year period (2013 to 2020 inclusive) the overall sea ice area in this region of the northwest Weddell Sea was over 125,000 km^2 (>50% of the box area). In 2011, sea ice area was just 100,000 km^2 on 19 January; however, we note that the fast ice formed later in this year (March). The overall sea ice area dropped in 2021 to 75,000 km^2, and in 2022 its area was just below 40,000 km^2. As Figure 2.6a shows, a corridor is present along the eastern side of the Peninsula in January 2022, which opened on ~8 January 2022 according to the MODIS and

AMSR-E/2 record. This pathway, which allows for wave action to access the front of the Larsen B fast ice, had not been present since the fast ice's formation in 2011 (Figs. 2.6b and A1-S7).

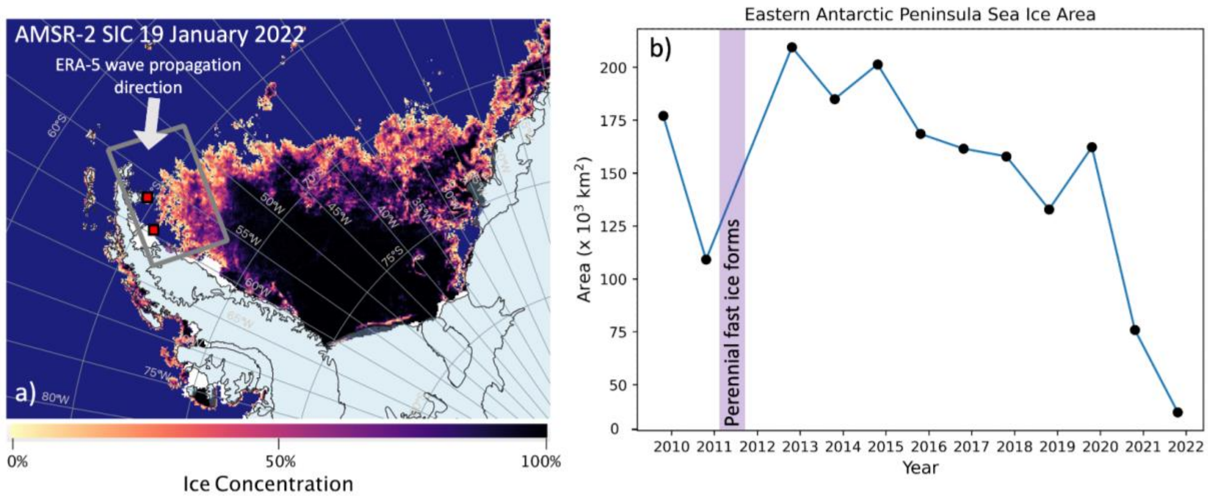

Figure 2.6: a) Pack sea ice concentration and distribution map on 19 January 2022 from AMSR-2 data (Spreen et al., 2008). Small red squares show the location of the ERA-5 wave height grid cells (Fig. 2.7). The gray box is the region selected for the overall sea ice area in 6b. The white arrow denotes the wave propagation direction on 19 January ERA-5 data. b) Overall sea ice area (concentration in each grid cell multiplied by the grid cell area) from AMSR-E and AMSR-2 data in the corridor region of the NW Weddell Sea for 2010 to 2022. Error in sea ice concentration according to Spreen et al. (2008) is ~7%. Purple vertical shading indicates the time period of fast ice formation.

4.2.4 Wave action

Examining both ERA-5 and WaveWatch-III wave data, the first large swell able to pass through the open-ocean (sea ice-free) corridor and reach the Larsen B fast ice edge occurred on 18 and 19 January (Figs. 2.7 and A1-S8). In the early hours (UTC) of 18 January 2022, the significant wave height averaged ~0.1 m in the selected grid cell region. By the afternoon on 18 January the average wave height rose steeply to a maximum of 1.75 m near Larsen B and to over 2 m near James Ross Island ~150 km to the northeast (red boxes, Fig. 2.6). Simultaneously, the peak wave period increased to ~5 s, indicating a wavelength equivalent to ~40 m. The wave propagation direction was bearing ~250° ± 25° through this period, similar to the orientation of the open corridor in the pack ice. There were no events in November or December 2021 that included both a long peak period and a high significant wave height (and in any case, pack ice damped wave propagation in the region until ~8 January). Both months have peak periods consistently less than 6 s and wave heights below 1.4 m (Fig. A1-S8 and A1-S9). Furthermore, there were no other times during January 2022 when the wave swell had both a long peak period and high significant wave height (Fig. 2.7). Abrupt shifts in peak period and significant wave height (see Methods) are evident when the wave corridor opens near James Ross Island (gray band 8 Jan 2022) and when the event occurs (gray band 18 Jan 2022), as well as when the wind direction changes (Fig. A1-S4).

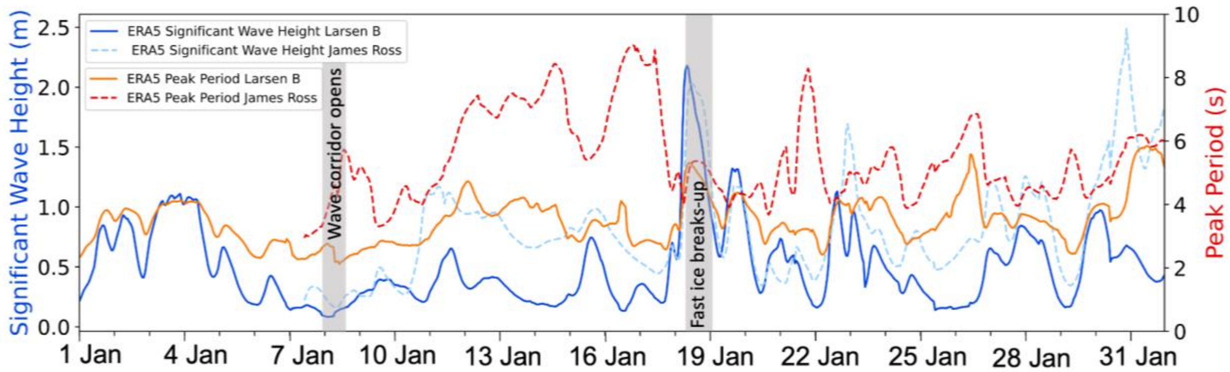

Figure 2.7: ERA-5 significant wave height (blue) and peak period (red) for both the Larsen B area (solid lines) and near James Ross Island (dashed lines) during January 2022. The red and dark red lines and the blue and light blue lines correspond to the peak period and significant wave height, respectively. The opening of the wave corridor and fast ice break-up are denoted by the gray vertical bands.

4.3 Initial glacier response to fast ice break-out

4.3.1 Retreat of glacier fronts

Four glaciers along the Larsen B embayment coast responded almost immediately to the fast ice break-out. Crane and Jorum Glaciers exhibited similar responses, losing most of their floating ice tongues within days of the fast ice breakout (Fig. 2.8a) and calving a number of large (several km^2) full-thickness tabular icebergs. Once the floating tongue portion was removed, both glaciers underwent buoyancy-driven calving and a tidewater-style retreat at their grounding zones, indicated by the presence of toppled icebergs in optical images and high-backscatter iceberg surfaces in Sentinel-1 data. Scattering intensity is related to surface roughness as well as how much melt has affected the surface of the berg; freshly toppled cold bergs will have a brighter surface, whereas tabular bergs that have been exposed to surface melt will display a decreased backscatter intensity (Young et al., 1998). Punchbowl Glacier began calving in a style that appears to be buoyant full thickness calving (Murray et al., 2015), indicated by toppled dark blue icebergs. Unlike Crane, Jorum, and HGE, Punchbowl did not readvance into the embayment during the fast-ice occupation. Hektoria and Green Glacier retained a 13 km extended thick (greater than 300 m) floating tongue after the immediate break-out, until March 2022. However, at this point their floating ice areas also underwent full-thickness tabular calving with occasional toppled icebergs (Fig. 2.8). From April to October 2022 the ice fronts were relatively stable, but rapid retreat reinitiated in November 2022. The calving style resembled tidewater glacier retreat for grounded ice with buoyant calving, similar to the Röhss Glacier response from the loss of the Prince Gustav Ice Shelf (Glasser et al., 2011) or calving regimes at Helheim Glacier, Greenland (Murray et al., 2015).

In the weeks and months following the fast ice break-up, Crane, Jorum, and Punchbowl glaciers continued to retreat. By 8 February 2022 the Crane Glacier floating front (defined here as the limit of contiguous ice > 100 m in thickness; consistent with Needell and Holschuh, 2023) had retreated more than 6.5 km and was still calving large tabular bergs (several km^2 and > 300 m thick, based on WV DEMs; Fig. 2.8a). From 8 February until 11 March 2022 only 400 to 800 m of retreat occurred. Crane continued its episodic periods of retreat of several hundred meters at a time throughout the 2022-2023 summer season (Fig. 2.8a). Its retreat totalled ~11 km, of which possibly 1 to 2 km was grounded ice using this study's grounding zone or no grounded ice using

Rott et al. (2018)’s, 2016 grounding line (Fig. 2.8b). Similar to Crane in calving style, the Jorum Glacier main trunk lost ~5 km of floating ice and its (former) tributary branch glacier lost ~6 km. Punchbowl Glacier, in contrast, has only lost a few hundred meters of its ice front as of May 1 2023.

Hektoria and Green Glacier responded to the fast ice break-out in later months. Hektoria Glacier had an extended thick (> 300 m) floating tongue that persisted until 12 to 17 March 2022, when it retreated ~7 km (Fig. 2.8c). From 26 to 30 March, Hektoria’s floating tongue retreated another ~6 km, exposing an arcuate ice front. From April 2022 until August, Hektoria’s ice front retreated ~1 km. This retreat is inferred to be the start of the grounded ice retreat based on a change in calving style and surface morphology of the upstream ice. For all of September and October Hektoria’s front did not change. Hektoria retreated ~3 km by 14 November and another 1.2 km by 30 November 2022. In December 2022, Hektoria underwent another series of retreats totaling ~4 km. From 17 January to 15 March 2023, another ~1.5 km retreat into the fjord occurred, and Hektoria is still actively retreating as of April 2023 and has retreated a total of ~25 km, of which ~10 km may have been grounded ice using this study’s grounding zone or 1 to 5 km of grounded ice using Rott et al., (2018)’s 2016 grounding line (Fig. 2.8d). Green

Glacier has also retreated substantially but not as far into its fjord. Following a similar timeline to Hektoria, Green has retreated ~18 km total.

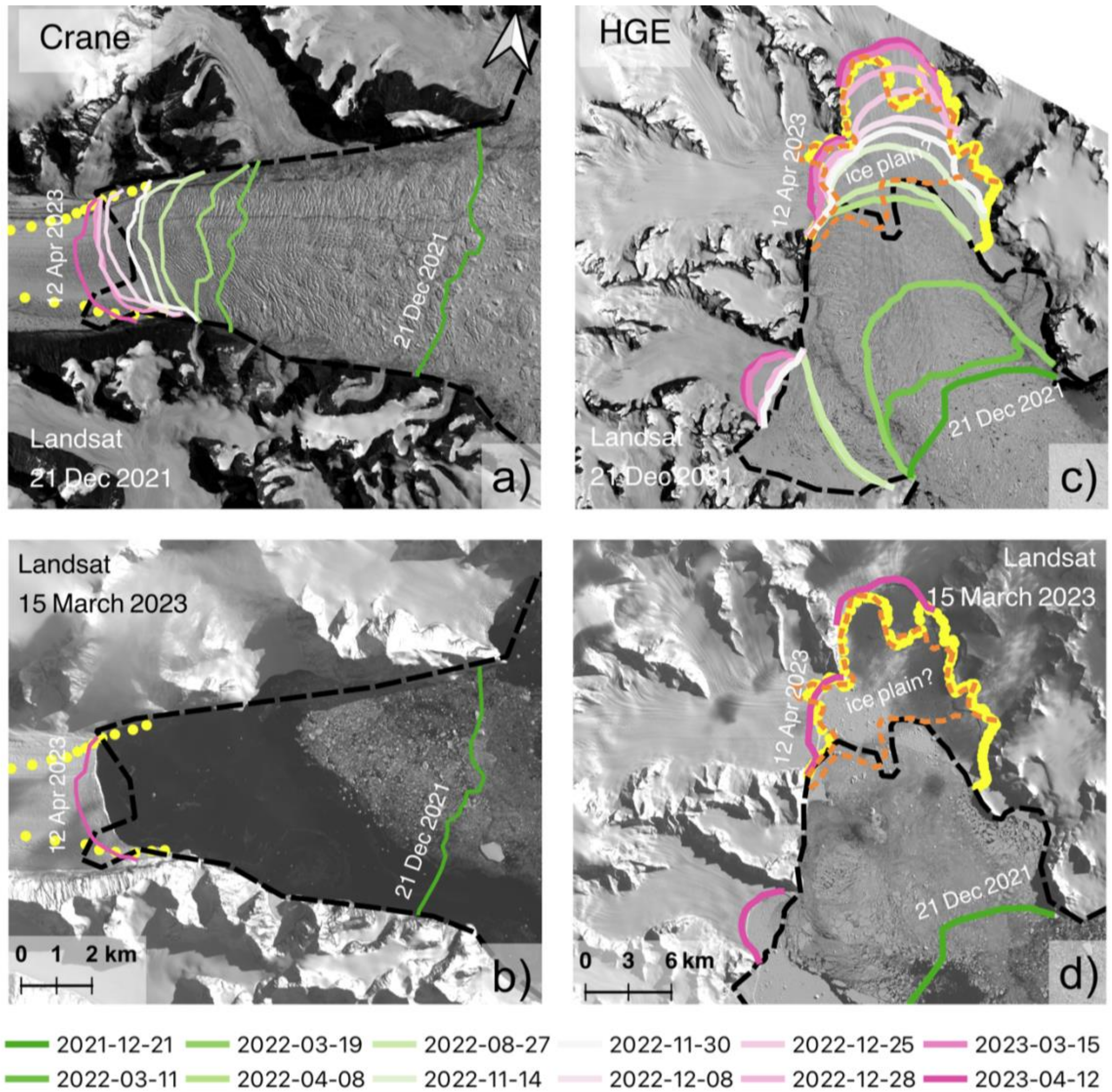

Figure 2.8: Yellow points are Rott et al., 2018's grounding zone, black dashed lines are this study's inferred grounding zone, orange dotted lines are Tuckett et al., 2020's grounding zone and ice plain location; a) Crane Glacier retreat fronts from November 2021 to April 2023, length scale is the same as panel b; b) Crane Glacier with pre-break out terminus position and April 2023 terminus position; c) HGE system retreat fronts from November 2021 to April 2023, length scale is the same as panel d; d) HGE system with pre-break out terminus position and April 2023 terminus position. For a) and c) the background is a Landsat 8 image from 21 November 2021, and for b) and d) the background is a Landsat 9 image from 15 March 2023.

4.3.2 Glacier centerline speed changes

Initial ice flow speed profiles along near-centerline tracks of Crane, Jorum, Green and Hektoria glaciers all show an increase in speed of various magnitudes since the fast ice break-out event. For all the glaciers besides Punchbowl, the floating portions increased in speed dramatically immediately after the break-out event while the grounded portion of the glaciers took many months to be affected, according to this study's grounding zone estimation (Fig. 2.9a-c; gray shaded bands on profiles and dashed white lines on insets). Additionally, the observed speed profiles in the 26-month period (January 2021 to March 2023) show far less local variability upstream of our inferred grounding line.

The Crane Glacier tongue accelerated and extended along-flow immediately after the event leading to an increase of speed from 1000 m yr^{-1} to 1300 m yr^{-1} within the first two months (Fig. 2.9a; light blue to yellow-green solid lines). The grounded portion of Crane Glacier responded in the months following. By November 2022 the grounded ice speed increased from 800 to 900 m yr^{-1} (Fig. 2.9a; yellow to dark-yellow solid lines) and by March 2023 the speed was 1200 m yr^{-1} (Fig. 2.9a; red solid lines). Crane Glacier is still undergoing retreat and acceleration as of March 2023.

Jorum Glacier did not experience as dramatic a change in speed after the event. Jorum Glacier has three flow speed sections: the upper glacier was slow-moving at 100 to 200 m yr^{-1}, the glacier's steep portion accelerated to 500 m yr^{-1} over a distance of 1.5 km, and the lower glacier flowed at ~475 m yr^{-1} prior to the break-out (Fig. A1-S10). By November 2022, this lower section increased in speed by ~75 to 100 m yr^{-1}, and has remained at ~550 m yr^{-1} as of

March 2023 (Fig. A1-S10). Jorum Glacier's floating tongue quickly calved away after the event so the floating icebergs and loose mélange were not tracked for speed.

The HGE system experienced significant changes after the break-up of the fast ice. While the floating portion of the system did not experience speed changes immediately after the fast ice loss (Fig. 2.9a-c; January to March 2022; light blue to yellow-green solid lines). The floating tongue was removed by April 2022 leaving only grounded ice, according to this study's grounding zone estimation. The mélange speed is tracked when the mélange is cohesive (solid lines downstream of this study's grounding line from April 2022 onwards), reaching ~1500 (Hektoria) and 1700 m yr^{-1} (Green) by October 2022.

Speed changes occurred in the lower trunk areas of both Green and Hektoria glaciers. Green Glacier increased from ~500 m yr^{-1} prior to fast ice break-up to 1150 m yr^{-1} by January 2023. Green Glacier's SAR-derived and Landsat-derived ice speeds for December 2022 and January 2023 agree with the general trend (Fig. 2.9b; light brown and brown solid lines). Hektoria Glacier's Landsat-derived ice speeds show a velocity increase 10 km upstream of the grounding line from September 2022 to January 2023 from 400 to 900 m yr^{-1} (Fig. 2.9c; light brown and brown solid lines). Both Green and Hektoria are still undergoing retreat and acceleration as of March 2023.

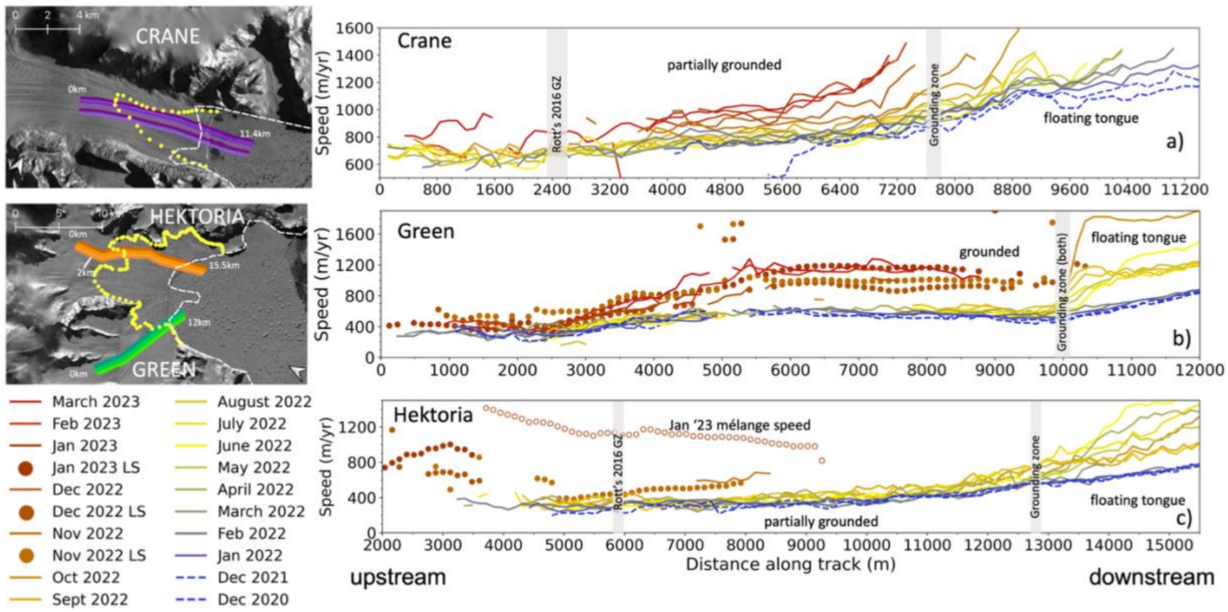

Figure 2.9: Monthly averaged ice flow speeds along the IceBridge flight centerlines, derived from Sentinel-1 speckle tracking from Alaska Satellite Facility HYP3-pipeline, solid-colored lines. Image pair flow speeds from Landsat imagery (using PyCorr) are indicated by colored solid dots. Gray bands on profiles and dashed white line on image insets show inferred grounding zones, with the Rott et al. (2018) grounding zone of 2016 as yellow points on insets. a) Crane Glacier velocity profile. b) Green Glacier velocity profile. c) Hektoria Glacier velocity profile. The open circles represent the melange speed from the January 2023 Landsat velocity data. The along-track distances are set at an arbitrary point well upstream of each glacier's grounding zone. Blue dashed lines are reference years Dec 2021 and Dec 2020, prior to break-out. Background image is a Landsat 9 image from 06 October 2022.

4.3.3 Elevation changes

We used ICESat-2 altimetry and WV-1, -2, and -3 stereo-image DEMs to assess elevation changes of the Larsen B embayment glaciers from 2017 to present. For each glacier, we evaluated three reference points along the near-centerline to these changes. Lower Crane Glacier (red box, Fig. 2.10) may have thinned by up to 16 m immediately after the fast ice break-out, however the trend is incomplete due to the glacier's rapid retreat and calving. This abrupt thinning may have been a consequence of a change in calving style near the front, e.g., listric faulting in the ice (e.g., Parizek et al., 2019). Our trend for the middle and upper section of Crane (orange and blue box, Fig. 2.10) shows thickening from 2017 to 2022, consistent with Needell and Holschuh's (2023) findings. Thinning may have now begun in those regions, however the data are inconclusive, as the thinning is only 1 to 3 m as of February 2023, which is within the measurement error and surface roughness variations on the glacier. Jorum and Punchbowl glaciers show very variable results as well (Fig. A1-S11).

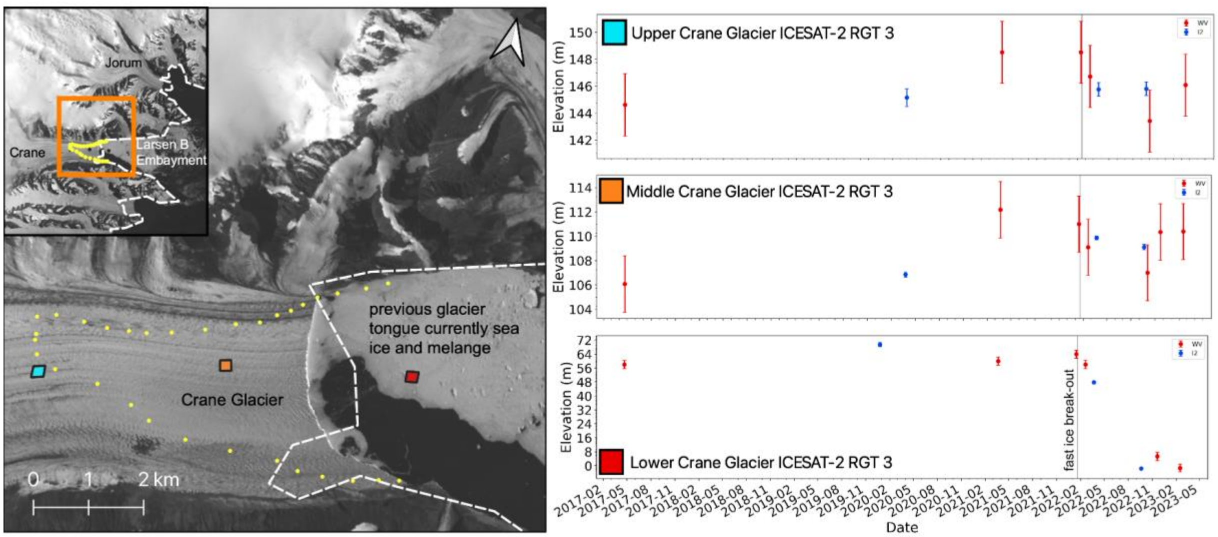

Figure 2.10: Crane Glacier near-centerline elevation changes through time. Background image is from Landsat 9 17 January 2023 Landsat. The time series plot corresponds to the area of the box of the same color. The gray band indicates the date of the fast ice break-out event. Note the different vertical scales on the figure.

The HGE system shows thinning in various regions and rapid calving and retreat in the elevation data.. Figure 2.11 (yellow box) shows the HGE system floating tongue freeboard as 40 m, which is consistent with a ~320 m glacier thickness, assuming hydrostatic equilibrium. After the break-out event, icebergs (which we define as ice with >5 m freeboard) are present in the fjord until the open ocean period (December 2022). Lower Hektoria Glacier lacks elevation change data points from the start of the collapse, simply because the downstream-most regions calved and drifted away before a repeat elevation measurement could be acquired (blue and green boxes; Fig. 2.11). The upper portion of Hektoria (dark orange box; Fig. 2.11) appears to have thinned since early 2018 (or prior). Minimal thinning occurred from April 2022 to late December 2022. As of 6 April 2023, this portion of the glacier is just 400 m upstream from the rapidly retreating glacier terminus and is unlikely to remain intact for further measurements. Both the lower and upper Green Glacier (orange and blue boxes, respectively; Fig. 2.11) show strong thinning above the level of surface variability from 2017-present. Lower Green Glacier thinned ~11 m between March 2022 to late December 2022, going from 79 m to 68 ±2.3 m. Upper Green Glacier thinned ~9 m between January 2021 to late December 2022, going from 162 ±0.5 m to 153 ±2.3 m. There are no data available between January 2021 and July 2022, so the initiation of thinning of the glacier is uncertain. However, from July 2022 until late December 2022, ~5 m of the total 9 m of thinning occurred.

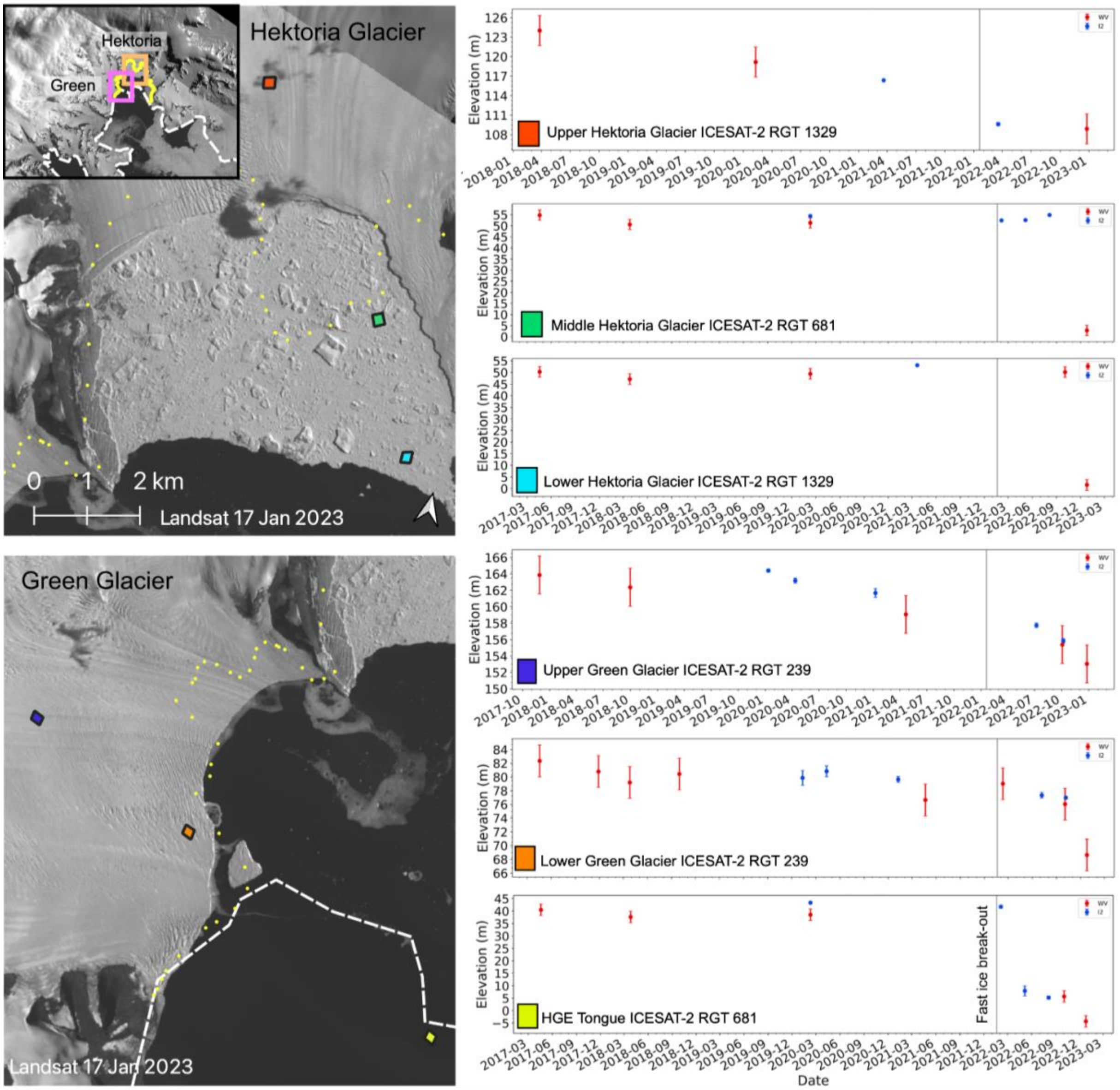

Figure 2.11: Hektoria and Green Glacier system elevation changes through time. Background image is from Landsat 9 17 January 2023 Landsat, yellow points indicate the Rott et al. (2018) 2016 grounding zone and white dashed line is the grounding zone inferred in this study. The pink box in the study area inset is the area depicted for Green Glacier and the orange box is Hektoria Glacier. The time series plot corresponds to the area of the box of the same color. The gray band indicates the date of the fast ice break-out event.

5 Discussion

Figure 2.12 summarizes the chronology of events in the 22-year period from 2001-2023 of the Larsen B embayment and the tributary glaciers. We document the changes that have occurred during the two break-out events and how the glaciers and the Scar Inlet Ice Shelf have responded to those events. Below we discuss the conditions and aftermath of the 2022 event in light of our findings and related literature.

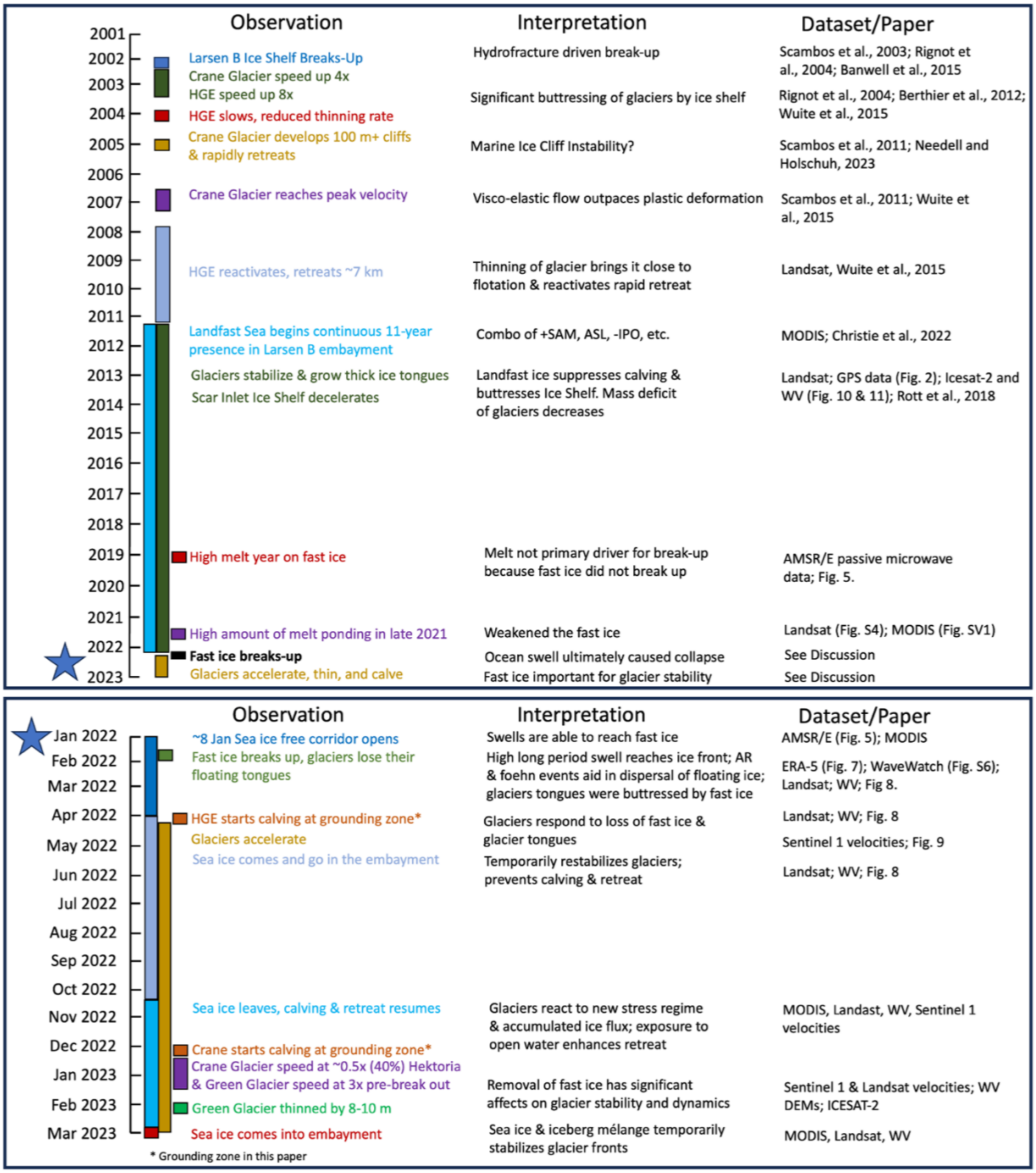

Figure 2.12: Schematic of the chronology of events from 2001-2023 of the Larsen B embayment region discussed in the text.

5.1 Meteorological Conditions and Modes of Atmospheric Variability

The AP climate is influenced by several large-scale modes of atmospheric variability. These patterns are drivers of the formation and demise of pack ice, fast ice, the mass balance and stability of the glaciers and ice shelves. Climate patterns and variability are driven by several modes with a variety of time scales, e.g., the Interdecadal Pacific Oscillation (IPO) at 10 to 30 years and SAM phase oscillations, changing on the scale of weeks to months. The IPO was in a negative phase from 2000 to 2014, favoring an increase of overall sea ice extent at $\sim 0.57 \pm 0.33 \times 10^6$ km^2 per decade (Meehl et al., 2016). Additionally, slightly cooler conditions around the AP in the 2010s limited the area of melt ponding on the Scar Inlet Ice Shelf and the northern Larsen C (Cape et al., 2015; Bevan et al., 2018). This situation paired with intensified cyclonic circulation in the Weddell Sea (Christie et al., 2022), which may be broadly favorable for the formation of the Larsen B embayment fast ice and advancement of the glacier tongues (Fig. 2.12), yet due to local variability it can be difficult to pinpoint its exact drivers in a specific season. It appears the IPO reversed in 2015/2016 but that remains to be confirmed (Li et al., 2021). The SAM index has been trending toward more frequent periods of positive phase for many decades (Kwon et al., 2020; Li et al., 2021). A positive SAM is generally associated with a deepening of the Amundsen Sea Low, which subsequently enhances northwesterly flow across the AP, bringing warm air masses and an increase in foehn events into this region (Li et al., 2021; Turner et al., 2022). A positive SAM is also correlated with AR events, due to enhanced moisture fluxes towards the Antarctic Peninsula and a more easterly storm track, which can increase warming on the eastern (lee) side of the Antarctic Peninsula during AR-driven foehn events (Wille et al., 2021; Shields et al., 2022; Wille et al., 2022). Strong westerly winds increase pack ice drift eastward and northward, exposing the AP's eastern coast and ice fronts to open ocean. This may have caused the low sea ice cover in the Weddell Sea in summer 2021/2022 and lack of pack ice in the corridor region in January 2022 (Turner et al., 2022).

We found that the climate of the Larsen B region was anomalously warm from November 2021 to January 2022. However, despite the climate being warmer, the number of melt days, and mean areal extent of melt, over the fast ice derived from the passive microwave data in the 2021/2022 season were not a record (Fig. 2.5). According to the optical imagery, melt ponds were evident in Landsat 8 satellite images mainly in November and December 2022, however the areal extent of melt ponds in the Larsen B region declined prior to the fast ice break-out event in late January 2022 (Fig. A1-S6). These observations suggest that neither surface melting, nor related hydrofracturing of pre-existing melt ponds in the thick glacier tongues, were a direct cause of the 19 January fast ice fracturing or the subsequent break-up, although they do point to a warmer (and likely weaker) fast ice cover at mid-summer of 2021/2022.

The low overall sea ice concentration and westerly winds from a deep Amundsen Sea Low led to an open water corridor between the pack ice and the eastern coast of the AP (Turner et al., 2022). This led to the region in front of the Larsen B having the lowest total overall sea ice area for the date in 13 years (2010-2022; Fig. 2.6). In February 2021, there was a smaller open corridor, however, the area was not as wide as in early January 2022 and did not create an unobstructed ice-free lane to Southern Ocean swell. With low sea ice damping, ocean swell events could impact the eastern fast ice and coastal areas; these have been shown to destabilize fast ice and ice shelves (Crocker and Wadhams 1989; Langhorne et al. 2001; Banwell et al., 2017; Massom et al., 2018; Teder et al., 2022). However, swell events in February 2021 were low amplitude or proceeded from the coast to the northeast, i.e. likely driven by foehn events.

5.2 The fast ice break-out event

Despite high temperatures and surface melt and meltwater ponding (Scambos et al., 2003; Banwell et al., 2013), alongside thinning due to both basal melting and surface melting (Adusumili et al., 2018; Smith et al., 2020), known to be primary drivers of ice shelf collapse, our analysis shows that the Larsen B multi-year fast ice persisted through warm and high melt years (e.g., 2019/2020; Bevan et al 2020; Banwell et at., 2021) without breaking up. Until the 2021/2022 melt season, the absence of a large sea ice-free corridor prevented high ocean swells from the northeast from reaching the fast ice (Fig. 2.12). Long period ocean swells, such that the wavelength is substantially greater than the ice thickness, can expose ice shelves and fast ice to flexural strains (Crocker and Wadhams, 1989; Langhorne et al. 2001; Banwell et al., 2017; Massom et al., 2018). In our case, the fast ice was several meters thick, wave height was nearly 1.75 m, and the wave period at the time of the event was 5 to 6 s, corresponding to wavelengths of order of 40 m (Fig. 2.7). The resulting strains can weaken the outer margins of the fast ice or ice shelf through plate-bending and fracturing. As the outer margin breaks, the stress is redistributed within the fast ice, possibly initiating further fractures within the ice (Massom et al., 2018). The fast ice was potentially preconditioned to break-up by the rifts that were open near the confluence of the Crane Glacier tongue and Scar Inlet Ice Shelf, however, contrary to Sun et al. (2023) we attribute the break-up to the long period, high-amplitude swell that came from the northeast through the open sea ice corridor. This order of events and ultimate cause of break-up is similar to what was proposed in Gomez-Fall et al. (2022) for the collapse of the Parker Ice Tongue.

The rapid removal of the fast ice fragments from the embayment coincides with the presence of foehn winds that were likely caused by an AR event. Recently, ARs and AR-triggered foehn events have been linked to the collapse of ice shelves due to their ability to cause extreme surface melting and subsequent hydrofracture (Laffin et al., 2022; Wille et al., 2022). Here, we found that foehn events happened prior to, during, and after the January 2022 Larsen B wave event. We cannot rule out the possibility that these foehn events may have sufficiently increased melting on the thick glacier tongues to cause hydrofracturing, which may have acted to further fracture the fast ice and facilitate break-up. As a secondary driver, the winds likely hastened the removal of the floating ice or helped create the open corridor for wave entry to reach the ice fronts. These findings parallel that of Massom et al. (2018) who attributes the Larsen B Ice Shelf break-up in 2002 to the removal of sea ice due to westerly/north westerly winds that not only enabled an ocean swell to reach the ice shelf but also helped to quickly evacuate large icebergs and mélange out of the embayment. Additionally, the AR and foehn events in January 2022 may have affected sea surface slope. It is possible that a sea surface sloping oceanward gravitationally promoted calving and removal of the floating ice, similar to the calving of large icebergs off the Amery Ice Shelf in 2019 (Francis et al., 2021), the Brunt Ice Shelf in 2021 (Francis et al., 2022), and Larsen D in 2020 (Christie et al., 2022). We suggest further research to investigate the presence of cyclone(s) and the sea surface slope during the time of the break-up event.

5.3 The initial glacier response

After the break-up of the ice shelf in 2002, the presence of fast ice significantly affected the tributary glaciers' dynamics, providing sufficient backstress that suppressed calving and permitted the tributary glaciers to form thick ice tongues and readvance into the embayment during 2010 to 2022 after the initial break-up in 2002 (Fig. 2.2; Needell and Holschuh, 2023), corresponding to an Eastern Antarctic Peninsula-wide ice front advance discussed in Christie et al. (2022). Rigid mélange and/or fast or pack ice can stabilize rifts (Larour et al., 2021), and can allow ice shelves, tidewater glaciers, or floating glacier tongues to advance, as has been seen in

Greenland (Moon et al., 2015), the Parker Ice Tongue (Gomez-Fell et al., 2022), the Cook West Ice Shelf (Miles et al., 2018), and other areas (Reeh et al., 2001; Massom et al., 2010; Cassotto et al., 2015; Banwell et al., 2017). During the 2010 to 2022 period of the occupation of the Larsen B multi-year fast ice, the tributary glaciers Crane, Hektoria and Green readvanced and decelerated (Rott et al., 2018) and the Scar Inlet Ice Shelf decelerated with clear seasonal variability associated with the presence of the fast ice (Fig 2). The loss of fast ice can affect the seasonal variability of velocity and calving dynamics of ice shelves, as seen for the Totten Ice Shelf (Greene et al., 2018) and Parker Ice Tongue (Gomez-Fell et al., 2022). Due to the fast ice moving as a cohesive unit coupled with the lack of iceberg rotation embedded in the fast ice, suggests a degree of mechanical coupling of the glacier tongues, and Scar Inlet Ice Shelf, to the fast ice, similar to the relationship of mélange and multiyear fast ice for the Voyeykov Ice Shelf prior to disaggregation (Arthur et al., 2021). The Larsen B fast ice played an integral role in the growth, deceleration, and stability of the Larsen B outlet glaciers, their floating tongues, and the Scar Inlet Ice Shelf. Given that the fast ice was 5-10 m thick, it likely provided backstress greater than the 10^7 N m^{-1} threshold required to suppress calving (Robel, 2017). Contrary to recent modelling results (Sun et al., 2023; Surawy-Stepney et al., 2023), in absence of any other plausible cause, our observations show the loss of the fast ice led directly to dramatic dynamical changes in the aforementioned tributary glaciers tongues and thereafter the subsequent grounded glaciers.

According to de Rydt et al. (2015), an “immediate” glacier response is one that occurs < 2 years after an initial event. Here we see an immediate disaggregation of the glacier tongues after the fast ice broke out. These responses mimic Voyeykov Ice Shelf where over the course of several months the ice shelf lost stabilizing land fast ice, then mélange, followed by partial loss of the ice shelf (Arthur et al., 2021). The immediate complete disaggregation of multiple floating ice tongues after the loss of the fast ice suggests that the fast ice was not only preventing calving but also supplied sufficient backstress that essentially held the tongues together. The glacier speeds began to gradually increase after the loss of their thick floating tongues (Fig. 2.9).

The calving regimes and dynamical changes of the Larsen B tributary glaciers are similar to their response after the 2002 Larsen B ice shelf disintegration, suggesting that calving is an immediate response to stress perturbations (Hulbe et al. 2008). At first glance, the two events were quite different; for example, the tributary glaciers were stable prior to the 2002 event and though they were readvancing and stabilizing prior to the 2022 event they were still in an imbalanced state (Seehaus et al., 2023), additionally the ice shelf was old and thick whereas the fast ice was much younger and an order of magnitude thinner. However, despite these differences, the similarities in the tributary glacier response to the two events are important to identify.

Crane Glacier experienced significant changes after the Larsen B Ice Shelf disintegration and fast ice break-out. In the three years following the Larsen B Ice Shelf disintegration event (2002 to 2005), the Crane Glacier ice front and grounding zone retreated 18 km into the fjord, and the ice front height increased from 60 m to just over 100 m (Scambos et al., 2011, De Rydt et al., 2015). Simultaneously, the glacier trunk upstream of the ice front lost elevation at a rate of 35 m yr^{-1} (Shuman et al., 2011). As of March 2023, the 2022 event has caused Crane Glacier to retreat ~11 km in 14 months (Fig. 2.8). However, significant thinning in the upstream areas has yet to occur (Fig. 2.10). Between 2002 and 2003, Crane Glacier ice flow increased rapidly, roughly 3-fold from ~500 m yr^{-1} to ~1500 m yr^{-1} (Rignot et al., 2004). In 2007, Crane's terminus had speeds up to ~ 3500 m yr^{-1} with a steady deceleration the following years (Wuite et al., 2015). By 2017 terminus speeds were ~1000 m yr^{-1} (Rott et al., 2020) and remained that way until the break-out. In what is likely grounded ice (relative to both the grounding zone locations in this study and in Rott et al., 2018), speeds prior to the break-out were ~750 m yr^{-1} and subsequently increased to ~1050 m yr^{-1} by early 2023 (Fig. 2.9). Crane Glacier has responded similarly to the two episodes of buttressing loss in the last 20 years, although the magnitude of change was greater in the immediate aftermath of the 2002 event (Fig. 2.12).

Hektoria's calving in 2022 is similar to the 2002 event where initially floating tabular bergs calved and then an arcuate calving front formed with large rifts and slumping. In 2022/2023, Hektoria retreated ~25 km, with ~10 km of that retreat (or 1 to 5 km referencing the Rott et al.'s 2016 grounding line (Rott et al., 2018); Fig. 2.8) likely to be partially grounded ice on an ice plain (Tuckett et al., 2020). This is greater than the 2002 event in which Hektoria lost ~15 km of floating ice in the first year and it was not until a year after the loss of the ice shelf in 2003 that Hektoria began calving at its grounded terminus (Rack and Rott, 2004). This could possibly be explained with the lower Hektoria glacier being much closer to floatation in 2022 than it was in 2002 and possibly with a higher amount of accumulated damage. In that case, acceleration and thinning would have first been needed to bring the Hektoria Glacier to a height near floatation before significant retreat of grounded ice could occur after the 2022 event. In 2002 to 2003 Hektoria's ice flow speeds increased 8-fold from ~250 m yr^{-1} to over ~2000 m yr^{-1}. Hektoria's terminus retreat paused from 2007 to 2009 and then reactivated in 2009 until the long-term fast ice formed in the embayment and stabilized the front in 2011 (Fig. 2.12). Following the fast ice breakout several kilometers upstream of the grounding line, Hektoria's ice flow speeds increased from 400 m yr^{-1} to ~900 m yr^{-1} (Fig. 2.9). Although the magnitude is not as great as the 2002 event, the glaciers have had a dramatic acceleration. Hektoria's thinning from 2002 to 2003 was between 5 to 38 m yr^{-1} (Scambos et al., 2004), whereas the 2022 event resulted in thinning of between 8 to 11 m on Green Glacier from March 2022 to January 2023 (Fig. 2.11). Again, this is a similar and only slightly subdued response to the loss of embayment ice.

Both Crane and Hektoria experienced rapid changes after both the 2002 and 2022 events. The speed up of both glaciers was immediate, yet gradual, as the evolution of the system adjusted to new geometry, particularly the glacier bed. This gradual, slightly delayed increase in velocity may be why Sun et al. (2023) did not capture the acceleration as their velocity data ended in July/August 2022 and the majority of the acceleration took place after that (Fig. 2.9). However, that is along the same timeline of changes experienced in the 2002 event as the first velocity data was only available December 2002, nine months after the ice shelf break-up (Wuite et al., 2015). Comparison of the speeds, thinning, and retreat rates, reveals that the 2002 event had a greater impact on the glacier dynamics within the first year of the loss of ice shelf/multi-year fast ice buttressing. This is an expected response, as the loss of the Larsen B Ice Shelf should result in a higher de-buttressing effect than the more recent loss of the much thinner fast ice and thick glacier tongues.

6 Conclusions

The climate of the AP has been warming over the past several decades (Vaughan et al., 2003; Zagorodnov et al., 2012), interrupted by a decade-scale cooling that coincided with the formation of the fast ice in 2011 (Turner et al., 2016). During the 2021/2022 summer, the Larsen B region of the AP experienced anomalously high temperatures, and strong westerly winds contributed to an ice-free corridor to open along the eastern coast of the Peninsula that in turn allowed long-period high amplitude ocean swell to reach the fast ice. In the 2021/2022 summer the Antarctic sea ice extent was at its lowest sea ice extent in the satellite record (prior to 2023) with the Weddell Sea contributing 26% to that negative anomaly (Turner et al., 2022). The sea ice extent in the Weddell Sea in 2022 was the 12th lowest in the satellite record (Turner et al., 2022) and the pack ice area immediately near the Larsen B embayment was at its lowest since 2010.

The large-amplitude wave event with a long period swell that occurred 18 to 19 January reached the fast ice front via the pack ice-free corridor. We infer that this flexed the fast ice, causing it to fracture and redistribute the stresses within the thin ice plate, which would be seasonally at its weakest due to the recent warm air temperature. We note, however, that surface meltwater-induced flexure and hydrofracture of the glacier tongues do not appear to play a direct role in this case. An AR and foehn wind event occurred during and after the fast ice break-out, contributing to the quick removal of the fast ice from the embayment.

All of the glacier responses following the Larsen B embayment fast ice break-out are reminiscent of the effects on glacier flow and decreased surface elevation after the Larsen B ice shelf removal (i.e., extreme and varied; Rignot et al., 2004; Scambos et al., 2004), despite the fast ice being substantially thinner than the ice shelf (5 to 10 m compared to ~250 m; Fig. 2.1) and the glaciers being in different states prior to the break-outs (Seehaus et al., 2023). We conclude that the fast ice slab was acting to significantly buttress the glaciers' floating tongues, and its removal led to the disaggregation of the tongues and destabilization and dynamical changes of the grounded glaciers.

Antarctica's coastline is fringed with multi-year fast ice (Fraser et al., 2021) that is likely buttressing large glaciers around the continent. As the climate continues to change (Gilbert and Kittel, 2021), Antarctica's fast ice may become more susceptible to breakup due to increasing exposure to ocean swells via open-ocean corridors through pack ice (Reid and Massom, 2022;

Teder et al., 2022). As Antarctic overall sea ice concentrations are projected to decrease over the current century (Holmes et al., 2022), this risk is inherently higher. Antarctic-wide fast-ice-buttressed glaciers will likely be subject to substantial dynamical changes and potential retreat if pack ice decline leads to multi-year fast ice break up.

This case study affirms the importance of examining the impacts of large-scale circulation patterns on foehn conditions, overall sea ice area, and ocean swells on the AP and other vulnerable ice shelf and outlet glacier areas. It is important to continue monitoring not only the glaciers feeding into the Larsen B embayment in terms of their response to changing fast ice conditions, but also other key glacier-ice shelf-fast ice interactive systems around Antarctica and their response to increased coastal exposure (Reid and Massom, 2022; Teder et al., 2022)

Acknowledgements

We would like to thank Chris Shuman and Mark Fahnestock for their help in monitoring the break-out and suggesting processing tools, as well as Bertie Miles for the suggestion on how to extract velocity profiles. We also thank the British Antarctic Survey pilots who captured images of the initial fast ice break-up on 31 January 2022, and the NSIDC for data access and technical support. NEO and TAS received support from NASA award 80NSSC22K0386 and USGS award 140G0118. AFB received support from the U.S. National Science Foundation (NSF) under award no. 1841607. GPS data was collected using the LARISSA award NSF OPP 0732602 and NSF OPP 0732921.

Author Contributions

NEO led the study, processed and analyzed the data, and led the writing of the manuscript. TAS initiated the idea and outlined the direction of the study with early data. GP processed the raw AMSR data to detect liquid water and AFB analyzed these data and produced Figure 2.5. RSA, SM, and LM contributed to the plan of the research. MLM analyzed the AR events. JAS contributed to the climate analysis methods. MT and ECP processed and analyzed the GPS data. All authors contributed to the writing of the manuscript and discussion of results.

Data Availability

Sea ice concentration and extent data are available on the University of Bremen sea ice webpage (https://seaice.uni-bremen.de/sea-ice-concentration/amsre-amsr2). Operation IceBridge data is available at NSIDC (https://nsidc.org/data/icebridge) as well as the ICESat-2 data (https://nsidc.org/data/atl06/versions/6). Velocity data are available from the Alaska Satellite Facility Sentinel-2 AutoRIFT pipeline (https://search.asf.alaska.edu). MODIS imagery can be viewed and downloaded on the Worldview interface (https://worldview.earthdata.nasa.gov). ERA-5 data are available at the Copernicus data store (https://cds.climate.copernicus.eu/cdsapp#!/home). WaveWatch III data are available on CSIRO (https://data.csiro.au/collection/csiro:39819). The AMSR-E/2 data are available to download here: https://perscido.univ-grenoble-alpes.fr/datasets/DS391. The Reference Elevation Model of Antarctica is available via the Polar Geospatial Center (Howat et al., 2022, https://www.pgc.umn.edu/data/rema/). The Worldview DEMs are available from Polar Geospatial Center upon request. The overview panel of Antarctica in Figure 2.1 is from Quantarctica (Matsuoka et al., 2021; https://www.npolar.no/quantarctica/)

CHAPTER 3

Record rate of tidewater glacier retreat at Hektoria Glacier, Antarctic Peninsula

This chapter will be submitted to Nature Geoscience in November 2024.

Coathors: Naomi Ochwat, Ted Scambos, Robert S. Anderson, J. Paul Winberry, Adrian Luckman, Etienne Berthier, Maud Bernat, and Yulia K. Antropova

Abstract

Hektoria Glacier on the Eastern Antarctic Peninsula underwent an unprecedented rate of tidewater-style glacier retreat from 2022 to 2023 after the loss of decade-old fast ice in the Larsen B embayment in January 2022. The glacier retreated ~25 km between February 2022 and March 2023. In two months, November to December 2022, ~10 km of grounded ice calved; a retreat rate an order of magnitude faster than any reported in the modern record. Following the fast ice break-out, a 6-fold ice speed increase resulted in a 40-fold increase in the glacier thinning rate. In November 2022, Hektoria Glacier transitioned from calving large tabular icebergs to buoyancy-driven calving associated with the change in basal shear stress where the glacier was grounded. We infer that the record retreat was accomplished by an extremely rapid calving style resulting from ice plain bed geometry. The Hektoria case implies that glaciers with ice plain bed geometry can be easily destabilized by loss of buttressing features.

1 Introduction

Glaciers that feed ice shelves or landfast ice areas (hereafter, ‘fast ice’) are subject to dynamical changes upon the removal of the buttressing features (Fürst et al., 2016; Greene et al., 2018; Ochwat et al., 2024). As the climate continues to warm, ice shelves and multi-year fast ice are increasingly susceptible to collapse (Gilbert and Kittel, 2021), thus exposing the glaciers to new stress regimes and external forcings. These dynamical changes have been documented and investigated in detail on the Antarctic Peninsula (AP) following the loss of the Prince Gustav Ice Shelf (Glasser et al., 2011), Larsen A and Larsen B Ice Shelves (e.g. Rott et al., 1996; Rott et al., 2002; Rignot et al., 2004; Scambos et al., 2014; Royston et al., 2016), the Wilkins Ice Shelf (Rankle et al., 2017), and others. These areas provide a natural observatory to examine potential feedbacks and instabilities that may occur in other, larger, glaciers that have at-risk buttressing floating ice.

In particular, the Larsen B ice shelf and tributary glaciers were relatively stable until the mid-1990s. In March 2002 the ice shelf broke up over several weeks, initiating a substantial change in the glaciers that fed it (Hulbe et al., 2008). The glaciers rapidly retreated into their fjords, thinned, and sped up (Scambos et al., 2004; Wuite et al., 2015). In 2011, the embayment filled with fast ice, partially stabilizing the glaciers, allowing them to advance into the embayment (Needell and Holshuh, 2023; Ochwat et al., 2024). In 2022, the decade-old fast ice broke out causing the glaciers to lose their 300+ m thick floating ice tongues and rapidly retreat (Sun et al., 2023; Ochwat et al., 2024; Surawy-Stepney et al., 2024). Ochwat et al. (2024) documents the triggers that caused the fast ice to break-out and the initial glacier acceleration and thinning until spring 2023. Ochwat et al. (2024) found that Crane, Hektoria, Green, and Jorum Glaciers began to accelerate, up to 2-fold. However, significant thinning had yet to occur at their specific study sites with only 5-10 m measured on Green Glacier. The authors did not examine Hektoria Glacier's extraordinary retreat.

Analogues for unusually rapid retreats are seen in Alaska, Greenland, Antarctica, and Patagonia. Pfeffer (2007) defines "rapid" as retreat rates that are greater than 200 m yr^{-1}, for example Columbia Glacier, Alaska, was known for its retreat rates of 1000 m yr^{-1} between 1980-2005 (Pfeffer, 2007; O'Neel et al., 2005). The LaConte Glacier, Alaska, retreated 2 km in ~6 years (O'Neel et al., 2001). In central western Greenland, rapid retreats of several hundred meters per year are observed (Catania et al., 2018). On the Antarctic Peninsula, Röhss Glacier retreated 15 km in ~8 years after the loss of the Prince Gustav Ice Shelf (Glasser et al., 2011). The Upsala Glacier East, Patagonia, a lake-terminating glacier, rapidly retreated in the 1980s at 440 m yr^{-1} (Warren et al., 1995) and 1000 m yr^{-1} between 2008-2011 with 40 m yr^{-1} of thinning (Sakakibara et al., 2013). With the exception of some lake-terminating glaciers, rapid retreats are usually restricted to tidewater glaciers.

The typical tidewater glacier cycle includes a period of rapid retreat (Meier and Post, 1987, Pfeffer, 2007). A tidewater glacier builds an underwater shoal from sediment transport as it advances. When the glacier advances into deeper water, sediment transport is no longer sufficient to maintain a shoal of necessary size for the water depth, and the glacier begins to thin and undergo a period of rapid retreat until it reaches a new equilibrium and begins building a new shoal (Brinkerhoff et al., 2017). However, in the Antarctic, coastal glaciers usually feed ice shelves or ice tongues and do not undergo the cyclical processes of classic tidewater glaciers. Instead, the removal of buttressing features (ice shelves or multi-year fast ice), may promote the transition of Antarctic glaciers to a tidewater geometry.

Rapid retreats in Antarctica have been associated with the proposed Marine Ice Cliff Instability (MICI) as the driving cause of retreat and not the tidewater glacier cycle (Alley et al., 2023). MICI is a consequence of high (>100 m) unsupported marine-terminating ice cliffs, resulting in very high ice-front stresses that can rapidly accelerate ice-front calving (Bassis and Walker, 2012; Pollard et al., 2015; Parizek et al., 2019). The Marine Ice Shelf Instability (MISI), on the other hand, is the hypothesis that outlet glaciers retreating into retrograde slopes will undergo a rapid grounding line retreat, creating a thick floating or near-floating ice front area driven by the increased ice thickness to flow rapidly, ultimately resulting in ice sheet collapse (e.g., Schoof, 2012; Joughin et al., 2014; Favier et al., 2014; Gudmundsson et al., 2019). Retreat of the grounding line, in a retrograde slope or flat glacier bed geometry may initiate rapid calving and instabilities are not limited to MISI (Sergienko, 2022). Recently, Batchelor et al. (2023) interpreted bathymetric geomorphological data in Norway as a setting in which a nearly planar bed profile (an ice plain) promoted rapid buoyancy-driven glacier retreat (Batchelor et al., 2023). Friedl et al. (2020) suggests that the presence of an ice plain allows a large region of the glacier to reach flotation simultaneously upon thinning.

In this study, we characterize the rapid retreat of Hektoria-Green (HG) Glacier, specifically Hektoria Glacier. The HG system underwent an unprecedented tidewater-style glacier retreat, receding ~25 km (~300 km^2) in 14 months, 10 km of which was Hektoria's grounded ice, measured along the central flowline (Fig. 3.1 and A2-SV1; Ochwat et al., 2024) This retreat is an order of magnitude greater than any known tidewater glacier retreat. First, we analyze the location of the grounding line prior to the loss of the Larsen B fast ice that includes utilizing several remote sensing and geophysical datasets. We include an evaluation of the calving style and characteristics of the glacier terminus and icebergs during the retreat. Lastly, we propose the 2022-2023 rapid retreat was due to buoyancy-driven calving over an ice plain area.

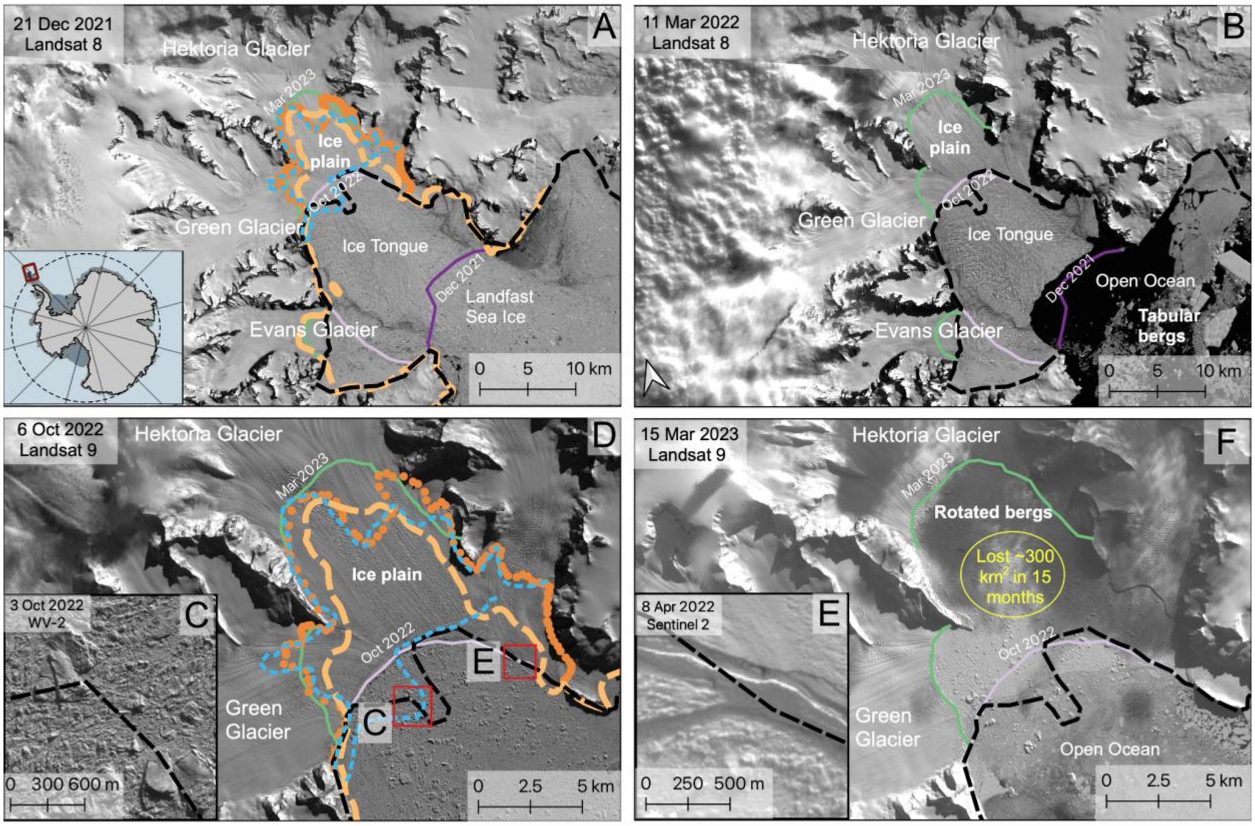

Figure 3.1: The retreat of Hektoria and Green Glaciers. A) Hektoria and Green glaciers prior to the loss of the fast ice; B) March 2022 image displaying the retreat of the floating ice tongue; C) Toppled icebergs that are present after the loss of the ice tongue; D) October 2022 image showing Hektoria and Green Glacier prior to the period of rapid retreat; E) forwardly rotated iceberg at the calving front in April 2022 at the transition from floating to grounded ice; F) Image of the new stable terminus location of Hektoria Glacier in March 2023. In panels A and B, several proposed grounding lines are displayed; the black dashed line is a 2021 grounding line (1; panels C and D), the light orange dashed line is a 2019 grounding line (50), the dark orange points are a 2016 grounding line (49), the blue small dashes are a 2016 grounding line (41). The green line is the March 2023-February 2024 terminus position, light purple is the terminus from August – October 2022, the dark purple is the terminus in December 2021 prior to the fast ice collapse.

2 Results

2.1 Assessment of the phases of the 2022-2023 retreat

After the loss of the Larsen B fast ice the Hektoria-Green glacier system underwent three phases of retreat, identified by iceberg morphology and calving style (Fig. 3.2). Tabular bergs are identified by their aspect ratio, dark rough surface, and they resemble the glacier surface near the retreating ice front (Sulak et al., 2017; Alley et al., 2023). The first phase of retreat occurred immediately after the loss of the fast ice, February-March 2022 (Fig. 3.2), when the 300+ m thick (Ochwat et al., 2024) floating ice tongue disaggregated and drifted away (Figs. 3.1A, B, D, and Fig. 3.5C). During this period the HG lost ~216 km^2 of the floating ice tongue, with a total of 16 km of retreat at a retreat rate of up to 0.8 km day^{-1}.

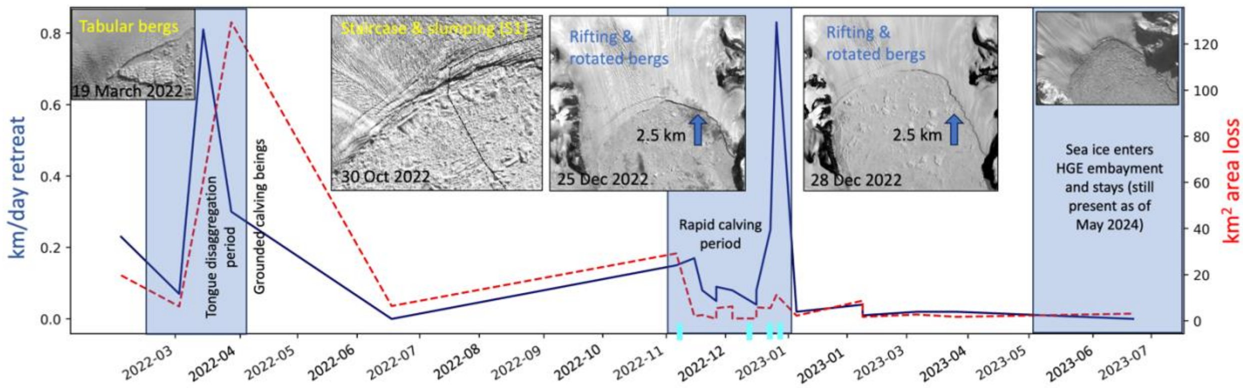

Figure 3.2: Hektoria Glacier retreat rates and area loss over the period of February 2022 until August 2023. Blue ticks are glacier earthquakes on 6 November 2022, 12 December 2022, 23 December 2022, and 25 December 2022; seismograms are in Supplemental Figure A2-S6. Inset panels show the glacier morphological changes that occurred during the key periods of retreat. “Tabular bergs” is from Landsat 9 on 19 March 2022, “Staircase and Slumping” is from Worldview 30 October 2022, “Rifting and Rotated Bergs 1” is from Landsat 9 on 25 December 2022, “Rifting and Rotated Bergs 2” is from Planet on 28 December 2022, and “Sea ice in embayment” is from Landsat 9 on 7 September 2023.

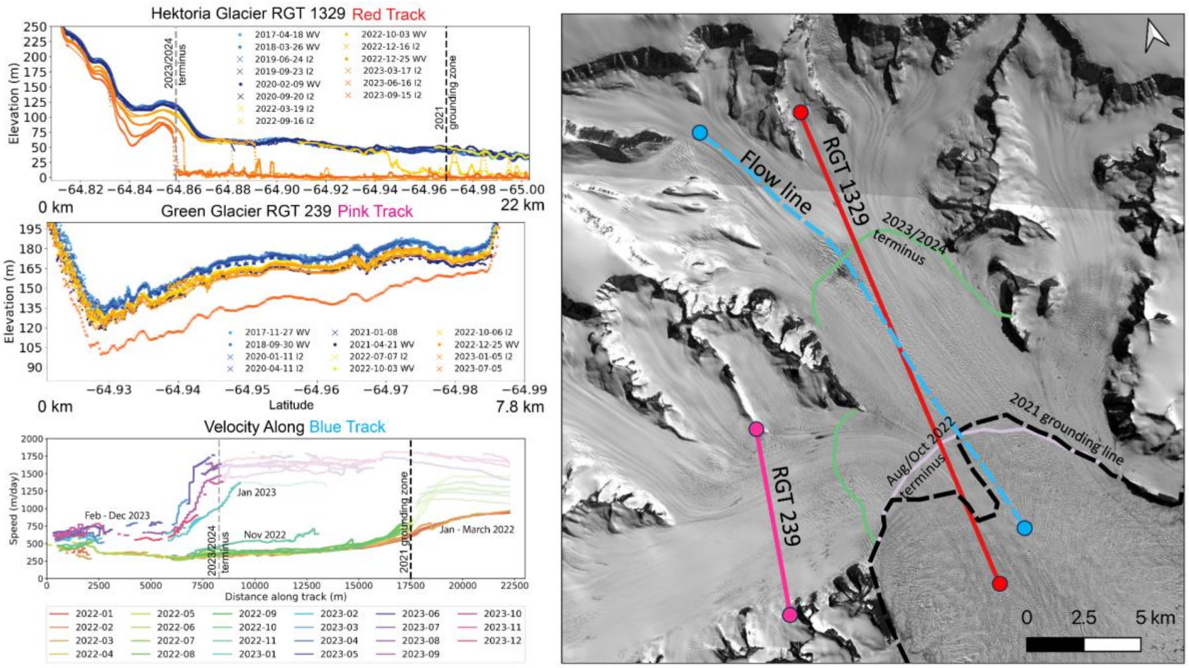

Figure 3.3: Time series of elevation and velocity changes of Hektoria and Green Glacier. A) Elevation profile of Hektoria Glacier (red track; Reference Ground Track (RGT) 1329) extracted from ICESat-2 data and Worldview DEMs from April 2017 to September 2023. B) Elevation profile across Green Glacier (pink track; RGT 239) from November 2017 to July 2023. C) Velocity along Hektoria Glacier's central flow line (blue track). The profiles are opaque at the transition from glacier ice to iceberg mélange at the time of the velocity measurement. Important time periods are indicated by text in the plot as well as the 2023/2024 terminus and the 2021 grounding line. Inset is 21 December 2021 Landsat 8 image with the ICESat-2 tracks and along flow track, the 2021 grounding line, August/October 2022 terminus, and the 2023/2024 terminus are depicted.

A quiescent period ensued during the Austral Winter 2022 while the sea ice and mélange remained in the immediate vicinity of the glaciers' termini (Fig. 3.2). During this time, the mélange likely provided enough backstress to prevent further calving (Cassotto et al., 2015; Robel, 2017). During the quiescent period Hektoria sped up by over 70% and began to dynamically thin (Fig. 3.3A and C); the same occurred on Green Glacier (Fig. 3.3B, Fig. A2-S5).

By October 2022, Hektoria Glacier's ice front had a staircase-like structure, with slumping and listric faulting, and ice cliff heights of 50 m (Fig. 3.2 "Staircase & slumping"; Fig.

A2-S4; Parizek et al., 2019; supplemental video in Crawford et al., 2021). Buoyancy-driven calving produces toppled icebergs that have a smoother, lighter surface that is often a dark blue, the iceberg has a scalloped surface shape suggesting the rift face is exposed (rather than upper surface) and they are generally smaller in size than tabular bergs (Fig. 3.1C; Sulak et al., 2017). From November through December 2022 the third phase of calving occurred, in which grounded ice calved at unprecedented rates for grounded ice of 0.8 km day^{-1} losing an additional 40 km^2 via buoyantly-driven iceberg calving (Fig. 3.1C; Fig. A2-S4) and retreated ~10 km measured along the central flow line. The size of these icebergs during this period indicates the glacier thickness was a minimum of 380-400 m (Fig. A2-S1). A notably rapid period of grounded ice retreat occurred from 25 December to 28 December where 2 km and ~4 km^2 of area was lost (Fig. 3.2). From January to March 2023 Hektoria retreated another 2 km. As of February 2024, Hektoria has remained at the same terminus location yet the dynamics have changed substantially as it continues to calve, accelerate, and thin (Fig. 3.3). The terminus no longer has a cliffed front and it continues to slump into a mélange that fills the HG embayment (A2-SV2).

Green Glacier underwent similar phases of retreat, yet only lost 4.5 km of grounded ice until Austral Winter 2023. Hektoria Glacier stayed relatively stable in Austral Spring 2023, however, Green Glacier has undergone several periods of minimal advancement and subsequent retreat of up to 2 km until April 2024 and is still actively calving and retreating.

The phases of retreat correspond to calving in different zones of the glacier. The initial phase was associated with the loss of the floating ice tongue. The quiescent phase saw a transition from floating to grounded ice. The last phase of rapid retreat was associated with calving from the lightly grounded ice plain region of the glacier. The grounding line is determined through various remote sensing and geophysical methods, as described below.

2.2 Grounding line constraints from elevation profiles

We utilize several datasets and observations to infer the grounding line location prior to the collapse of the HG floating ice tongue. We examine ICESat-2, DEMs, and optical imagery to determine the transition from floating to grounded ice.

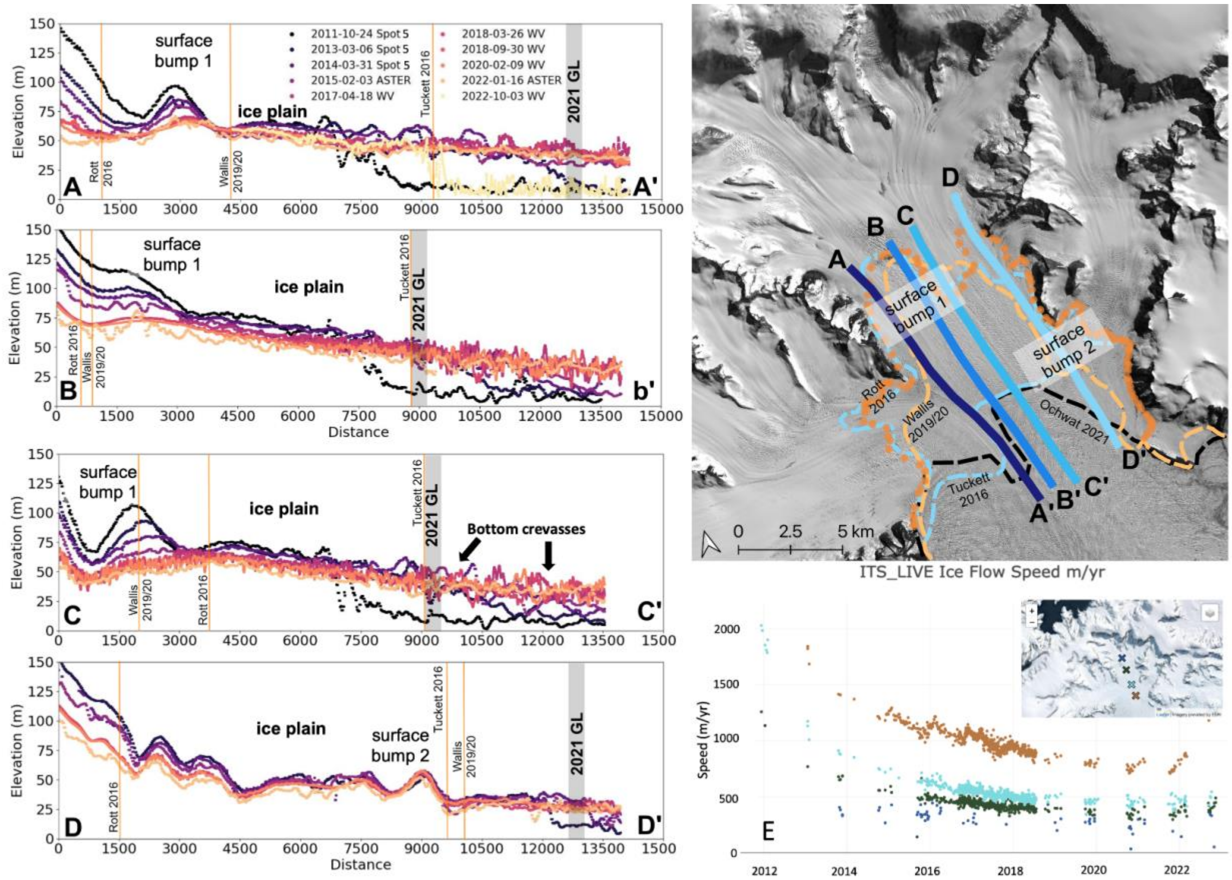

Figure 3.4: Time series of elevations along four profiles in the Hektoria-Green glacier system and corresponding velocities. Panels A-D) four elevation profiles show satellite stereo-image derived DEMs spanning 2011 to late 2022, with several surface features and interpreted state of the glacier ice labeled. Black arrows highlight the moving position of surface features interpreted as bottom crevasses on the basis of longer wavelength. Right inset: Landsat 8 image from 21 December 2021 showing elevation profile locations, recent published grounding line locations, the date of the data used to infer their location, including Ochwat 2021 (black dashed line; 1), Wallis 2019/20 (light orange dashed line; 50), Tuckett 2016 (blue dashed line; 41), and Rott 2016 (dark orange points; 49). and higher amplitude undulations (few hundred meters and tens of meters, respectively). Panel E shows the ITS_LIVE velocity from 2011-2022 at four points on Hektoria's central flow line.

Figure 3.4 displays a time series of ASTER, SPOT 5 and WV DEM derived elevation profiles along four flow-lines on Hektoria Glacier. The profiles show several fixed features that we interpret as dynamically supported topography, indicating that the glacier is grounded in those locations. Figure 3.4A and 3.4B show a “surface bump 1”, that thinned 2-3 m yr^{-1} from 2011-2022, yet it is not advected downstream. Velocities during this period and location are 300-400 m yr^{-1} (Fig. 3.4E, blue points), therefore, if this feature was floating it would have been advected downstream by at least 3 km. The “surface bump 1” is also evident in Figure 3.4C, however, it thinned substantially (5+ m yr^{-1}), suggesting that around 2018 this area may have lost considerable contact with the bedrock or at least reached a state of very low basal shear stress. Figure 3.4D shows several features, including “surface bump 2”, that do not move downstream either, suggesting this area of the glacier is fully grounded through the entire time-series.

Downstream of the proposed grounding line (Ochwat et al., 2024), long-wavelength undulations are present in all of the profiles and clearly show advection with the speed of the glacier (some data sets are noisy; however, the longer-scale surface features are still present; Figs. 3.3A and 3.4C). We interpret these as bottom crevasses, indicating a transition to fully floating hydrostatic equilibrium in those areas.

All profiles show two distinct breaks in the slope – after the surface bump 1 feature, which we identify as the upstream edge of the ice plain, as well as at the downstream end where the bottom crevasses appear. The two distinct breaks in the slope are a morphological indicator of an ice plain (Friedl et al., 2020; Tuckett et al., 2020).

2.3 Grounding line constraints from surface texture and calving style

We used optical images to examine the morphological transition from partially grounded to floating ice. In Figure 3.1B and Figure 3.4, we focus on spatial differences in the surface characteristics of the Hektoria-Green Glaciers. The lower glacier ice transitions from a smooth finely crevassed surface to a surface with longer-wavelength surface undulations or depressions representative of basal crevassing and therefore floating ice. This area of floating ice calved primarily as large tabular icebergs between early February and early March 2022. In April 2022, the calving style of the retreating ice front changed to buoyantly rotated icebergs (Fig. 3.1C). In some areas, these blocks were forwardly rotated (Fig. 3.1E), which is only possible in areas of high basal shear stress (i.e., grounded ice) or substantial amounts of melt undercutting (Alley et al., 2023). We rule out the latter due to the rapidity of the calving and the relatively cool ocean temperatures in this area (Nicholls et al., 2004). In addition, the staircase-like structures and slumping (Fig. A2-S4) that developed during retreat in the area above our inferred grounding line in Figure 3.1 are indicative of listric faulting (Parizek et al., 2019), super-buoyancy (Murray et al., 2015) or ice-cliff stresses under certain scenarios (Bassis et al., 2021, Crawford et al., 2021). All of these calving styles suggest the glacier was partially grounded in the ice plain region.

2.4 Glacier earthquakes

During key periods of Hektoria Glacier's retreat glacier earthquakes (GEQs) were detected in this region (Fig. 3.2, blue ticks, Supplemental Figs. A2-S6, A2-S7, and Table A2-S1). A comprehensive search for GEQs during the 2022-2023 time period revealed no events in the Hektoria region prior to November of 2022. Modeling the seismic waveforms of the observed events indicates the events were generated by a nearly horizontal source oriented roughly perpendicular to the Hektoria calving front that had peak forces of ~0.5-2 x 10^{10} N, consistent with generation by calved icebergs with mass of ~10^{11} kg (Fig. A2-S7; Sergeant et al., 2019, Olsen et al., 2021). Glacier earthquakes and their relationship to calving mechanisms have been well-studied in Greenland and minimally in Antarctica (Nettles and Ekström, 2010; Murray et al., 2015; Sergeant et al., 2019; Winberry et al., 2020). Buoyancy-driven calving can produce glacier earthquakes when icebergs capsize at the terminus of the glacier creating a force against the front and the solid earth; this momentarily creates a cm-scale speed reversal in the glacier and an upward force on the Earth (Nettles and Ekström et al., 2010; Murray et al., 2015; Sergeant et al., 2019). These types of earthquakes are characterized by long periods (30-150 s, moment-magnitude $M_w = 5$ tectonic earthquake) and are detectable globally (Sergeant et al., 2019). These types of glacier earthquakes can only occur at grounded or nearly grounded termini (Sergeant et al., 2019, see their Figure 1). Six GEQs occurred at Hektoria Glacier during the rapid retreat, three of which correspond solely to the retreat of Hektoria's front (Fig. A2-S7). The presence of these GEQs during Hektoria Glacier's retreat is further evidence that the glacier terminus was grounded during the rapid calving events.

2.5 Glacier response following the fast ice break-out

During the period of rapid retreat (2022-2023), Hektoria and Green glaciers rapidly thinned and accelerated. ICESat-2 and Worldview DEM data show that Hektoria and Green's thinning rate increased non-linearly in several phases, accelerating through time (Fig. 3.3). All thinning rates are the maximum rate measured at 64.845°S and 65.95°S, respectively, on the ICEsat-2 tracks in Figure 3A and B. Prior to the break-out, from 2017 through 2021, both Hektoria and Green Glacier thinned on average 3 m yr^{-1} (Fig. 3.3A and B). Immediately after the break-out, from March to December 2022 the thinning rate increased to 19 m yr^{-1} for Hektoria and 4 m yr^{-1} for Green. From December 2022 to March 2023 the rate for the remaining portion of Hektoria Glacier, in the catchment cirque, increased to 64 m yr^{-1} (Fig. 3.3A). By September 2023 Hektoria was thinning at rates of 80 m yr^{-1} and Green Glacier 54 m yr^{-1} (Hektoria measured at 64.841°S, as a trough had formed in the cirque creating the maximum thinning rate, Fig. 3.3A).

Similarly, Sentinel-1 derived velocities reveal a continuation of acceleration since the fast ice break-out. Ochwat et al. (2024) show a speed increase in Green Glacier of 500 m yr^{-1} to 1150 m yr^{-1} by January 2023, and here we show the speed has continued to increase to 1700 m yr^{-1} by December 2023 (Fig. A2-S5; measured at 7500 m), representing ~3.5-fold increase in speed since the loss of the fast ice. Hektoria Glacier accelerated from 400 to 900 m yr^{-1} by January 2023 and by December 2023 to 1700 m yr^{-1} near the terminus, a more than 4-fold increase (measured at 7500 m; Fig. 3.3C; Ochwat et al., 2024). In both Hektoria and Green Glacier, the acceleration is greatest near the terminus of the glacier and propagates upstream through the time series. At 8 km upstream of the current terminus of Hektoria Glacier, glacier flow speed has increased 70% (500 m yr^{-1} to 700 m yr^{-1}). At 11 km upstream of the Green Glacier terminus the glacier flow speed has yet to be affected by the loss of the fast ice and new calving regime.

3 Discussion

3.1 Grounding Line Controversy

As shown in Figure 3.1, several recent studies have presented grounding line maps for the Hektoria-Green glacier system that show substantial disagreements. The mappings are derived from different analyses: break in ice surface slope, derived from SAR-based TanDEM-X DEMs (Rott et al., 2020); Sentinel-1 SAR-based displacement variations and their correlation with tidal oscillations (Wallis et al., 2024); or surface morphological and elevation variations suggesting that the grounding line is downstream from the break-in-slope due to the presence of an ice plain (Tuckett et al., 2020; Ochwat et al., 2024). The first two studies place the grounding line farther upstream, at substantial breaks in slope (though not exactly at the same place; Fig. 3.1A) and the second study places the grounding line lower on the glacier by approximately 12 km (again, not in exactly the same location, but similar).

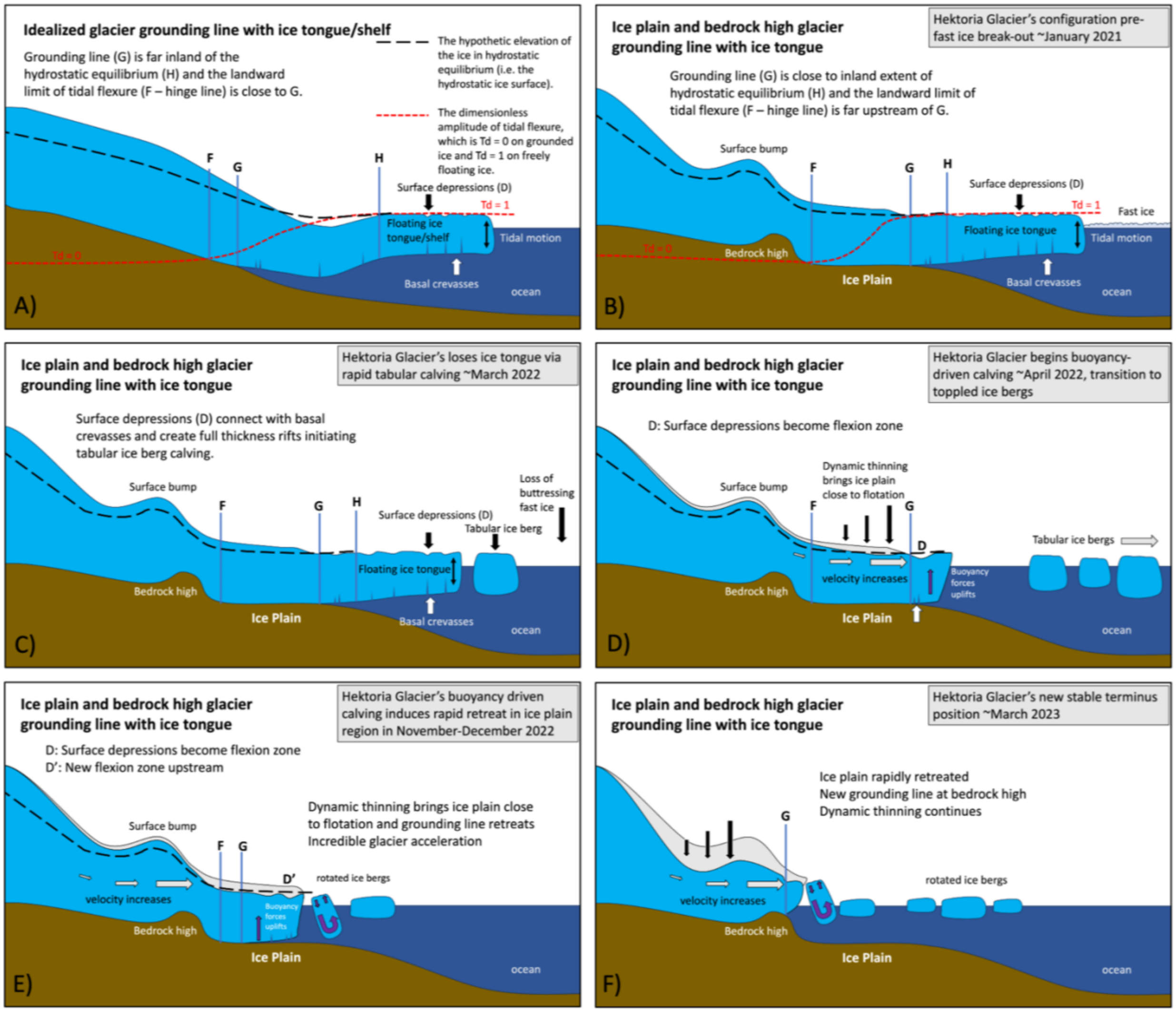

Figure 3.5 Time series schematic of an idealized glacier cross section and Hektoria Glacier's configuration and rapid retreat. Black dashed line is the elevation of an ice surface with the ice in hydrostatic equilibrium, the red dashed line is a dimensionless amplitude of tidal flexure where Td = 0 on grounded ice and Td = 1 for ice in full hydrostatic equilibrium. Point F is the landward limit of tidal flexure (hinge line); Point G is the grounding line, the last point at which the glacier touches the bedrock surface; Point H is the point of hydrostatic equilibrium of floating ice shelf or tongue. A) the idealized glacier and ice-shelf configuration; B) A conceptual model sketch of Hektoria Glacier's profile prior to the fast ice break-out, showing a bedrock high similar to that shown in Figure 3.3; C) Sketch of the Hektoria Glacier system as it loses its floating ice tongue, including surface depressions and basal crevasses creating full thickness rifts and tabular icebergs; D) Sketch of Hektoria Glacier as it begins to calve at its grounding line (April 2022); E) Sketch showing dynamic thinning of the lower glacier, with the ice plain nearing hydrostatic equilibrium and calving blocks buoyantly rotating, causing glacier earthquakes when capsizing against the terminus (November-December 2022); F) Hektoria Glacier retreats to a new more stable terminus position at the slope break or bedrock high (March 2023) and continues to calve, speed up, and dynamically thin.

An ice plain is a flat region of bedrock upstream of the grounding line, where the glacier ice has a very low slope (< 5°) and is near hydrostatic equilibrium (Fig. 3.5B; Brunt et al., 2011; Friedl et al., 2020). In an idealized glacier-ice-tongue/shelf scenario (Fig. 3.5A; see also Vaughan, 1994) the true grounding line (Point G: where the glacier first loses contact with the bedrock) is close in proximity to the landward limit of tidal flexure (Point F), and is far inland of the first point of hydrostatic equilibrium (Point H). In an ice plain geometry (Fig. 3.5B), point G is closer to point H (if ice thicknesses are similar in both cases) and point F is well inland of point G; there is also the coupling line (Point C), near point F, which is the upstream limit of the ice plain and is often confused with point G because it is the first break-in-slope. The two key differences between these geometries are: 1) the landward limit of tidal flexure extends far beyond the grounding line and high tidal variations can change the location of true landward limit of tidal flexure point F and may induce partial ungrounding of the glacier during high tides (Brunt et al., 2011); and 2) the ice plain area of the glacier is near hydrostatic equilibrium and is therefore sensitive to external perturbations (Brunt et al., 2011).

Tuckett et al. (2020) was the first to propose the presence of the ice plain at Hektoria Glacier. Tuckett et al. (2020) identify surface features that suggest grounded ice as well as two breaks-in-slope, one near the Rott et al. (2020) and Wallis et al. (2024) location, and one near our suggested position of the grounding line. The two breaks-in-slope can indicate an ice plain (Friedl et al., 2020).

We evaluated the Hektoria topographic features through 2011-2022 and concluded the larger features (10s of meters relief, few kilometers in lateral dimension) in the area between the two groups of grounding line locations do not advect downstream at the speed of the glacier, strongly suggesting that the glacier is grounded over much of the proposed ice plain area (Fig.

3.3). Satellite images of the 2022-2023 calving of the notional ice plain area showed a distinct change in style as retreat proceeded past the Tuckett-Ochwat grounding line estimates, switching from frequent tabular calvings to nearly entirely toppled icebergs. This coincided with structural evolution of the ice plain towards a staircase fracture style. This again indicates a substantial change in the basal shear stress. Additionally, IceBridge radar data from 2017 show a transition zone from grounded to floating ice in the area of the Tuckett-Ochwat grounding line (Figs. A2-S2 and A2-S3), IceBridge radar data in other years was inconclusive. Finally, we identified a series of glacial earthquakes that occurred in the region simultaneously as rapid retreat via buoyant calving consumed the proposed ice plain area, which points to a distinct change in glacier-bed conditions. We conclude that there was indeed an ice plain in the region between the two groups of grounding line estimates, which thinned near flotation after the fast ice break-out in 2022. This bedrock topographic setting of the lower Hektoria-Green glacier ice was the cause of the record-setting tidewater retreat rate of Hektoria's ice from November 2022 – December 2022.

The grounding line determined by Rott et al. (2020) was likely due to identifying Point C as the grounding line via the break-in-slope method. Friedl et al. (2020) and Brunt et al. (2011) noted that this was a common feature in ice plain areas that could lead to mis-mapping of the actual grounding line. The Wallis et al. (2024) grounding line was determined by identifying cyclical variations in the range distance (after subtracting displacement due to ice velocity) in Sentinel 1 SAR. However, the range variations can be interpreted in two ways: as vertical motion due to tides, or as cyclical tidally-paced variations in flow speed. Such variations have been noted in several low-slope ice streams and ice plain areas in previous studies (e.g. Ice Stream D/Bindschadler Ice Stream; Anandakrishnan et al., 2003 and Walker et al., 2012; Helheim

Glacier; Voytenko et al., 2015). Wallis et al. (2024) interprets range variations as vertical motion. We suggest that at lower tide ranges the terminus of the glacier is more grounded, causing a rise in basal shear stress that induces a slowdown. Therefore, the presence of a lightly-grounded, near-flotation ice plain can reconcile the various grounding lines.

3.2 Record pace of Hektoria Glacier retreat across the ice plain 2022-2023

Hektoria Glacier's rapid retreat is unprecedented in the modern glaciological record (Fig. 3.2). However, rapid retreats at nearly this rate have occurred before. Röhss Glacier on the James Ross Island from January 2001-December 2002 lost 9.1 km of grounded ice, 7.5 of it in the first year (Glasser et al., 2011), a similar albeit slower rapid retreat as seen at Hektoria Glacier. The Röhss Glacier retreat occurred six years after the loss of the Prince Gustav Ice Shelf and continued to retreat until 2009, losing 70% of its area and retreating a total of 15 km (Glasser et al., 2011). This is not unlike a previous retreat of Hektoria itself after the loss of the Larsen B ice shelf, in which the glacier retreated 500 m from 10 February to 26 February in 2011 at a rate of at least 35 m day^{-1} (Fluegel and Walker, 2024). The retreat rate in November to December 2022, 9 km of grounded ice in only two months, surpasses all the reported retreat rates in Alaska and Greenland, by an order of magnitude.

The dynamical thinning at Hektoria Glacier is also unprecedented. Previously, Hektoria Glacier was reported to have thinned ~38 m during six months 2002 after the loss of the Larsen B ice shelf (Scambos et al., 2004). During this same time period, Crane Glacier, south of Hektoria Glacier, thinned over 100 m in approximately two years, with about 40m of thinning due to subglacial lake drainage (Scambos et al., 2011, Shuman et al., 2011). Other record-breaking thinning rates have been reported to have occurred in Patagonia on the HPS12, a tidewater glacier which thinned at a maximum rate of 44 m yr^{-1} (Dussaillant et al., 2019).

Hektoria's thinning rate of 80 m yr^{-1} is heretofore unseen and coincides with 6-fold increase in velocity measured in the glacier cirque.

When the fast ice broke out, the terminus of the ice tongue lost a small amount of buttressing from the fast ice (Parsons et al., 2024), which mostly served to suppress the calving rate and allowed the tongue to advance between 2011 and 2022 (Robel, 2017). This loss instigated an increase in rifting and the rapid disaggregation of the ice tongue into tabular icebergs. Unlike the Larsen B Ice Shelf collapse in 2002, the optical imagery does not show substantial meltwater ponding that would have prompted rapid hydrofracture of the ice tongue rifts (Ochwat et al., 2024). The collapse of the HG ice tongue is similar to the disaggregation of Voyeykov Ice Shelf, Wilkes Land, Antarctica, which partially collapsed after the break-out of mélange and multiyear landfast sea ice in 2007 (Arthur et al., 2021, Teder et al., 2024). Yet, in this case, after the loss of the floating ice tongue, Hektoria and Green glaciers' calving style completely changed, and an unprecedented dynamically thinning and rapid tidewater retreat ensued.

3.3 Broader implications

Glacier instabilities, such as MICI and MISI, remain one of the greatest uncertainties in the future projection of sea level rise (Fox-Kemper et al., 2021). However, these instabilities may not always be the cause of rapid retreats. MICI ensues in various scenarios, dependent on cliff height (> 100 m), the ice thickness gradient upstream, the water depth, and the possibility of iceberg mélange providing enough backstress to support the ice cliff (Amundson et al., 2010; Bassis et al., 2021). Crawford et al. (2021) and Clerc et al. (2019) show the spectrum of possibilities of ice cliff failure and its relationship to the viscous-elastic flow response of the glacier, suggesting cliff height may thin due to the increase in ice influx speed, thus preventing MICI from occurring or stopping it prior to a runaway retreat. At Hektoria, the ice cliff heights rarely exceeded 60 m (Fig. 3.3A, Fig. A2-S4) suggesting MICI was not a driver in the rapid retreat.

At Hektoria Glacier, rapid grounding line retreat occurred, likely due to the presence of an ice plain. This instability may not be associated with MISI and is perhaps more representative of other grounding line instabilities (e.g. Sergienko, 2022; Batchelor et al., 2023). The ice plain grounding line retreat combined with buoyancy-driven calving ultimately resulted in the collapse of the glacier. With the buoyancy-driven glacier earthquake inducing mode of calving similar to Helheim Glacier discussed in Murray et al. (2015), yet with an instability due to the bed's ice plain geometry. Using oceanographic glacial landforms, Batchelor et al. (2023) infer a rapid buoyancy-driven retreat of Norwegian ice streams and ice shelves 15-19 kya during the last glacial maximum. They infer retreat rates of 55-610 m day^{-1}, similar to Hektoria Glacier's retreat rates in 2022 (Fig. 3.2). Ice plains have been detected in other areas of Antarctica such as the Bungenstockrücken region of the Filchner-Ronne Ice Shelf (Freer et al., 2023; Brunt et al., 2011), Pine Island Glacier (Corr et al., 2001), Amery Ice Shelf (Fricker et al., 2009), and Thwaites Glacier (Batchelor et al., 2023), which may be susceptible to rapid retreats. The loss of any of the supporting ice shelves may instigate rapid thinning, bringing the whole ice plain region to hydrostatic equilibrium and initiating the rapid buoyancy-driven retreat, as observed in this study. Therefore, it is imperative to obtain comprehensive bedrock data of the glaciers around Antarctica to better evaluate the potential for this type of instability to occur. Additionally, like Batchelor et al. (2023), we emphasize the need to incorporate nonlinear grounding-line behavior and subsequent rapid buoyancy-driven retreats in models predicting future sea level rise and the fate of the Antarctic glaciers.

4 Methods

4.1 Satellite image time-series for morphological evolution

We used MODIS (Moderate-Resolution Spectroradiometer), Landsat 8 and 9, Worldview (WV) -1, 2, and 3, Sentinel 2, and Synthetic Aperture Radar (SAR; Sentinel 1) to investigate changes in glacier extent, characteristics and dynamics. All these sensors were used to assess glacier surface and calving morphology, to infer crevassing and rifting styles, and to time the stages of retreat. The MODIS sensor, on the Aqua and Terra satellites, has a near-continuous daily image data archive from 2002 to present with coarse resolution (250-1000m). The Landsat 8 and 9 Operational Land Imager product has a panchromatic band with 15 m resolution and an orbital repeat time every 8-16 days. To assess smaller periods of rapid retreat, we used Sentinel 2 imagery acquired every 12 days (with 10 m resolution) and Planet data, acquired by numerous small multispectral imaging satellites (1-5 m resolution). Additionally, we use WV-1, 2, and 3 satellite images that provide very high resolution (< 0.5 m) stereo-optical images.

4.2 Image-derived elevation and velocity changes

Satellite optical imagery was used for investigating the morphology and freeboard of icebergs and the creation of digital elevation models (DEMs) of the glacier surfaces. To evaluate elevation changes of surface features on Hektoria Glacier through the 2011-2022 period we utilized DEMs derived from ASTER (AST_L1A) data and SPOT5 HRS (1A) stereo-imagery. The DEM processing follows Bernat et al., (2023). All the DEMs are co-registered and vertically adjusted to the 25 November 2006 SPOT5 DEM. This SPOT5 reference DEM is referred to the EGM96 geoid and was vertically coregistered to the earlier laser altimeter satellite, ICESat, which operated from 2003 to 2009. The ASTER and other SPOT5 DEMs are vertically adjusted using low-elevation-change regions, such as bedrock outcrops. A single constant vertical offset is applied to each DEM. This results in a vertical uncertainty of about 5 m for ASTER DEMs and about 2 m for SPOT5 DEMs (Berthier et al., 2012).

WV-1, 2, and 3 in-track stereo-image DEMs were obtained from the Polar Geospatial Center (PGC; https://www.pgc.umn.edu/) to evaluate elevation changes post fast ice break-out. The DEMs have a spatial resolution of 2 m and absolute accuracy of ~±4 m in horizontal and vertical dimensions (from PGC documentation; https://www.pgc.umn.edu/guides/stereo-derived-elevation-models/pgc-dem-products-arcticdem-rema-and-earthdem/). We applied a geoid correction using EGM 2008 and then assessed the mean elevation difference (i.e., bias) for six bedrock regions in each of the WV DEMs relative to the Reference Elevation Map of Antarctica DEM (REMA; Howat et al., 2019) and applied the mean offset to the WV DEMs, as done in Ochwat et al. (2024). Additionally, we used these to assess iceberg thickness and infer minimum bed depths (Fig. A2-S1). The commonly known BedMachine (Morlighem et al., 2020) and Huss and Farinotti (2014) bed map have dramatically different bed estimates for this area of the AP and are inconsistent with the ice thicknesses we derived from iceberg freeboard and geometry.

4.3 Ice flow speeds

To determine ice flow speeds through time we used standard feature tracking methods between consecutive pairs of Sentinel 1A and B SAR satellite images. From 2015 to 2017, Sentinel 1A provided 12-day image pairs and from 2017 until late 2021 and the addition of Sentinel 1B provided 6-day image pairs. We used the standard Gamma software (https://www.gamma-rs.ch/software) to track coherent speckle and surface features between the image pairs. Surface structure must remain relatively constant in the pair interval, which is generally the case for the minimum repeat pairs (Luckman et al., 2007). We applied feature tracking to all image pairs of the 6 (when available) and 12-day repeat-pass period images for 2021-2023 and mosaiced all velocity maps into monthly averaged composites to give improved spatial consistency. Once the velocity mosaics were generated, we extracted ice speed profiles along the central flowline of Hektoria and Green Glacier. We also use ITS_LIVE velocity data to track the flow speed from 2011-2022 of four points along the central flow line of Hektoria Glacier using the Inter-mission Land Ice Velocity Experiment (ITS_LIVE) mapping tool, with the days between image pairs ranging from 30-120 (https://mappin.itsliveiceflow.science/; Gardner et al., 2019).

4.4 Laser Altimetry

To study changes in surface ice elevation, we combined the WV image-derived DEMs with altimetry data from the Ice, Cloud, and Land Elevation Satellite 2 (ICESat-2), launched in 2018. We used the ICESat-2 ATL06 version 5 product, which provides a linear surface approximation of 40 m long overlapping segments along each ground track (Smith et al., 2021) with a 91-day repeat cycle (clouds permitting). We correct for the geoid (EGM 2008) prior to estimating the initial thickness of the fast ice, glacier tongues, and elevation of the glaciers. We use the along-track ICESat-2 data to examine thickness changes from 2018 to 2023. We extracted the WV DEM elevation data from 2017 to 2023 along the same track (RGT 1329 and 239) to fill in temporal gaps of the ICESat-2 data.

4.5 Airborne radar profiles

Unfortunately, despite several attempts to map the base of the ice in the glacier fjords and ice tongue areas of the Larsen B embayment, a careful examination of the available IceBridge CReSIS radar data provides only very limited and subjective indications of the ice base in the central Hektoria Glacier outflow. From 2009 to 2018 IceBridge collected radar data in the HG region, however, most of the radar data near the Hektoria glacier grounding zone have no reliable information on the bed signal and, hence, cannot be used for the glacier thickness and bed signal analysis. Nevertheless, the radar profile from 2017 shows a small area of the region with distinct reflections near the grounding zone. Here we followed the method in Antropova et al. (2024) to assess the Normalized Bed Reflection Power (NBRP) and the Normalized Internal

Reflection Power (NIRP) for the 2017 track 005. NBRP and NIRP indicate the power of the microwave signal reflected from the bed of the glacier and within the ice column, respectively. NIRP serves as a qualitative assessment of the signal power losses. Hence, in general, we consider the NBRP signal reliable if it is higher than NIRP. Relatively high values of NBRP coefficients suggest the existence of water underlying the ice (i.e., floating ice), while low NBRP values indicate rocks and/or sediments under the ice layer (Gades et al., 2000, Copland and Sharp, 2001). We used the NBRP and NIRP to identify a transition zone between grounded and floating ice, limited by the available data (Fig. A2-S2 and A2-S3).

4.6 Glacial-Earthquake Event-Detection, Location, and Waveform Modeling.

Glacier earthquake (GEQ) detections were made using a grid search method that is broadly similar to previous studies. We first downloaded and bandpass filter (40-20s) the vertical component seismic data in the West Antarctic and Antarctic Peninsula region. We then computed envelopes using a 60 s short-term average to 1000 s long-term average (STA/LTA) ratio for each station. We selected time-windows with potential GEQs by finding 500 s time windows during which at least 3 stations have a peak STA/LTA ratio that exceeds 2.5. Next, we generated potential event sources on a 100 km grid that spanned the Antarctic continent. For each potential source, we shifted the envelopes to account for the expected travel time difference between the grid point and each station. The coherence of the shifted envelopes was then used as a measure of event location likelihood at the grid point. Since we were focused on finding potential glacial events in the Antarctic Peninsula region, we removed events with optimum locations outside the study region, defined by a bounding box that spanned -3000 to -1500 km (Polar Stereographic X) and from 500 to 2000 km (Polar Stereographic Y). For 2022, this resulted in approximately 40 event detections. Most of these events are tectonic earthquakes originating from the Southern Ocean that were incorrectly located due to the relatively small aperture of our network. We culled these events via visual inspection as the dispersive nature makes them very easy to distinguish from GEQs. We used GEQs to associate the calving with the bed condition of Hektoria Glacier.

To constrain event size and azimuth, we model the GEQs as a centroid single force (CSF) (Nettles and Ekström, 2010, Walter et al., 2012). We download Green's functions from EarthScope Consortium's Syngine (Krischer et al., 2017). Due to the relatively low signal-to-noise ratios on the horizontal components of the seismograms, we were not able to estimate the dip of the source and prescribe it to be horizontal. We performed a simple grid search to obtain the optimal force and azimuth of the CSF that best reproduced the observed seismograms. As noted in previous work, there is a 180° ambiguity in the estimated azimuth that arises from the potential misalignment of the waveforms (Copland and Sharp, 2001).

Acknowledgements

We would like to thank NASA for funding our research and our fieldwork in 2024. We thank CIRES for continued support, particularly CIRES travel and Dawn Williams. We thank the Instituto Antártico Argentino for supporting our fieldwork to the Antarctic Peninsula and the helicopter pilots who flew us over Hektoria Glacier. We thank the many conversations with Doug Benn, Anna Crawford, Tasha Snow, Catherine Walker, Ben Wallis, Sierra Melton, and countless others. EB and BM acknowledge support from the French Space Agency (CNES).

Author contributions

Conceptualization: NEO, TAS, RSA; Methodology: NEO, TAS, AL, EB, MB, JPW, YKA; Data Curation: NEO, AL, EB, MB, JPW, YKA; Investigation: NEO; Visualization: NEO, YKA; Supervision: TAS, RSA; Writing—original draft: NEO; Writing—review & editing: NEO, TAS, RSA, AL, EB, MB, JPW, MB, YKA

CHAPTER 4

Wavering Ways Waves Work: Applying models and satellite and field observations to glacier surface waves

This chapter is in prep and will be submitted to a journal in early 2025.

Coauthors: Naomi Ochwat, Yoram Terleth, Robert S. Anderson, Alison Banwell, Martin Truffer, and Ted Scambos

1 Introduction

Ogives are among the most striking and least studied glacier surface features. They consist of two types of features, both arcuate shaped pointing downglacier. The name “ogives” originates from the Middle English “oggif” and Middle French “augive”, both relating to arches. The first type of ogive is referred to as “Forbes bands” or “band ogives” (hereafter called Forbes bands), which are alternating bands of light and dark surface color of the glacier. The second type of ogive are “wave ogives”, which are glacier surface undulations in crest-trough topography, like waves. Both features form at the bottom of icefalls, occur annually with the wavelength corresponding to the annual glacier displacement. They may occur on the same glacier, or independently. They are found in glaciated regions with icefalls all over the world.

Theories of ogive formation processes were debated during the nascence of glaciology (e.g. Forbes 1845; Streiff-Becker 1952; Nye 1958; Nye 1959). For Forbes bands, King and Lewis (1961) proposed that seasonal differences related to snowfall and melt within the icefall changed the mass and density of the ice, relative to the season, causing the ice to alternate between light and dark colors downstream of the icefall once the “chaotic surface layers” were melted away. Fisher (1962) took this theory one step further and measured apparent density differences in the light and dark bands and attributed them to seasonal temperature differences within the icefall. Later studies, Vincent et al. (2018) and Goodsell et al. (2002), proposed different mechanisms for the formation of Forbes bands, but concluded that the bands form from different ice types, although the origin of each ice type remained to be determined.

Compared to Forbes bands, much less is known about the formation processes of wave ogives, which is the focus of this study. Early studies acknowledged the presence of wave ogives and attributed their origin to surface ablation differences associated with the Forbes bands. For example, Atherton (1963) was one of the first to specifically investigate wave ogive formation and proposed that velocity fluctuations ultimately produced the features. However, there were competing hypotheses from Nye (1957) who suggested the seasonal ablation pattern in icefalls gave rise (pun intended) to wave ogives. In 1986, Waddington synthesized the existing literature into two main hypotheses of ogive formation. He proposed that ogives may be formed from both seasonal mass balance differences, as well as seasonal velocity changes (Waddington, 1986). The mass balance mechanism suggests that during summer, icefall ice experiences greater ablation rates compared to winter, resulting in a smaller volume of ice entering the lower glacier in the summer, creating the trough of the ogive. In winter, when accumulation is more sustained and ablation is lower, a larger volume of ice enters the lower glacier, giving rise to the crest of the ogive (Nye 1958; Waddington 1986). Conversely, the velocity variation hypothesis poses that the substantial difference between the velocity of the icefall (that has a near constant seasonal velocity) and lower glacier, paired with a seasonal variation in velocity of the lower glacier, results in “stretching” of the ice in summer and “pile-up” of ice in winter, creating the large ogives (Waddington, 1986). Despite some acceptance of the velocity-origin theory (Goodsell et al., 2002), the formation process of wave ogives has not been fully agreed upon or explored since 1986.

Our study focuses on geophysical observations and modeling of wave ogives, hereafter simply referred to as “ogives.” We seek to better understand the formation process for ogives, using data from the well-developed ogive train present on Gilkey Glacier, below the Vaughan Lewis Icefall in the Juneau Icefield region of Alaska. Our research combines a variety of in-situ Global Navigation Satellite System (GNSS) and satellite-derived velocity observations, combined with timelapse camera data, in order to constrain parameter values in a finite-difference numerical model that simulates ogive formation. We then use this model to test the plausibility of the two formation mechanisms described above; i) seasonal mass balance variation; and ii) and seasonal velocity variation.

2 Study Area

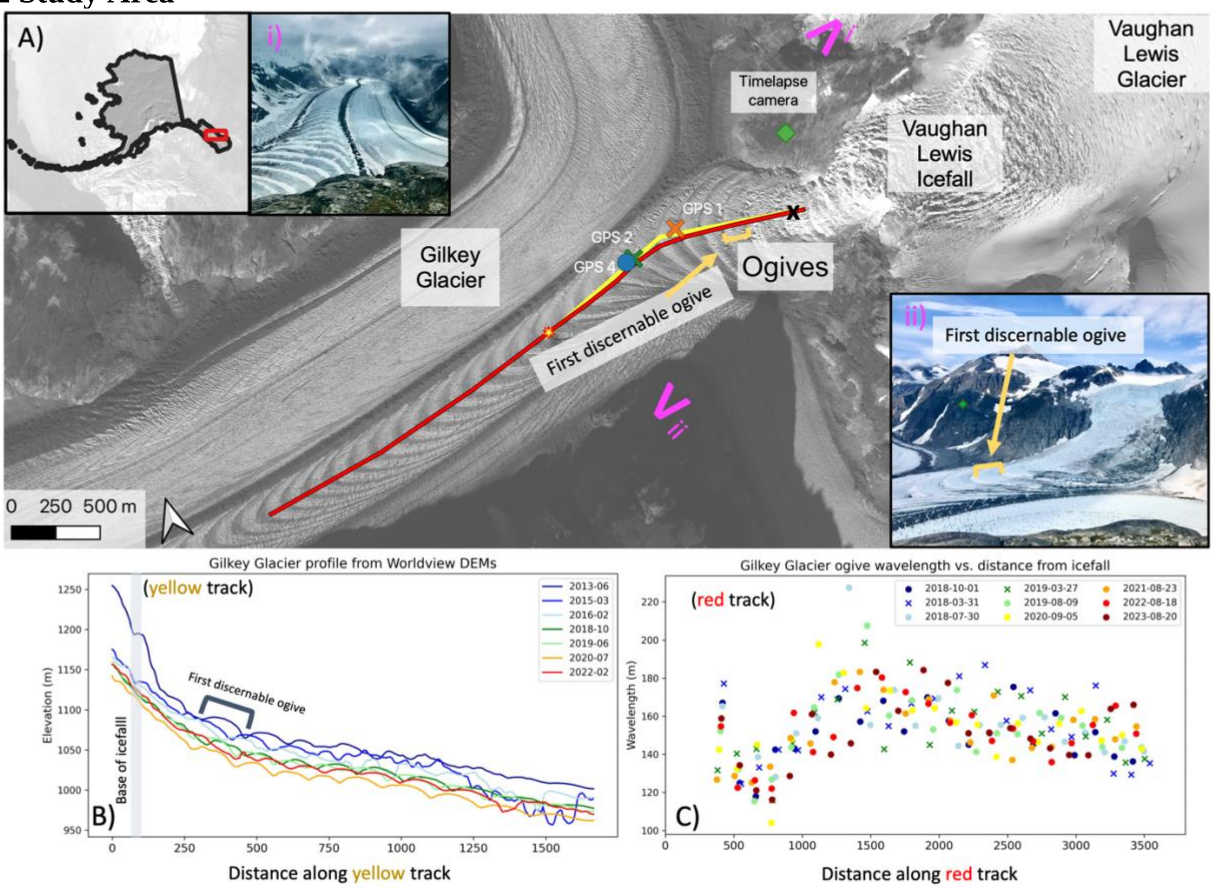

Figure 4.1: Gilkey and Vaughan Lewis glaciers, the Vaughan Lewis icefall, and Gilkey Glacier ogives in the Juneau Icefield, Alaska. Image from Worldview-1 from 1 October 2018. Insets i and

ii show photographs of the study area from their respective i and ii locations on the map (pink "V" showing view angle). Location of the timelapse camera is depicted as green diamond in the map and inset ii. First discernible ogive is denoted by the yellow bracket and labeled in map, inset ii, and panel B. The black X is the "base of the icefall." Three GNSS stations collected data, named GPS 1, 2 and 3; two on crests (orange and green X), and one in a trough (green dot) of the ogives near the base of the Vaughan Lewis Icefall; A) Map of Alaska, indicating the location of the Juneau Icefield. B) Elevation profile of the Gilkey Glacier (yellow track in panel A, with the red star indicating the end of the yellow track) through time, taken from Worldview-derived DEMs. Base of icefall and first discernable ogive labelled. C) Wavelength of ogives from the base of the icefall (red track in panel A). The exact locations of the yellow and red tracks in panel A differ slightly as a result of the red line following the glacier's central flowline, whereas the yellow line connects the GNSS points, which we required for future analysis. See Fig. 4.2 for the thickness profile along the yellow track.

The Juneau Icefield in southeast Alaska is a plateau icefield with ~1000 glaciers feeding into Canada and the Pacific ocean (Davies et al., 2022). Juneau's plateau icefield geometry has a large flat area in the accumulation zone with steep icefalls draining the plateau, which feed large valley glaciers (here referred to as "lower glacier"). The Juneau Icefield has 55 icefalls, with 22 glaciers reported as having ogives (Davies et al. 2022), including the Gilkey Glacier (Fig. 4.1). The Gilkey Glacier has an area of ~220 km^2 (GLIMS database; Raup et al., 2007) with several tributary glaciers and numerous icefalls that feed the large valley trunk. The Vaughan Lewis Glacier flows from the plateau at ~1800 m elevation through the Vaughan Lewis Icefall and into the Gilkey Glacier (~1030 m elevation), where at the bottom of the icefall, ogives form and advect downglacier. The ogives here represent the quintessential feature with large amplitudes and crescent shape. We chose the Gilkey Glacier to study ogive formation due to the presence of the classical ogives, the well documented history of the Juneau Icefield, and the ability to collect field data with ease via support from the Juneau Icefield Research Program (JIRP).

3 Methods

We used several different remote sensing datasets to gain an understanding of ogive characteristics and constrain parameter values for the finite difference numerical model. Field data was collected on the Gilkey Glacier in Summer 2023 and Summer 2024.

3.1 Satellite remote sensing

To establish an ice velocity time series for the Gilkey Glacier and assess mean seasonal and annual ice velocity variations, we used the Inter-mission Land Ice Velocity Experiment (ITS_LIVE) velocity dataset (Lei et al., 2021; Gardner et al., 2019). ITS_LIVE utilizes a variety of satellite sensors (e.g. Landsat, Sentinel -1, -2), including optical and synthetic aperture radar (SAR) data, to track the velocity of glaciers around the globe at sub-seasonal, seasonal, and annual timescales. Feature tracking software operates by finding similar features in images (backscatter intensity for SAR data), matching the same feature in the later image, and dividing the distance between the features by the time between the two images to calculate a velocity (Gardner et al., 2019). We used the ITS_LIVE Browse Tool to track the flow velocity of the Vaughan Lewis glacier and Gilkey Glacier from 2018 to 2023, using all available image pairs with 30 to 90 days separation, in order to capture the seasonal and sub-seasonal signals.

To evaluate the glacier geometry, and more specifically changes in ogive characteristics, through time, we utilized the ArcticDEM strips from the Polar Geospatial Center (PGC; Porter et al., 2022). The ArcticDEM is a high resolution (2 m in the horizontal) digital elevation model (DEM) that is mosaiced from many smaller high resolution DEM images, called "strips". The ArcticDEM strips are created from high resolution (<0.5 m) Worldview satellite imagery and are time-dependent. Not all strips were used because winter imagery made differentiating the ogives difficult due to the presence of snow. To document the wavelength of the ogives, we used optical imagery from several sensors, including Landsat 8 and 9's panchromatic bands (15 m resolution) and Worldview-1, -2, and -3 (<0.5 - 2 m resolution). We also used these images to measure the width of the icefall chute, Gilkey Glacier, and estimate the transition length of the velocity gradient used for the model.

3.2 Field data collection
3.2.1 Timelapse camera deployment

On 16 July 2023, we installed a timelapse camera on the nunatak above the Gilkey Glacier that separates the Vaughan Lewis Icefall from the now disconnected Little Vaughan Lewis (Fig. 4.1, green diamond). We programmed a Harbortronics assisted Canon SLR camera to take a photo every 30 minutes while the battery remained powered via a small solar panel mounted to a tripod. In July 2024 we retrieved the images from the camera. As described below, these images were used to quantify icefall velocity and test the assumption of a steady icefall velocity throughout the year.

From a total of 17,456 timelapse camera images collected between July 2023 and July 2024, we manually selected 472 images that had sufficient light and visibility for feature tracking, while compromising to retain relatively small time (<4 days) increments between image pairs. We used the openly available ImGRAFT package (Messerli and Grinsted, 2015) to correct our camera model to the 2 m ArcticDEM strip from the Worldview image, acquired on 30 July 2020, through manual definition of 8 ground control points. ImGRAFT computes displacement between subsequent image pairs for a series of grid points on the glacier. We removed the calculated displacements between each image pair that do not meet a minimum correlation threshold of 0.7, and removed displacements whose direction of motion was not consistent with the downslope direction in the icefall. ImGRAFT then computed flow velocity in the direction of ice flow for each point and for each image pair. We removed outliers (+/- 2 standard deviations) and took the spatial mean of these velocities as our ice velocity for the time interval between the two images, further defining the range of uncertainty as +/- 2 standard deviations.

3.2.2. GNSS deployment

We used two sets of in-situ GNSS data collected a year apart and from different GNSS systems. We describe the two methods below.

In July 2023, we installed four GNSS units on the Gilkey Glacier near the base of the Vaughan Lewis Icefall. We deployed the units on the troughs and crests of two ogives; the first pair on the fourth ogive downstream of the icefall and the second pair on the sixth ogive, ~500 m and 800 m away from the base of the icefall, respectively (Fig. 4.1). For safety reasons, we could not deploy the GNSS any closer to the icefall. However, the GNSS unit in the trough of the fourth ogive malfunctioned and did not collect data. For the three units that successfully functioned, we collected 2 GNSS positional points every 5 minutes for 2-3 days depending on battery life. We then converted the raw data files into RINEX files and submitted them to the Canadian Geodetic Survey Precise Point Positioning program as ITRF Kinematic processing (https://webapp.csrs-scrs.nrcan-rncan.gc.ca/geod/tools-outils/ppp.php). This produced solutions for the data from which we were then able to calculate the horizontal velocity. First, we calculated the distance from the initial location for each point in time for all stations, then we cleaned the data by visually inspecting outliers and removing them as required (Banwell et al., 2024). In general, we removed individual values and clusters of values that jumped distances greater than 20% than the previous hundreds of data points (we still show these outlier values as opaque colors in our data plots). We plotted the original and clean data and fit a line of best fit (i.e., linear regression) through the clean data; the slope constrains the mean velocity over the timeseries.

In July 2024, we deployed an additional 18 GNSS units (Emlid Reach RS2) on the Vaughan Lewis Glacier above the Vaughan Lewis Icefall (Fig. 4.2) over a period of five days. After downloading the data, we converted the raw data from latitude and longitude to UTM 8N, and calculated the velocity by finding the distance between day 1 and day 6 and dividing by time. We used the GNSS and timelapse imagery derived velocity data to gain a greater understanding of ice flow through the entire system and estimate the initial velocity conditions and the variation to be used in the model.

3.2.2 Ice Thickness Calculations

Using the velocity data and Worldview-derived DEMs, we calculated ice thickness using two methods; 1) a equation for the slope-dependent basal shear stress, and 2) Glen's Flow Law that is dependent on observed surface velocities. For both methods, we used values for the slope and velocity estimated at 400 m downglacier of the base of the icefall, which is the location of the crest of the first completely discernable ogive (Figs. 4.1 and 4.4).

For the first method to calculate ice thickness, we used the equation for basal shear stress that is dependent on the slope of the glacier (Cuffey and Paterson, 2014; their equation 8.6):

$$b = f'\rho g H S \tag{1}$$

Where b is 10^5 Pa, ρ is the density of ice (~900 kg m^{-3}), g is the acceleration due to gravity (9.8 m s^{-2}), H is the ice thickness in m, S is the slope (tangent of the angle), and f' is the valley geometry correction factor. We have assumed f' to be 1, and therefore ignore lateral drag of the valley walls, essentially assuming an infinitely wide glacier (Cuffey and Paterson, 2014).

For the second method, we used Glen's Flow Law to calculate ice thickness from the velocity data. Here, it is important to note that in this calculation we assumed that U_s (i.e. surface velocity) is caused solely through internal deformation and does not take into account basal sliding. This is in opposition to how U_s is defined in the analytical and numerical models (see below). We reconcile these differences by acknowledging a proportion of the glacier's movement is likely caused by basal sliding, which we account for by using the mean annual velocity and not the seasonal pulse. The seasonal pulse is most likely induced by an increase in basal sliding, whereas the annual mean may be more representative of the baseline internal deformation. We discuss this further in the Discussion section. To solve for *H* from the mean U_S, we invert the formula for the internal deformation generated surface velocity:

$$U_s = \frac{2A}{4}(\rho g S)^3 H^4 \tag{2}$$

The ice thickness (*H*) is therefore:

$$H = \left[\frac{U_s}{\frac{2A}{4}(\rho g S)^3}\right]^{1/4} \tag{3}$$

Where U_s is the surface velocity, *A* is the flow-law coefficient $2x10^{-16}$ Pa^{-n} yr^{-1} and assuming n = 3.

3.3 Modeling ogives

First we considered an analytical solution to simulate ogive formation prior to running the finite difference model. An analytical solution allowed us to better understand the physics behind the phenomena in order to simplify the complexities of glacier flow to be used in the numerical model.

3.3.1 Analytical model of ogive amplitude

In order to test the various hypotheses of ogive formation, we must first take into account the basic principles of mass continuity. Since an ogive train is essentially an alternating series of thicker and thinner areas of glacier ice, we use ice thickness calculations along a glacier profile through time to see if ogive-like structures are generated.

The expression we use to relate ice thickness, ice discharge, velocity, and mass balance, through time is:

$$\frac{dH}{dt} = -\frac{dQ}{dx} + b \tag{4}$$

Where *H* is ice thickness, *x* is distance downglacier, *t* is time, *Q* is ice discharge (m^2 yr^{-1}), and here *b* is the local meteorological mass balance (m yr^{-1}). If we assume that the dominant mechanism of Q, the ice discharge, is basal sliding (i.e. ignoring internal deformation), then we can approximate that $Q = U_s H$ in which H is the local ice thickness, and U_s is the sliding velocity. We assume U_s is the velocity throughout the vertical ice column, and hence also the (measurable) surface velocity. By ignoring internal deformation, this calculation becomes an endmember case, which we discuss further in more detail in the Discussion.

If we have a constant steady system, in which there are no changes throughout time for the mass balance or ice discharge, then we would expect the ice thickness and velocity to stay the same throughout time as well. However, if the mass balance or sliding velocity varies over the course of a year then that will be translated into a change in thickness. Ignoring the mass balance (b), we can assume that sliding velocity varies through a year from U_{so} to U_{smax} in a pulse that lasts a fraction of the year (T) and the spatial pattern is characterized by λ, then we can calculate how the ice thickness should change through that time following the integral:

$$dH = -\int_0^T \frac{dQ}{dx} \qquad (5)$$

From this, we would expect the ice to thin in the region of the glacier where acceleration occurs.

The spatial gradient in ice discharge may be scaled by:

$$\frac{dQ}{dx} \sim \frac{d(U_s H)}{dx} \sim \frac{H(U_{smax} - U_{so})}{\lambda} \qquad (6)$$

Here we have assumed that H does not vary dramatically within one year (the ogive is small in amplitude relative to the ice thickness). Combining these equations yields an estimate of how the ice should thin over the duration of the sliding pulse:

$$dH = -\frac{H(U_{smax} - U_{so})\,T}{\lambda} \qquad (7)$$

The negative sign in equation 7 ensures that in the stretching region, where $\frac{dQ}{dx}>0$, the ice will thin, generating a trough in the ogive train.

Now that we have described the analytical model that describes how ogive amplitude is related to ice thickness, given our assumption of ignoring internal deformation, we can use these physics to create a 1-D finite difference model.

3.3.2 Numerical Model

We created a one-dimensional domain with a prescribed initial thickness *(H(x))* and the distance from the base of the icefall defined as *x*. To test the role of seasonal mass balance variation, we forced a sinusoidal function through time, imposing a shift at an artificial ELA (~750 m) to test the possibility of the ablation mechanism of ogive formation (Fig. 4.3). The mass balance of the icefall is defined as $a_{icefall}$ and the valley glacier as a_{valley}. The transition from the icefall to the valley glacier occurs over the length scale λ. The mass balance through time is defined as:

$$a(x) = a_{valley} + \left(a_{icefall} - a_{valley}\right) \times \left(\frac{\pi}{2} - \operatorname{atan}\left(\frac{x - x_{icefall}}{\lambda}\right)\right) \qquad (8)$$

At each timestep the mass balance updates as:

$$a(x,t) = a(x) + amp_{mb}(b) \times sin\left(\frac{2t\pi}{P}\right) \qquad (9)$$

Where t is time, P is the period (one year), and the amplitude of seasonal mass balance variation is variation is amp_{mb}.

To test the role of velocity variation on ogive formation, we imposed a gaussian velocity field *(u(x, t))* that captured the velocity pulse described above (essentially, U_{smax}-U_{so} through time; Fig. 4.2C). In the *x* direction, *u(x)* is uniform ($u(x) = u_{icefall}$) until a location $x_{icefall}$ (1000 m), where we then forced a gradual decrease in velocity, occurring over the length scale λ, simulating the slowdown that occurs at the bottom of an icefall. The proportion of the width of the icefall to the valley glacier can help account for the change in the discharge due to ice thickness differences, therefore, we scale the velocity by the proportion of the width of the icefall ($w_{icefall}$) to the width of the valley glacier (w_{valley}). The gaussian pulse varies around u_{valley} with time of t and a period of one year (P) and with amplitude amp_u, the pulse is defined by the time period of sliding, t_{sig}, and the width of the peak as t_{slide}:

$$u(x) = u_{valley} + ((u_{icefall} - u_{valley}) \times \left(\frac{w_{icefall}}{w_{valley}}\right)) \times (\frac{\pi}{2} - atan\left(\frac{x - x_{icefall}}{\lambda}\right)) \quad (10)$$

$$u(x,t) = amp_u \times (\left(\frac{\pi}{2}\right) + atan\left(\frac{x - x_{icefall}}{\lambda}\right)) \times e^{-(\frac{t-t_{slide}}{t_{sig}})^2} \quad (11)$$

The imposed velocity variation and/or mass balance variation allows the ice thickness (H) to vary through time, theoretically creating ogives if the variations are sufficient to cause changes in thickness (Fig. 4.2). In equation 12, we calculate H through forward forward finite differences:

$$H(t,x) = H(t-1,x) \times (a(t,x) - \left(\frac{dH(x) \times u(x,t)}{dx}\right)). \quad (12)$$

This allows us to plot the ice thickness changes through time and assess whether ogives do or do not form along the profile of the glacier for an idealized glacier. For the Gilkey Glacier, we use the same numerical model to investigate the characteristics of ogives and limitations of the model. We use this model to generate ogives in an idealized glacier setting, using estimated parameters from literature on the Alaskan region. This allows us to draw generalized conclusions about ogive formation prior to using the model on a real glacier. This ensures us that the real glacier with ogives, the Gilkey Glacier, is not a special case. Then we input parameters estimated from data on the Gilkey Glacier.

4 Results

4.1 Gilkey Glacier characteristics from Worldview-derived DEMs, velocity data, and math!

4.1.1 Ogive setting and wavelength

The geometry of the Vaughan Lewis Glacier, icefall, and Gilkey Glacier were evaluated using the optical satellite imagery and ArcticDEM strips. The Vaughan Lewis Icefall drops almost 500 m in less than a kilometer of distance through a narrow (~400 m) chute, resulting in a slope greater than 40° through the icefall. The icefall feeds into the trunk of the lower Gilkey Glacier along with two other tributaries at the same juncture. At the base of the icefall, wave ogives are fully developed, which are up to ~750 m wide within a few hundred meters downglacier (Fig. 4.1).

Figures 4.1B and C show characteristics of the ogives that are observed between the base of the Vaughan Lewis Icefall to 3000 m downglacier. Figure 4.1B shows the troughs and crests of the ogives, which beginning with the first discernable ogive, are 5 to 8 m in amplitude, equivalent to heights from crests to troughs of 10 to 16 m (Fig. 4.1). The ogive widths vary over space, beginning as 700-750 m wide and downglacier narrowing to 400 m wide. Also, the first ogive at the bottom of the icefall has variable widths from year to year, likely due to discrepancies in the location of the crest of the first ogive, it is difficult to distinguish within the icefall (see map in Fig. 4.1 and inset ii). In the first 500 m horizontally downglacier from the icefall, the ogives have wavelengths of ~130 m, which is approximately the same as the annual mean velocity in this region of the glacier (Fig. 4.3). Between 500 and 1000 m horizontally downglacier from the icefall, the wavelength increases to ~175 m, then slowly decreases over to ~150 m at a distance of 3000 m downglacier from the base of the icefall.

4.1.2 Ice thickness

As explained in the Methods, we calculated ice thickness using two methods; 1) an equation for the slope-dependent basal shear stress (Equation 1), and 2) Glen's Flow Law that is dependent on observed surface velocities (Equation 3). We calculated the slope using the DEMs as 0.05 for the lower Gilkey Glacier. We input this value into Equation 1, which yielded an estimated ice thickness of ~227 m at the point 400 m from the base of the icefall. We chose 400 m from the base of the icefall because that is the crest of the first discernable ogive (Fig. 4.1A). We use the mean annual velocity derived from the Gilkey Glacier data points of the ITS_LIVE dataset (Fig. 4.3B, yellow and pink lines). We plug 133 m yr^{-1} in Equation 3 to calculate the ice thickness based on Glen's Flow Law, which resulted in an ice thickness of ~350 m (Fig. 4.2).

In Figure 4.4, we show the two point calculations for ice thickness described above, along with ice thickness profiles from the base of the icefall to 1.5 km downstream taken from Millan et al. (2022) and Farinotti et al. (2019)'s estimations. Both Millan et al., (2022) and Farinotti et al. (2019)'s methods used Glen's Flow Law based inversion models to calculate the ice thickness, similar to our Equation 3. At 400 m from the base of the icefall (Fig. 4.2, red X in photo), Millan et al. (2022) reports a thickness of ~380 m and Farinotti et al. (2019) ~340 m, compared to our calculations of 227 and 350 m (purple and yellow dots, respectively). If we omit our slope-based calculation (Equation 1; 227 m, purple dot), then all thickness estimates based on Glen's Flow Law are in relative agreement, suggesting the ice is between 340-380 m thick at 400 m from the base of the icefall. The ice thickness estimates from Millan et al. (2022) and Farinotti et al. (2019) increase downglacier until roughly 900 m horizontally from the base of the icefall, where the ice thickness plateaus at ~475 m (Fig. 4.2).

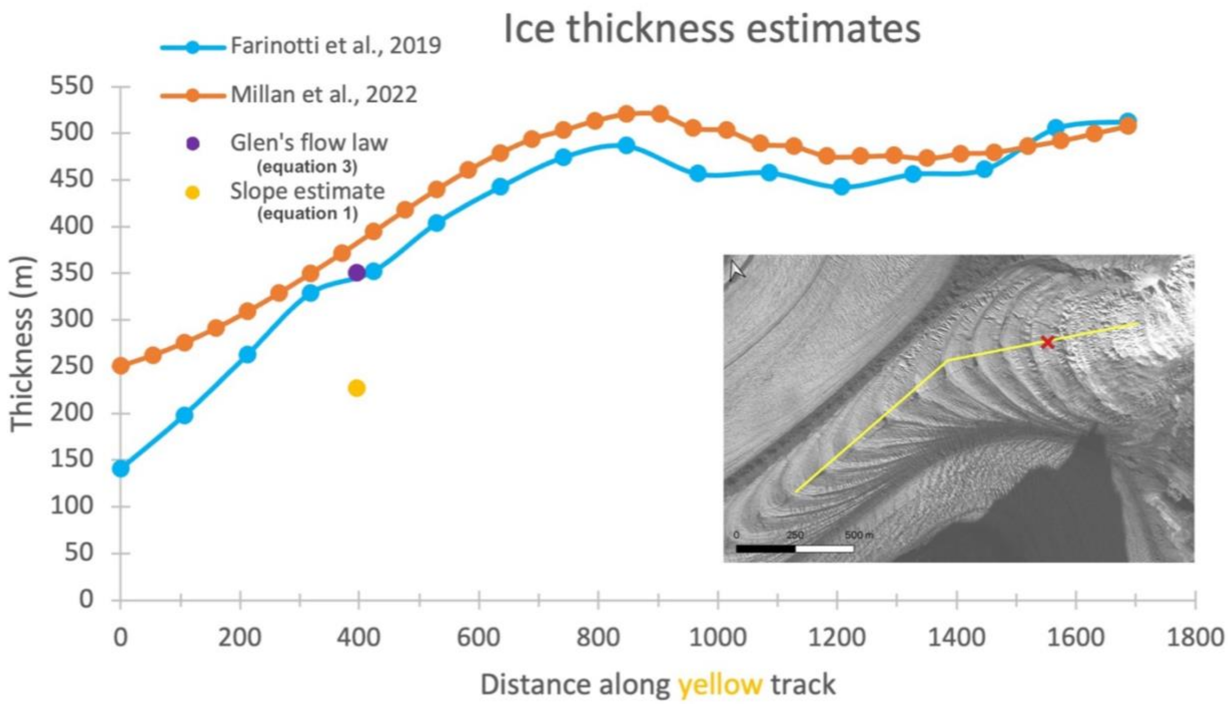

Figure 4.2: Ice thickness of the Gilkey Glacier from four different sources. The blue line is the ice thickness from Farinotti et al. (2019), the orange line is the ice thickness from Millan et al., 2022, the purple dot is the calculated ice thickness from Glen's Flow Law (our equation 3), and the yellow dot is the calculated ce thickness from basal shear stress and slope (our equation 1). The red X in the image inset is where we calculated our estimates in order to compare with the literature, as discussed in Section "Ogive wavelength".

4.1.2 Ice velocity observations

To determine input parameter values for the numerical model to simulate the Gilkey Glacier and to describe the general characteristics of the glaciers in our study area, we utilized several satellite and in-situ velocity datasets shown in Figure 4.3. The satellite-derived ITS_LIVE velocities (Fig. 4.3A) are from two points in the Vaughan Lewis Glacier and two points in the Gilkey Glacier from 2018 through 2022. We find that in the lower glacier, the seasonal velocity varies between the mean annual maximum of 250 m yr^{-1} and mean annual minimum of ~60 m yr^{-1}, with a mean annual velocity of ~130 m yr^{-1} (Fig. 4.3A). We also find that the annual peak in velocity usually occurs in late April/early May and is usually lowest in July, though we note that the data are sparse from September to March, likely due to winter darkness inhibiting feature tracking. Our 2024 GNSS data show that the Vaughan Lewis Glacier ice that feeds the Vaughan Lewis Icefall accelerates near the icefall, increasing from 60 to 90 m yr^{-1} (Fig. 4.3B). Our timelapse imagery derived velocities show that as the ice flows through the steep icefall (> 40°), it accelerates to 1800-2500 m yr^{-1}, with a mean annual velocity of ~2200 m yr^{-1} (Fig. 4.4). We note that there are no data from December 2023 to February 2024, but the absence of any significant variation in the months around the data gap suggests there was not a substantial change during that period. The ice decelerates as it enters the Gilkey, with a mean summer velocity of 114 m yr^{-1} determined from our 2023 GNSS data (Fig. 4.3D and B, Table 4.1). This annual mean velocity is reflected in the initial ogive spacing at the base of the icefall, where one year of ice flow is represented by one complete ogive (Fig. 4.1C).

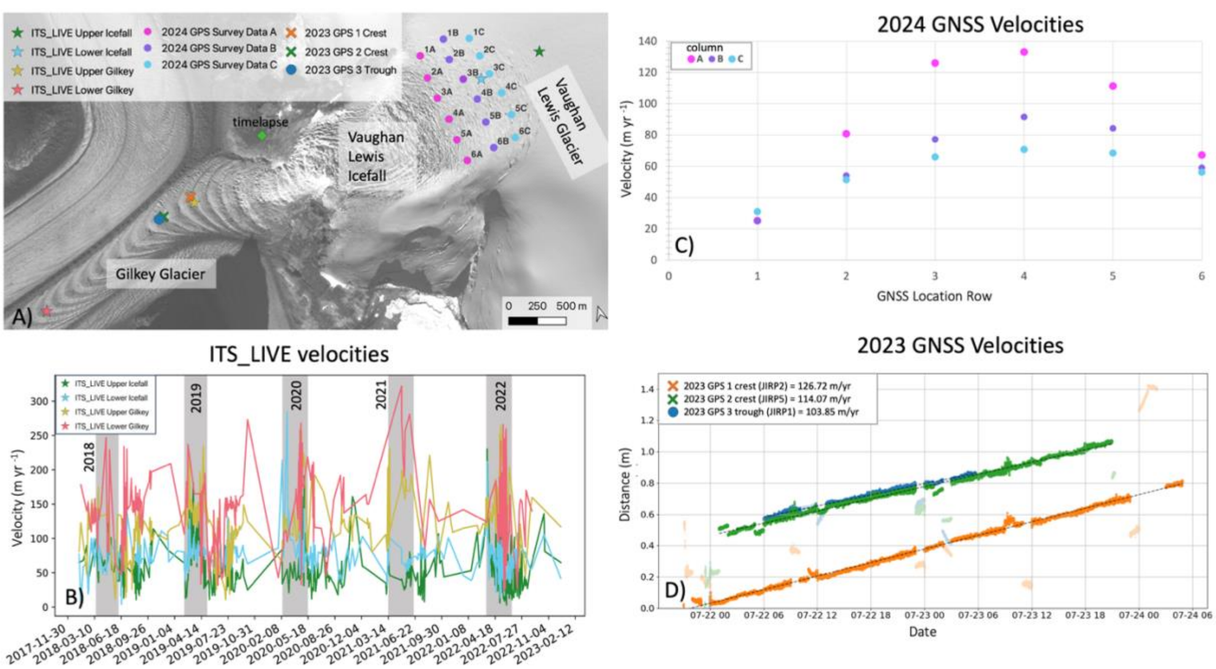

Figure 4.3: Velocity estimates from satellite remote sensing and in-situ data. A) Map of ITS_LIVE and GNSS measurement locations and timelapse camera (green diamond), on 10 October 2018 Worldview-1 image of the study area. B) ITS_LIVE velocity from January 2018 to December 2022 from two locations above the icefall and two locations below the icefall, denoted by colored stars. Gray shading are the annual periods of peak velocity; C) 2024 GNSS velocity from the array of GNSS units located above the icefall in July 2024; D) 2023 GNSS velocity of three GNSS units located on the lower Gilkey Glacier, the plot shows distance over time, where the slope

equals the velocity indicated in the top left corner next to the X and O that match the map. Data points that are opaque in color are outliers that are ignored for regression analysis.

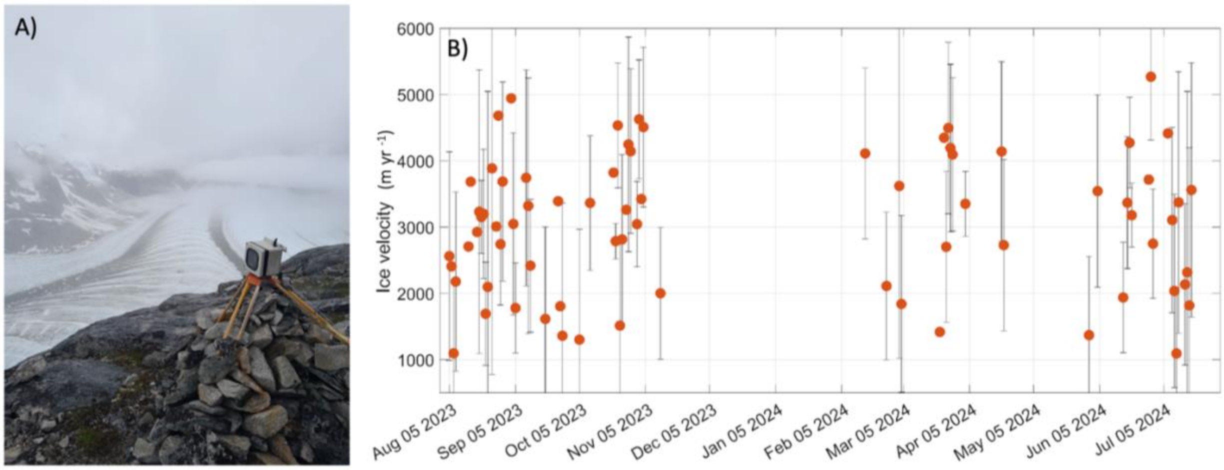

Figure 4.4: Velocity of the lower Vaughan Lewis Icefall derived from the timelapse camera imagery acquired from July 2022 to July 2023. The location of the camera is denoted by the green diamond in Figure 4.1, and by the green diamond in Figure 4.3. A) Photo of timelapse camera set-up; B) Timelapse camera derived velocities. Gray vertical lines are error bars for each data point taken as +/- 2 standard deviations of the mean velocity between the image pairs.

4.2 Icefall and ogive location analysis

In order to try to find a generalized relationship between icefalls, ogive presence, and seasonal velocity variations, we utilized the geographic dataset from Davies et al. (2022) and ITS_LIVE data. Davies et al. (2022) provide a comprehensive map of all of the geomorphological features on the Juneau Icefield, including icefalls, ogives, glaciers, and more. First we discarded icefalls that did not connect to a valley glacier. We also discarded ogives that were Forbes bands in style. We employed the ITS_LIVE data set to identify the seasonal velocity pattern below the icefalls and categorized those velocity patterns by ogive presence. Figure 4.5A shows our map of the location of the icefalls denoted by dots, which we colored based on our examination of icefall and ogive locations, where green indicates the presence of ogives, and red indicates no ogives. Figure 4.5B shows the annual variability in velocity measured at the base of the icefalls where there were ('true') and were not ('false') ogives present. In icefall-glacier locations where there were no ogives present, annual variability in velocity ranges from no variability to over 600 m yr^{-1} of variability, with a median of ~130 m yr^{-1}. In locations where ogives were present, the range in velocity variability is similar from no variability to over 550 m yr^{-1}, with a median of 180 m yr^{-1}. We discuss these findings in the Discussion section.

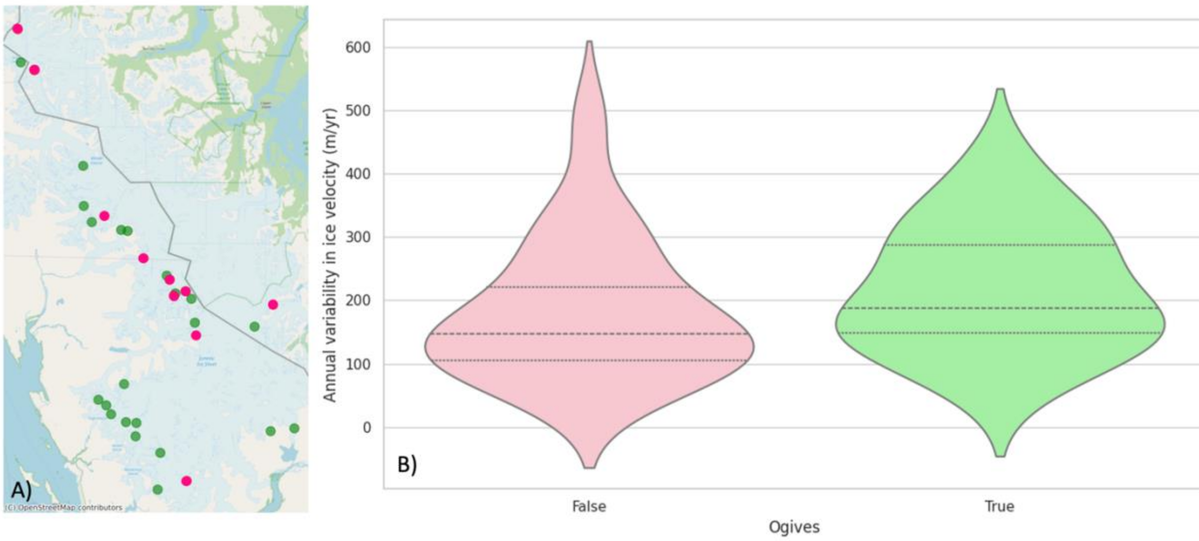

Figure 4.5: Locations of glaciers with icefalls in the Juneau Icefield, alongside ice velocity variability for glaciers with and without ogives. A) Map of icefall locations taken from Davies et al., 2022, green dots indicate presence of ogives and magenta indicates lack of ogives, background image from Open Street Maps. B) Violin plot of seasonal variability of ice velocity of locations with (green) and without (red) ogives, where the dashed lines are the median values and the dotted lines are the first and third quartiles.

4.3 Modeling results

4.3.1 Idealized glacier

In order to test the two primary theories of ogive formation, we first ran the finite difference model in an idealized glacier scenario. We chose parameter values that were able to create ogives with realistic topography in order to compare the two theories of formation. For both experiments, we chose initial parameter values from representative ranges from published literature and data (e.g., Burgess et al., 2013; Armstrong et al., 2017, McNeil et al., 2020). We experimented with these ranges and chose one to discuss here. We set the initial glacier thickness to 70 m and scaled the transition from icefall to valley glacier velocities with a length scale (λ) of 100 m.

To first test whether mass balance plays a significant role in ogive formation for an idealized glacier, we imposed a sinusoidal mass balance function and held the velocity steady throughout the year (Fig. 4.6A and C). The mass balance values were based on estimates of glaciers on the Juneau Icefield, such as Lemon Creek and Taku Glacier, 50 km and 25 km southeast of Gilkey Glacier, respectively (McNeil et al., 2020). The imposed seasonal mass balance varied along the glacier profile from +2 m to +4.5 m w.e. in the icefall, and -2.6 to +2.5 mwe at 2500 m downstream of the glacier, see Figure 4.6B, with a seasonal oscillation of approximately 3 m w.e.. At the ELA (x = 750 m), the mass balance decay begins such that downglacier of the base of the icefall the mass balance is slightly negative; ~ -0.2 m w.e. (Fig. 4.6C). We ran the model for 50 years, in order to allow enough time for the glacier thickness to reach a steady state. Figure 4.7A displays the modeled ice thickness along the glacier profile. Figure 4.7B shows the ice thickness anomaly resulting from the seasonal variability of mass balance. The ice thickness anomaly clearly shows ogives and allows us to analyze the amplitude and wavelength of the features. Downglacier from the top two ogives, the ogives tend to be less than 2 m in amplitude, have a wavelength of 160 m, and quickly diminish in amplitude and wavelength with distance downglacier.

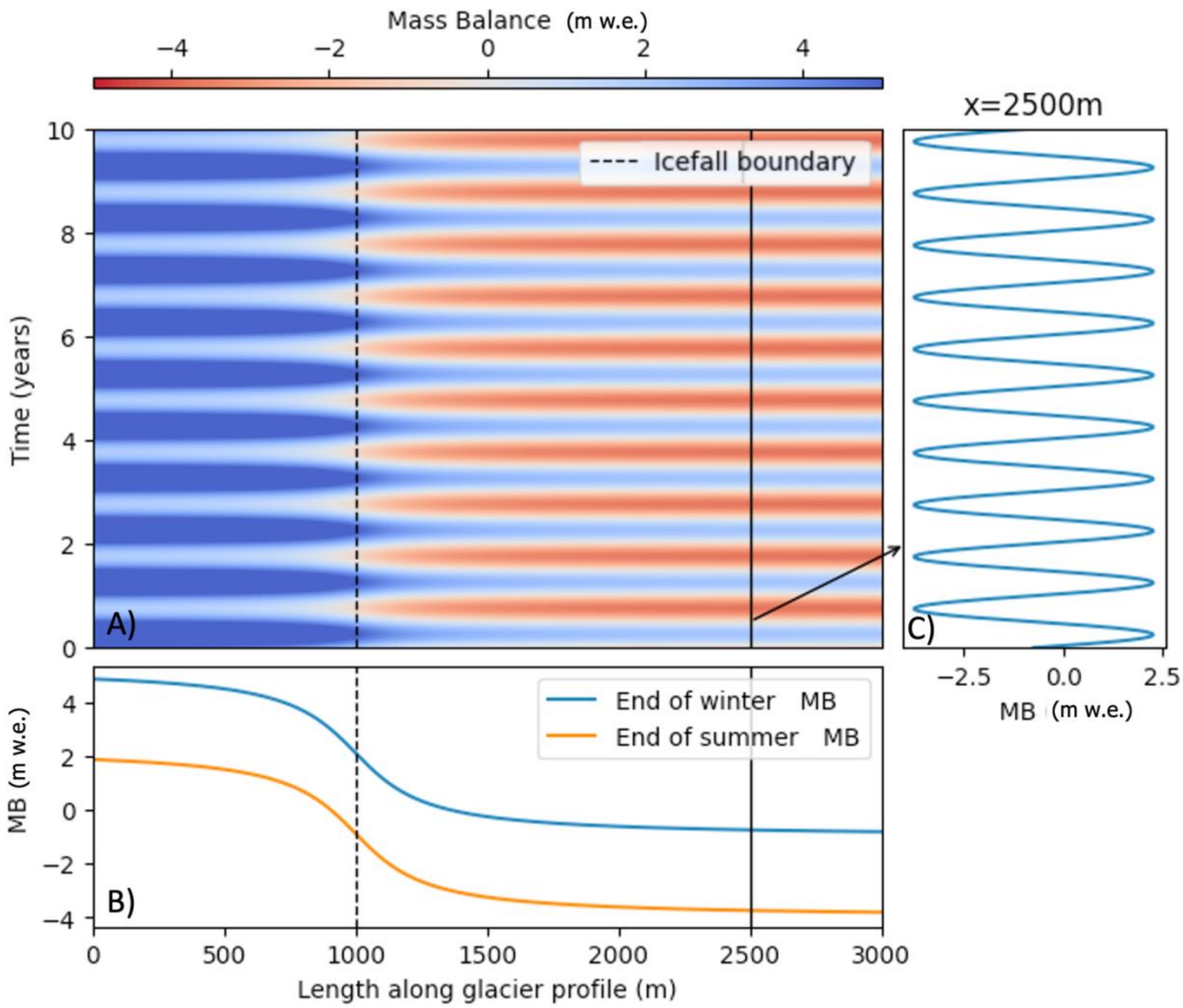

Figure 4.6: For an idealized glacier scenario, imposed values for the parameter surface mass balance sinusoidal function as a function of time and distance downglacier (results depicted in Fig. 4.7). Mass balance is denoted as MB A) Mass balance through time along the distance of the glacier profile, where 0 is an arbitrary point within the icefall and 1000 m is the base of the icefall. B) Seasonal mass balance variation along the glacier profile, where blue is the end of winter and summer is orange. Note that the ELA location is at roughly x=750 m, where the end of the year balance crosses 0. C) Sinusoidal function of the seasonal oscillation of mass balance at 2500 m distance along the glacier profile.

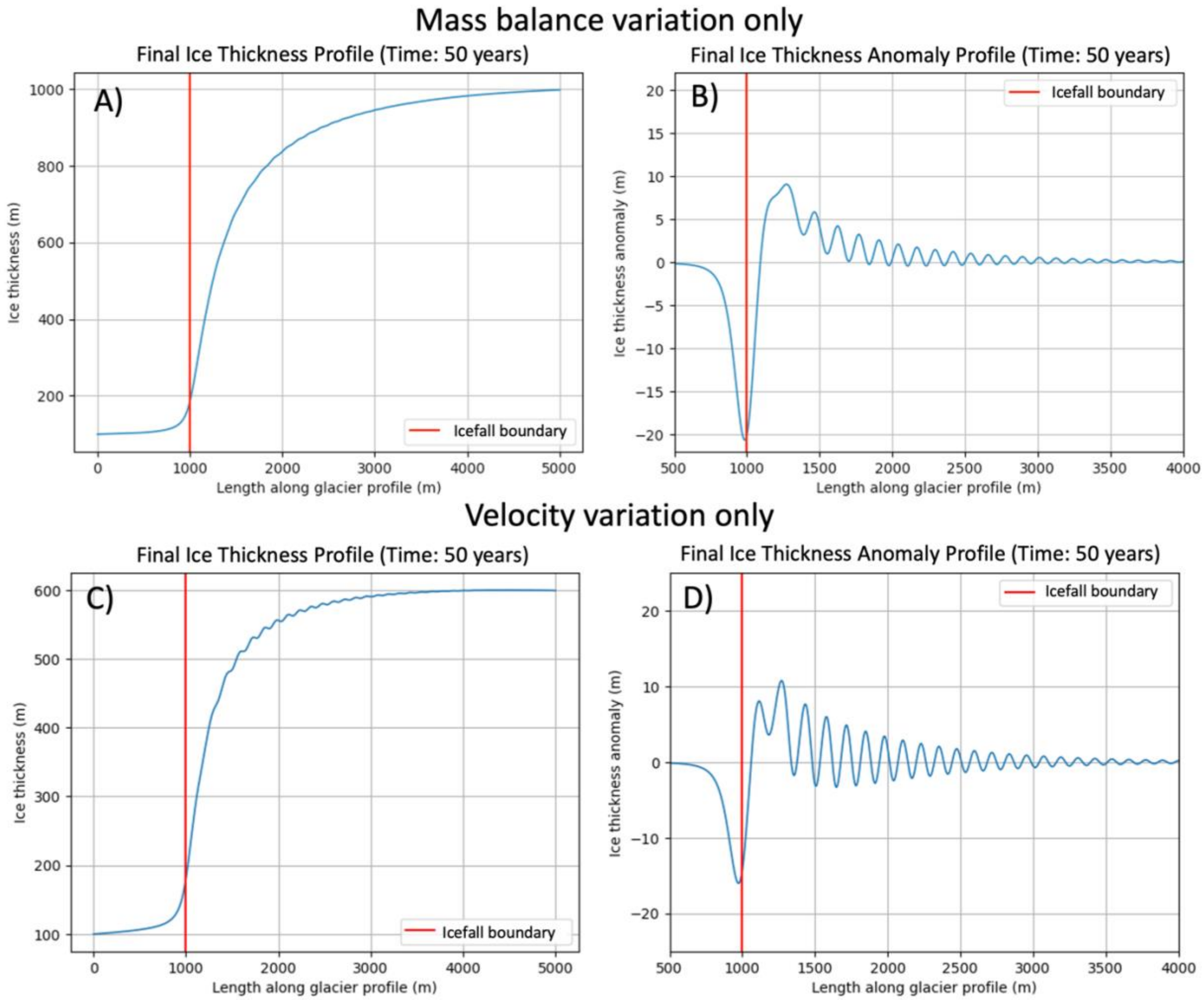

Figure 4.7: Idealized glacier model runs. Red vertical line depicts the base of the icefall in all plots. Note the different scales. A) Final ice thickness profile after 50 years of imposed mass balance variation only. Note ogives are barely depicted. B) Ice thickness anomaly when increasing ice thickness trend is removed, the true pattern of ogives is revealed. C) Final ice thickness profile after 50 years of imposed mass balance variation and seasonal velocity variation. D) Ice thickness anomaly along the glacier due to a seasonal velocity variation.

Next, we tested the role of seasonal velocity variation in ogive formation for the idealized glacier. To do this, we omitted any mass balance variation through time and held the icefall velocity constant through the year at 730 m yr^{-1}, as the hypothesis requires. We varied the velocity of the lower glacier from a minimum of 120 m yr^{-1} to a peak (i.e., the maximum in the seasonal pulse) of ~160 m yr^{-1}, values that optimized realistic ogive amplitudes. We ran this for

50 years (Fig. 4.8A-C). We defined the duration of the seasonal pulse to be approximately two months long (t_{sig}) and the timing of the peak sliding to be at 4.8 months (t_{slide}). We ran the model for 50 years. The model results show that with seasonal velocity variation, while mass balance is held constant, the ogives form immediately at the base of the icefall (Figs. 4.7C and D). The ogives reach amplitudes as high as 11 m, almost triple the size of the ogives formed from varying just mass balance for the idealized glacier. Downglacier from the top two ogives, the ogive wavelength is ~160 m and increases downglacier. We address this pattern in the Discussion.

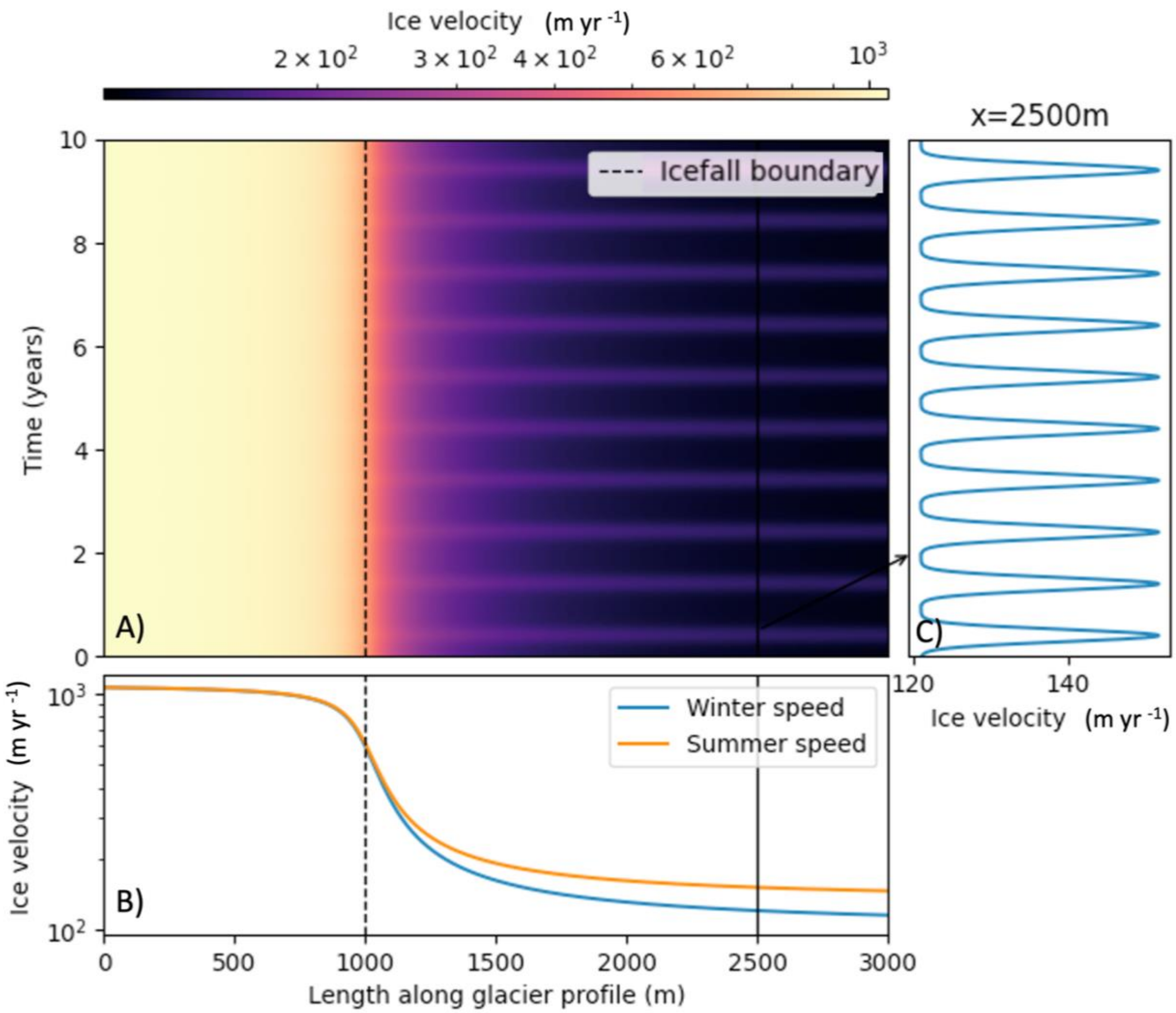

Figure 4.8: For an idealized glacier scenario, imposed values for velocity as a function of time and distance downglacier (results depicted in Fig. 4.7). A) Velocity through time along 3000 m

of the glacier profile. The icefall is set to a steady velocity of 730 m yr^{-1} and an initial ice thickness of 70 m. At 1000 m along the profile the icefall ends and the ice velocities are slower, while seasonal velocity variation begins downglacier from this point. B) The winter minimum (blue) and summer maximum (orange) velocities along the profile. C) The annual cycle of velocity variation at 2500 m along the distance of the profile with a minimum of 120 m yr^{-1} and a maximum of 150 m yr^{-1}.

4.3.2 Gilkey Glacier Experiment

In order to explore the output and limitations of the numerical model in a real glaciological setting, we employ the field-collected and satellite remote sensing data described above to constrain various parameter values in the model. We run the model with only the mass balance variation, then only the velocity variation, then both simultaneously. Arguably, the most important input parameters for the model are the characteristics of the velocities. Table 4.1 summarizes the datasets and the key velocity information for each data set.

Data	Location	Mean annual max(m yr^{-1})	Mean annual min (m yr^{-1})	Dataset mean velocity (m yr^{-1})
2024 GNSS data	Upper and lower VL	N/A	N/A	71
2023 GNSS data	Upper and lower Gilkey	N/A	N/A	115
ITS_LIVE	Upper and lower VL	177	32	65
ITS_LIVE	Upper and lower Gilkey	253	66	133
Timelapse imagery	Icefall	1835	2555	2190

Table 4.1. Summary of velocities in key sections of the Gilkey Glacier derived from a variety of datasets described in the Methods section.

We include the mass balance sinusoidal variation and the velocity gaussian pulse seasonal variation, separately and then together. We set the initial ice thickness to 70 m, the icefall velocity to 2190 m yr^{-1} and the lower Gilkey a seasonal velocity minimum of ~120 m yr^{-1}

and a peak reaching ~280 m yr^{-1} at the end of April, and the transition length of 100 m (Fig. 4.9). As in the idealized glacier model, we scale the transition length by ratio of the icefall width to the Gilkey Glacier ogive width (see Methods). Due to uncertainty in the mass balance of this particular glacier, we set the mass balance to be the same as the idealized glacier that is estimated from nearby glaciers on the Juneau Icefield (Fig. 4.6; see above and McNeil et al., 2020). We ran the model for 50 years. When we run only the mass balance variation, we find that ogives of an amplitude of <5 m are formed, relative to a total ice thickness of over 3000 m (Fig. 4.10A and B). When we run only the seasonal velocity variation, we find that ogives of an amplitude of 100 m are formed, relative to a total ice thickness of over 1700 m (Fig. 4.10C and D). When we include both seasonal mass balance variation and the velocity variation, we find large ogives of an amplitude of 125 m, a wavelength of ~200 m, and an ice thickness of up to 2500 m (Fig. 4.10D and E). The wavelength of the ogives declines from 300 m near the icefall to ~100 m at the end of the calculation space (i.e., downglacier); this change in wavelength is discussed further in the Discussion. The amplitude of the ogives decreases with distance from the base of the icefall; at 3000 m horizontally from the base of the icefall, the amplitude is only 10s of meters, coinciding with a decrease in wavelength to ~160 m.

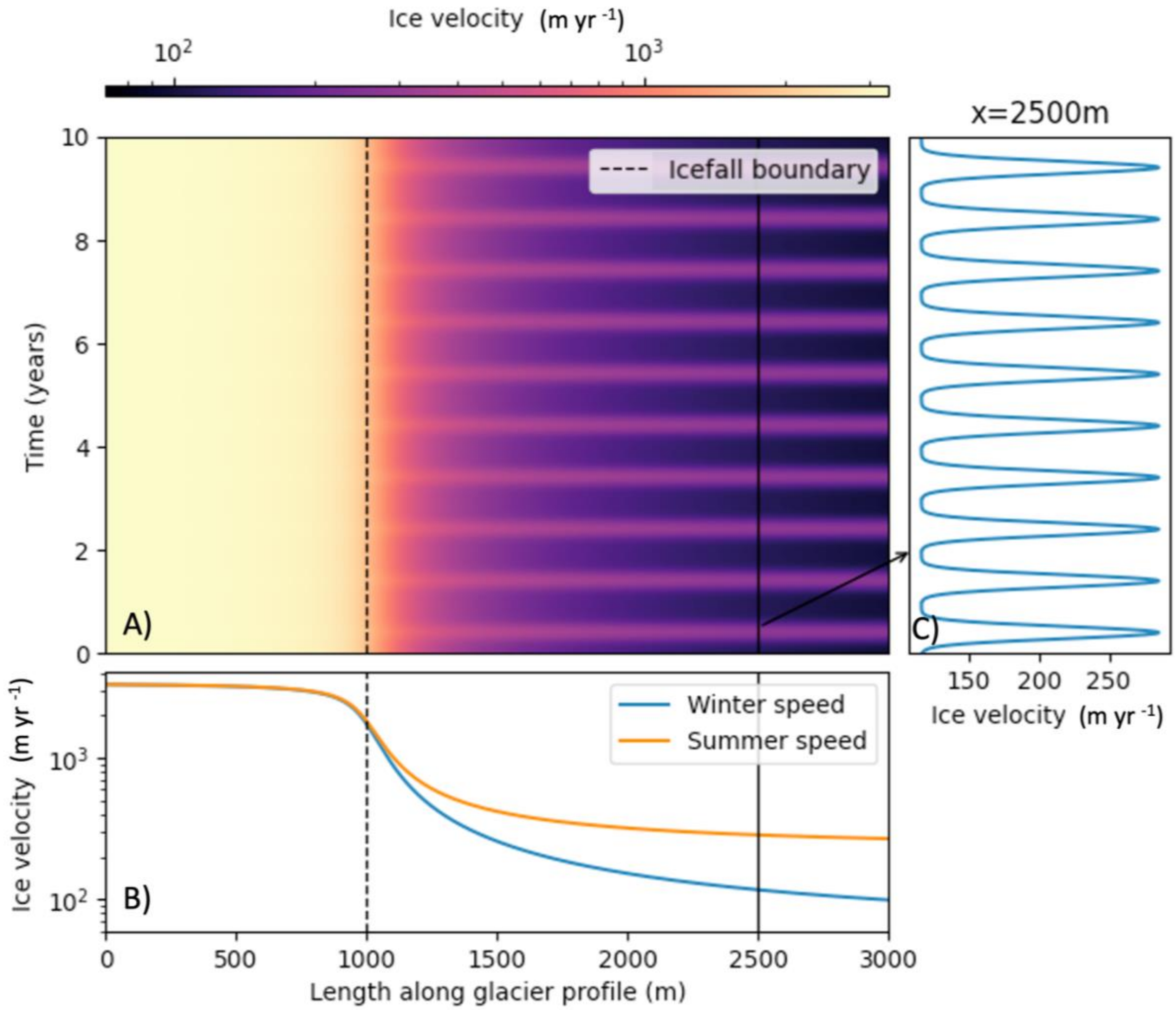

Figure 4.9: For the Gilkey Glacier scenario, imposed values for the parameter velocity variation as a function of time and distance downglacier. A) the seasonal velocity as it varies along the distance of the glacier through time; B) The velocity along the glacier profile, with winter (blue) and summer (orange) velocities depicted, and C) velocity variation over several annual cycles at a distance of 2500 m.

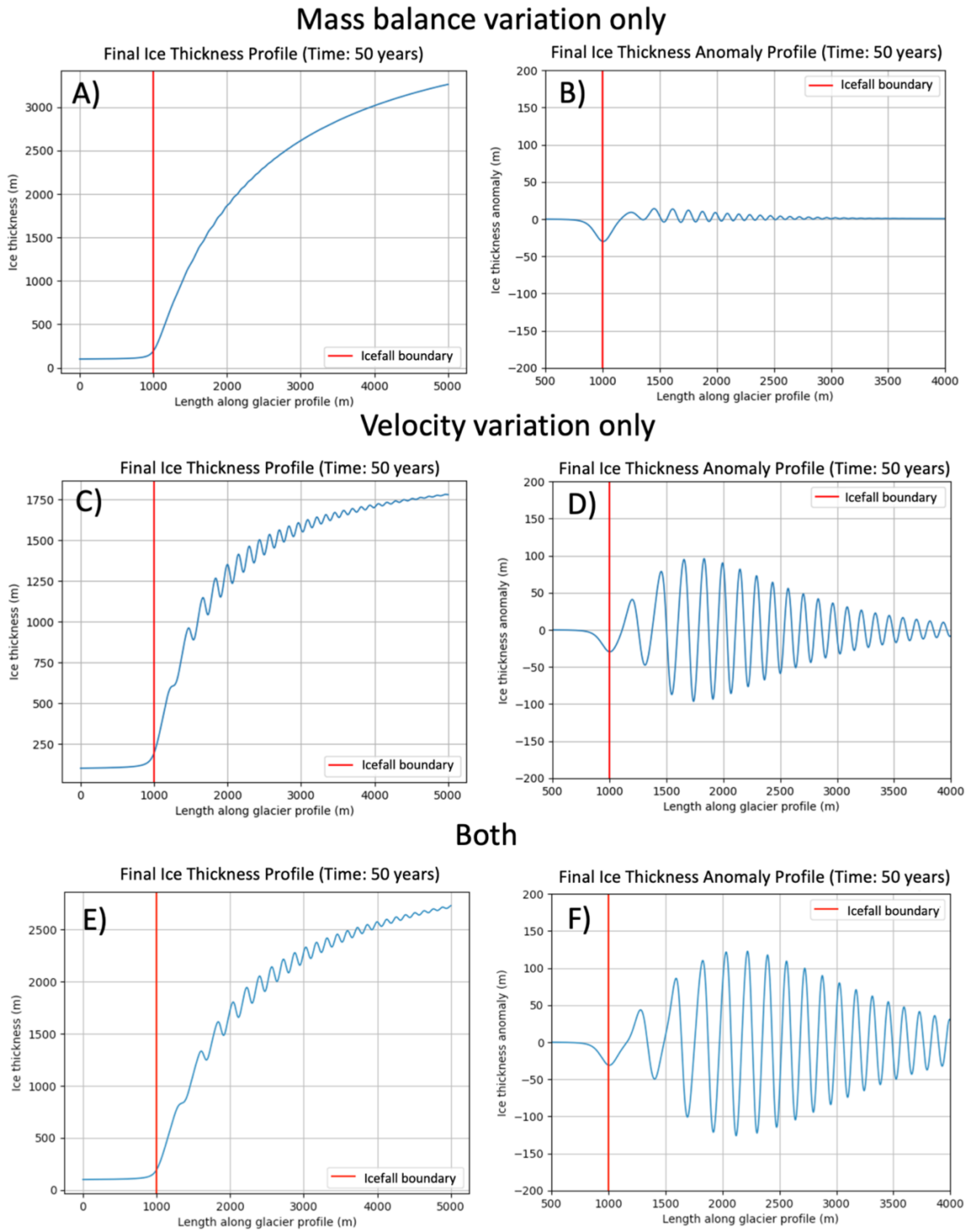

Figure 4.10: Results of the Gilkey Glacier model runs, after 50 years. The red vertical line represents the base of the icefall, approximately at the black X on Figure 4.1. For the imposed mass balance variation only, A) final ice thickness; and B) the ice thickness anomaly For the

imposed ice thickness variation only, C) final ice thickness; and D) the ice thickness anomaly. When both the mass balance and ice velocity variations are imposed on the model, E) final ice thickness; and F) the ice thickness anomaly.

5 Discussion

5.1 Characterization of Gilkey Glacier

Our study synthesizes data from two field campaigns, timelapse imagery, and the ITS_LIVE satellite dataset (Gardner et al., 2019). Although our study is focused on ogive formation for a specific glacier, this unique dataset allows us to further our understanding of plateau icefield systems in general. For example, very few prior studies have investigated icefall velocities (Armstrong et al., 2017), given their difficulty in measurement. Here we measured icefall velocities using timelapse imagery and found a nearly steady velocity throughout the year. This lack of intra-annual variation in ice velocity supports the notion that basal sliding in icefalls is minor, as seasonal variation in hydrology, i.e. which may alter subglacial water pressure, is unlikely through the icefall (Armstrong et al., 2017). Yet, we are unable to completely confidently partition the motion between internal deformation and sliding, as well as from toppling seracs that occur frequently.

Our measured icefall velocity of ~2200 m yr^{-1} is similar to that measured in the only other study that includes both ogives and icefall velocities (King and Lewis, 1961), which found that the top of the ogive-forming Odinsbre Icefall, Norway displayed velocities of ~2000 m yr^{-1}. Despite our results and those of King and Lewis (1961), not all icefalls move as quickly, for example the Khumbu Glacier Icefall has a measured velocity of ~365 m yr^{-1} (Altena and Kääb, 2020) and the Mer de Glace 700-800 m yr^{-1} (Berthier et al., 2005). It is not surprising that the velocity of icefalls varies with location. Given these high flow velocities, mass conservation suggests that the icefall ice thickness is much more thin than that of the upper and/or lower glacier.

Previous studies have suggested the relationship between ogive wavelength downglacier and annual glacier velocity is a way to study velocity changes through time (King and Lewis, 1961, Fisher 1962, Waddington 1986). For example, Aniya et al. (1988) attempted to employ variations in ogive wavelength with distance to reconstruct the glacier dynamic history of the Soler Glacier in Chile. In our study, we find that once the model has achieved a steady state, the wavelength of the ogives at the base of the Vaughan Lewis Icefall is indeed attributable to the annual mean velocity there, yet downglacier from the icefall, the wavelength declines despite relatively steady velocities (Fig. 4.1C). This suggests that one should not use ogive wavelengths as proxies of the history of glacier dynamics. Our modeled variations in ogive wavelength downglacier from the icefall is primarily due instead to changes in ice thickness and hence in ice surface velocity. In our model, which is driven by an imposed spatial distribution of sliding velocity, as sliding velocity declines, ice thickness must increase to conserve mass, as seen in Figure 4.10. As velocity declines, the modeled wavelength of surface features (i.e. ogives) declines. The reality on Gilkey glacier, based on our observations as opposed to modeling, is more nuanced. The ogive wavelengths (Fig. 4.1C) increase slightly with distance downglacier for ~1 km, before declining subtly thereafter. If this is not due to temporal variation in the original ogives generated at the base of the icefall, it must reflect the spatial variation in the velocity of the glacier: increasing velocities over the first kilometers, followed by slightly decreasing speeds over the next few kilometers.

5.2 Theories of ogive formation

Ogives have tantalized scientists for over a hundred years. There have been no recently published observations or models to explain how they are created, despite advances in understanding Forbes bands (Vincent et al., 2018; Goodsell et al., 2002). As stated in our introduction, the two main hypotheses for ogive formation are as follows: 1) The seasonal mass balance variation, suggests that in summer, greater ablation rates in the icefall are higher compared to the valley portion of the glacier, thus a smaller volume of ice enters the lower glacier, relative to winter. 2) The velocity variation hypothesis, suggests that a seasonal velocity variation in the lower glacier creates waves by summer acceleration, thinning the ice, and in winter slowdown, thickening the ice (Waddington, 1986).

In our idealized glacier model runs, we test the ability of each hypothesized formation process to create ogives of representative amplitudes. When we hold ice velocity steady and seasonally vary mass balance, we create small ogives with an amplitude of less than 2 m. These ogives are substantially smaller than what we observe on the Gilkey Glacier (with amplitudes of 11 m) or other ogives reported in Alaska; the nearby Antler Glacier has ogives with 5 m amplitude (Hashimoto et al., 1966). Therefore, although this mass balance driven formation process indeed can create ridge and trough topography, as Nye (1961) and Waddington (1986) proposed, it likely is not the dominant mechanism responsible for large amplitude ogives that we see around the world, including on the Gilkey Glacier.

When we test the seasonal velocity variation mechanism on the idealized glacier, while holding mass balance steady throughout the year, ogives of ~10 m in amplitude are created. This amplitude is much more similar to what we observe in nature, both on the Gilkey Glacier as well as other locations around Alaska (e.g. Root Glacier, ~11 m in amplitude, based on our ArcticDEM analysis).

When the model is applied to the Gilkey Glacier, although the magnitude of the resultant ogives and ice thickness differ to the results in the idealized model runs, a similar pattern emerges; the ogives formed from seasonal velocity variation alone are far larger in amplitude than those formed from the mass balance variation model run (<5 m for mass balance variation, compared to 125 m for velocity variation). These results, paired with those from the idealized glacier runs show that both the mass balance variation process and velocity variation process can produce ogives; however, it is clear the velocity variation can generate larger amplitude ogives even just with small variations in velocity (~40 m yr^{-1}).

When we constrain our numerical model with the velocity parameter values estimated from our in-situ and satellite derived observations of Gilkey Glacier, combined with the mass balance variation that we imposed previously, we illuminate limitations of our model and deduce information on ice plateau dynamics (Fig. 4.10C). We create unrealistically large amplitude ogives and an overly thick glacier (Figs. 4.9 and 4.10). Ogive amplitudes in this run reach 125 m and 166 m in wavelength that decrease downglacier, with glacier thickness over 2500 m (Fig. 4.10C). In reality, Gilkey Glacier's ogives are 5-8 m in amplitude and the estimated ice thickness is 300-500 m. Given the solution in the analytical model described in Methods, we anticipate that the velocity variation determines the ogive amplitude, which also scales with the ice thickness (Equation 7). Since our model produced ice thicknesses of over 2500 m, >5 times the estimated ice thickness, and we have a velocity variation magnitude of over 100 m yr^{-1}, we would expect to see ogives with amplitudes of 100s of m, >5 times the actual Gilkey Glacier ogives. We discuss the reason for our high modeled ice thickness in the next paragraph.

In the Gilkey Glacier model run, we assumed that the lower glacier and icefall velocities are uniform vertically through the glacier thickness, with ideal basal sliding conditions at the base and zero internal deformation. This creates an inverse relationship between velocity and ice thickness, as ice discharge is simply the product of sliding velocity and mean ice thickness across the width of the glacier. Due to this relationship, the high icefall velocities we employ create unrealistically thick ice at the base of the icefall. In reality, this relationship between ice velocity and ice thickness is highly nonlinear in cases where internal deformation of ice, captured by Glen's Flow Law, dominates; surface ice velocity is proportional to thickness raised to the fourth power (H^4), and ice discharge is proportional to ice thickness to the fifth power (H^5). If our model included internal deformation, we would not need as thick an ice mass to generate the observed several-fold reduction in ice velocities (the icefall velocity compared to the lower glacier velocity; Table 4.1). In addition, we have little constraint on the thickness of ice in the icefall. Due to the large difference between the Millan et al. (2022) and Farinotti et al. (2019) estimates of ice thickness of the Vaughan Lewis Glacier, a mass conservation estimate of the icefall thickness is not well-bounded. It is possible the icefall ice thickness is substantially thinner than our model's prescribed initial ice thickness of 70 m, although DEM data for the sercas suggest it is at least 20 m thick. Ideally, a future study would involve detailed ground penetrating radar (GPR) surveys of both the Vaughan Lewis Glacier and the Gilkey Glacier, the results of which would then impose strong constraints on the icefall ice thickness by conservation of mass.

For all the idealized glacier and Gilkey Glacier model experiments, our model produces ogive wavelengths that decline with horizontal distance from the base of the icefall. The wavelength reduces by almost 3-fold from the start of ogives to the end of our model domain, i.e. 3000 m downglacier. In contrast, our analysis of in-situ data of ogive wavelengths of the Gilkey Glacier shows an increase in wavelength before becoming nearly uniform for several kilometers. In fact, the decay of ogive wavelength in our model is likely an artifact of numerical diffusion. Employing second order upwind differencing in the model, which essentially includes three points in calculation of the gradient in discharge instead of just two, prevents this behavior. We also suggest the width scaling of our model could be improved upon, such that the model more accurately adjusts the velocity according to the width of the icefall and glacier. Here we simply use a proportion, but a more complex treatment of this feature may improve results. Finally, the shape of the velocity decay may also be adjusted, such that the deceleration occurs more abruptly with horizontal distance.

Despite the limitations of our model, the idealized glacier runs and the Gilkey Glacier runs inform us of the dominant ogive formation process. Our results suggest that seasonal mass balance alone is not sufficient to create the scale of the observed ogives in nature. Although ogives can be formed through this mechanism, seasonally varying velocity has far greater leverage on the size and wavelength of ogives. Therefore, we find the most plausible mechanism of ogive formation is seasonal variation in the velocity of the lower glacier.

Atherton (1963) utilized observations from the eastern fork of Vimmelskaftet, Greenland to form the original hypothesis of velocity variation driven ogive formation. He suggested the presence of multiple waves in the icefall was due to the increased strain during winter slowdowns. We see a similar pattern in the Vaughan Lewis Icefall (Fig. 4.1, Inset ii), lending additional support for this method of formation. Ultimately, the cause of the ogives is likely due to temporal variation in the strain field as the glacier slows down at the base of the icefall. The summer pulse of sliding will stretch and thin the ice over the distance it takes to accelerate, followed by a return to lower sliding velocities that will cause a greater negative gradient in velocity and hence thickening. However, it is still unclear why some icefalls do not form ogives, even with seasonally varying lower glacier velocities.

5.3 Why do ogives not form under all icefalls?

Our results suggest that ogive formation requires a seasonal velocity variation of the lower glacier below an icefall. Yet, not all icefalls create ogives, even when the lower glacier has a seasonal velocity variation. Figure 4.5 showed us that there is no clear relationship between the annual variability of ice velocity in the lower glacier and the presence of ogives. Therefore, despite our promising modeling results, variable velocity is not sufficient to determine whether or not ogives will form at the base of the icefall. So what (o)gives?

We propose several research avenues to investigate why not all icefalls form ogives. First, in our analysis of the Juneau Icefield region ogives (Fig. 4.5), we did not distinguish the amplitude or wavelength of the different ogive trains. It would be interesting to investigate the variety of ogive amplitudes and wavelengths in the Juneau Icefield. In addition, if we broaden our study area to include regions outside of Juneau that have ogives (e.g. Wrangell St. Elias National Park, Alaska), we could perform an analysis on the relationship of ogive presence and other characteristics such as the steepness and width of the icefall, the proportion of icefall width to valley glacier, the elevation difference of the icefall and lower glacier, minimum and maximum baseline velocities of the lower glacier and ice plateau areas, lower glacier ice thickness and many other factors. It would be ideal to examine these characteristics in greater detail utilizing the plethora of remote sensing tools and datasets (e.g. ITS_LIVE velocities, ArcticDEM, Millan et al., 2022 ice thickness, etc). To build upon the analysis modeling presented here, we can perform a series of sensitivity tests using the finite difference model to identify any parameter thresholds that may exist in the model. Areas of sensitivity analysis would include minimum and maximum values of seasonal velocity, seasonal velocity amplitude, and the velocity difference between the icefall and lower glacier. Additional field data collection would include measurement of the strain rate at the bottom of the icefalls, collecting GPR ice thickness measurements, and additional timelapse imagery focused on the base of the icefall, where ogives originate. An experimental investigation using glacier-like materials in a laboratory could also be employed. Lastly, our results suggest a plausible ogive formation mechanism, yet the process of ogive diffusion downstream remains to be explored.

6 Conclusions

Prior to this study, ogives have only been minimally studied. Despite the initial fascination in the early days of glaciology, their origin and representation of glacier dynamics has been relatively understudied since the 1980s. Ogives form in precarious glaciated regions, where icefalls meet valley glaciers. These regions are notoriously difficult to obtain field data due to access issues relating to safety. Even with the advent of satellite remote sensing, the highly dynamic topography of icefalls makes it difficult to track changes from space. Our study includes one of the first comprehensive datasets of velocities that cover the entire system, from the plateau icefield, through the icefall, down to the valley glacier. This complete velocity profile may help inform future studies on ice-plateau-icefall and feedback dynamics in a changing climate. We have tested ogive formation hypotheses by using our integrated dataset to constrain values for ice velocity in a finite difference model that is able to capture and test the plausibility of the existing hypotheses. We determined that ogive formation is plausible if there is a large seasonal velocity variation in the valley glacier below the icefall. We found that the seasonal mass balance ogive formation theory alone cannot explain the observed ogives amplitudes on the Gilkey Glacier. Further work is necessary to constrain whether a threshold of velocity variation for ogive formation exists, and/or other factors that might explain why not all icefalls create trains of ogives.

Acknowledgements

Polar Geospatial Center, Earthscope, CIRES Innovative Research Proposal program, NASA, The Canadian Geodetic Survey for GNSS processing, the Juneau Icefield Research Program students, researchers, and field staff: Iván Álvarez, Isabella Chittumuri, Carly Hayward, Kaia Neal, Dean Gelling, Jeet Patel, Morgan Abbruscato, Daniel Shapiro, Stine Ornes, Brian Rougeux, Christina Stahl, Cal Hobson, Sydney Bidwell, Emma Neuhauser, and Julia Kaltenborn. Coastal helicopters. The numerous people that provided helpful conversations and or code along the way; Julia "Jukes" Liu, Julianna Ruef, Ryan Cassotto, and more.

Data and materials availability

All Landsat-8 and 9 data are publicly available on https://search.earthdata.nasa.gov/. Worldview DEMs are available via PGC. ITS_LIVE data is available on its_live website (https://mappin.itsliveiceflow.science/). All code used for analysis is available on Github.

CHAPTER 5

1 Implications of the Larsen B fast-ice and tributary glacier dynamics

The work I have presented in Chapters 2 and 3 increases our understanding of ice-ocean systems in a changing climate. In these chapters, I presented a detailed analysis of the recent events that occurred in the Larsen B embayment on the Antarctic Peninsula. The results from Chapter 2 emphasize that ocean waves have the potential to contribute to ice-shelf and multi-year fast-ice instability. Although this idea is not new (Massom et al., 2018), my study adds to the growing consensus that ocean waves can play a significant role in the stability of floating ice bodies. In addition, this is the first recorded occurrence of a large wave swell driving the break-up of mutli-year fast-ice. The glacier response to the event was catastrophic: grounded regions of Crane Glacier experienced a 50% increase in speed, and Hektoria Glacier's speed increased by 600%. This increase in speed and associated thinning occurred simultaneously as both glaciers retreated into their fjords. Record-breaking thinning occurred on Hektoria and Green Glacier, and Hektoria's retreat was so extreme it warranted its own study (Chapter 3).

The immediate responses of Hektoria and Crane Glaciers to the Larsen B fast-ice collapse suggest a clear connection between their stability and the presence of the fast-ice. However, questions pertaining to the physics behind the ability of fast-ice to directly buttress glaciers remain, especially as to what exactly it means to "buttress." Sun et al. (2023) and Suraway-stepney et al. (2024) investigate the Larsen B fast-ice and conclude that the fast-ice was not providing a backstress to the grounded glaciers, but rather suppressed the calving of the glacier terminus, such that when the fast-ice broke up the calving of the floating ice tongues quickly followed. Other studies (e.g., Green et al., 2018; Miles et al., 2017) suggest that fast-ice is a stabilizing feature for grounded glaciers regardless of the degree of direct buttressing applied by the fast-ice. In contrast to Sun et al. (2023) and Suraway-Stepney et al (2024), Parsons et al.

(2024) quantified the backstress applied by the fast-ice on Crane Glacier's terminus in the Larsen B embayment, suggesting the fast-ice provided sufficient buttressing to the floating ice tongue to allow it to advance (i.e., calving was suppressed by its presence). Needell and Holshuch (2021) show an obvious slowdown on the grounded portion of Crane Glacier throughout the fast-ice occupation, which suggests that the fast-ice buttressed the grounded portion of the glacier. This lack of consensus on the ability of fast-ice to suppress calving and to provide a backstress to grounded glacier areas suggests further work is needed. My overview is that the controversy is partially due to semantics in what exactly qualifies as buttressing. How much of a backstress is required for fast-ice to "buttress" a glacier? Is it sufficient for it to simply suppress calving, or does it need to be enough to slow down the grounded glaciers? Regardless of the detailed answers to the questions posed, it is obvious that fast-ice plays an important role in glacier dynamics, glacier readvance, and requires further research.

In Chapter 2 we detail the events that led up to the break-out of the fast-ice and the outcomes of the event. We reported that the ice tongues that had re-advanced into the embayment 10+ km were over 300 m thick in some places, and when the fast-ice broke-up they also disintegrated within a month. The relationship between the fast-ice and the formation of the ice tongues suggests the possibility that fast-ice can support glacier extension and ice tongue advance. With several decades of uninterrupted cooling, we can infer that the ice tongues would have merged, ultimately producing an ice shelf. The early stages of this process were demonstrated by the ice tongue advance during the 2011-2022 fast-ice occupation at the Larsen B embayment. This suggests that one way ice shelves may form is during a cooling climate in which multi-decadal fast-ice forms in the glacier fjords and embayments, not unlike the formation of the Arctic-style ice shelves in the North (Jeffries et al., 2017), although the significantly warmer summer conditions there make the resulting ice shelves thinner and less stable. As the fast-ice suppresses calving and the ice tongue begins to advance, it will come into direct contact with fjord walls and pinning points, increasing the buttressing effect and thus advancing further, in a positive feedback. If the fast-ice still remains, the floating ice tongue may continue to replace the relatively thin (<20 m) fast-ice with several hundred meter thick ice, subsequently forming a true ice shelf. Ice shelves may form through another process, based on the retreat of a marine-based ice sheet during a prolonged warming period. Over multiple centuries, as warm ocean water erodes the grounding line, a new ice shelf may form, as predicted at Thwaites (Betts et al., 2024) and what has potentially happened in the Ross Sea Embayment since the mid-Holocene (Conway et al., 1999). A comprehensive study of the development of ice shelves via the presence of fast-ice would be valuable.

The retreat of Hektoria and Crane Glaciers in the aftermath of the loss of the fast-ice is alarming and warrants a deeper exploration of glacier instabilities are and what causes them. Although a marine ice cliff instability has been hypothesized (Deconto and Pollard, 2016), neither of these glaciers possessed terminal cliff heights greater than 100 m, suggesting ice cliff instability did not drive their rapid retreats. In Chapter 3, we find that the ice plain geometry at Hektoria Glacier is likely to have caused rapid buoyancy-driven retreat. This is the first recorded occurrence of the process in the modern record, and lends credence to Batchelor's (2023) hypothesis based on geomorphologic analysis of the bathymetry formerly covered by the Scandinavian Ice Sheet during the last glacial maximum. The rapid buoyancy-driven retreat resulted from a gradual thinning that occurred over several months following the fast-ice break-up. Once the glacier thinned to near flotation the whole area lifted off the ground and calved away, essentially surpassing a tipping point. This is a new type of instability that may occur after reaching such a tipping point. A new stable terminus appears to have been established on Hektoria Glacier, 10 km from its previous grounding zone, although it continues to thin at rates greater than 80 m yr^{-1}.

As a scientific community, our preoccupation around instabilities as runaway processes needs a paradigm shift. We may be overlooking processes that can result in a period of instability followed by a new normal. That period of instability may very well be catastrophic, as was the case of Hektoria Glacier. If something like that were to happen on, for example, Thwaites Glacier in central West Antarctica, even just a few kilometers of retreat occurring over several months would be calamitous. Our results highlight the need to redefine rapid glacier retreat, and show that we need to include retreat mechanisms that occur in pulses, not only in complete runaway processes in our ice sheet and consequent sea level rise models. We need to put forth greater research effort into how we can define these pulses, determine what starts them and what can stop them.

2 Broader impact of ice dynamics of ogives in Alaska

My study in Chapter 4 investigates ogive formation. Ogives form in valley glaciers at the bottom of icefalls, yet how they form has remained an enigma to scientists since the mid 1800s (Forbes, 1845). I synthesize geophysical data from remote sensing and field campaigns to characteristize of the ogives below the Vaughan Lewis Icefall. This is the first comprehensive study that includes velocities data of an ice plateau, icefall, and lower glacier.

We find that as the plateau ice is funneled through a narrow chute (the icefall), it accelerates 30-fold, before decelerating 20-fold as it enters the lower glacier. We found that the seasonal velocity variation at the top of the icefall and in the icefall itself, is minimal. However, in the lower glacier, the velocity variation is such that the annual peak pulse is nearly double that of the mean annual velocity. We use these velocity measurements to constrain a finite difference model in combination with idealized glacier conditions to test the two main hypotheses of ogive formation: seasonal mass balance variation and seasonal velocity variation of the lower glacier. With all experiments, we find that Gilkey Glacier is not a special case, ogives can be formed using velocity and mass balance values commonly observed in Alaskan glaciers today. More importantly, we find that the dominating process of ogive formation is the seasonal velocity variation, as opposed to seasonal surface mass balance variation. Despite our study's limitations, which are discussed in detail in Chapter 4, our results may spark renewed interest in modeling ogive formation processes, ice plateau-icefall dynamics, and other crest-trough topographic patterns on glaciers. In the following paragraphs, I discuss Chapter 4 in the context of these broader themes.

Our model assumes ice flow velocity is entirely controlled by basal sliding, i.e., I assume no internal deformation. In reality, it is likely that internal deformation accounts for a significant proportion of the minimum ice velocity. In future research, utilizing a model that includes both internal deformation and basal sliding would help to better elucidate the controlling factors on ogive formation, in particular the temporal and spatial patterns of sliding. I also recommend investigating ogive formation in plastic deformation models to provide insight into the buckling capacity of ice, and running 2D full-stokes models to examine the complex ssgrss associated with the base of icefalls.

Our study is unique in its documentation of velocity measurements. These can be used in future studies for icefall dynamics, including understanding icefall velocities and icefall disconnection. Due to access and safety concerns, icefall velocities are extremely difficult to measure. We provide a year-long velocity time series derived from timelapse camera imagery. These data help to confirm the hypothesis that icefall velocities are near-steady throughout the annual cycle, perhaps reflecting a well-drained subglacial hydrologic system (Armstrong et al., 2017). In addition, this comprehensive dataset may aid in research efforts focused on investigating the effects of climate change on ice plateaus in glaciated regions, such as the timing of icefall disconnections. An icefall disconnection occurs when an icefall that drains a plateau icefield becomes disconnected with a lower glacier. When this happens, both the plateau icefield and the lower glacier become stagnant and eventually melt away through significant melt-accelerating feedbacks (Davies et al., 2024). Future studies may combine our velocity results with projected climate scenarios to identify when the icefalls will become disconnected, thus potentially enabling us to predict the fate of the valley glaciers and ice plateaus. In addition, it is possible to use old satellite imagery or aerial photographs to date previous icefall disconnections to determine how quickly these events may occur in the future (e.g., Little Vaughan Lewis Icefall; Davies et al., 2022). Our geophysical measurements offer a foundation of in-situ data to further investigate tipping points in this dynamic glacier system.

Lastly, ogives are not the only wave like feature in glacier ice. There are several other glaciological phenomena in which waves, sometimes called “rolls” or “rumples” are created. On ice shelves, in both the Arctic and Antarctic, undulating surface topography originates from compressive stresses that cause the glacier ice to buckle and/or to create rumples (Jefferies, 2017; MacAyeal et al., 2021). In the Arctic, a relationship between the wavelength of the rumples and the thickness of the ice was identified (Jefferies, 2017; Ochwat et al., 2023). In both Arctic and Antarctic rumples, the distinct peak-valley topography originates from a process that differs from ogives, and has specific consequences for ice dynamics in these systems. For example, the rumpling of ice shelves causes them to weaken and lose much of their buttressing force against upstream glacier ice (Borstad and others, 2013; MacAyeal et al., 2021). Well-known examples of such rumples in Antarctica are those on the McMurdo Ice Shelf, adjacent to the New Zealand Scott Base research station, as well as those on the Brunt Ice Shelf, called the McDonald Ice Rumples. However, we suggest that there are some parallels between glacier ogives and ice shelf rumples due to the compressional forces that may help to drive their formations, further research is needed to examine stresses in the icefall and lower glacier.

Another example of waves in ice features can be seen in rock glaciers where there are distinct lobes of debris that have notable "ridge and furrow" topography. However, these wave-like features likely originate from pulses of glaciation (Lehmann et al., 2024; Anderson et al., 2018) and can provide insights into paleoclimate characteristics and paleo-glaciological processes. As one of the most unique solid substances on Earth, ice has a tendency to form distinct wave-like patterns, all due to different processes that can affect ice dynamics in various ways. This natural phenomena can tell us more about the fascinating physics of ice, its viscous-elastic behavior, and its place in our world.

3 Commonalities between ice dynamics at the Larsen B embayment and ogives in Alaskan valley glaciers

This dissertation seeks to further the understanding of glaciers in systems that are susceptible to irreversible change. As described above, Chapter 2 and 3 investigate the Larsen B system and glacier instabilities of floating ice and tidewater glaciers. Due to the loss of the fast-ice, Hektoria Glacier experienced a tipping point at which it rapidly retreated at rates never before seen in the modern record. Chapter 4 explores the formation of ogives, which only occur at the base of icefalls. Since icefalls are increasingly disconnecting from their large valley glaciers below, ogives will soon be disappearing as well. It is in our best interest to study their formation before that tipping point is reached. These two seemingly different systems are both undergoing rapid changes as climate change continues to wreak havoc on our icy world. In both cases, we need to study the dynamics of the ice, from rapid retreat processes, to origins of ogive formation, before it is too late. As a last thought, it is worth acknowledging that the Antarctic Peninsula is an ice plateau with icefalls that feed large valley glaciers, so what we can glean from Alaska now will contribute to our understanding of the ice dynamics in that region in the future. Perhaps one day, there will be ogives at Crane Glacier.

REFERENCES

Adusumilli, S., Fricker, H. A., Siegfried, M. R., Padman, L., Paolo, F. S., and Ligtenberg, S. R. M.:. Variable basal melt rates of Antarctic Peninsula ice shelves, 1994–2016. Geophys. Res. Lett., 45, 4086–4095. doi:10.1002/2017GL076652, 2018.

Alley, R. B., Cuffey, K. M., Bassis, J. N., Alley, K. E., Wang, S., Parizek, B. R., Anandakrishnan, S., Christianson, K., and DeConto, R. M.: Iceberg calving: regimes and transitions, Annu. Rev. Earth Planet. Sci., 51, 189–215, 2023.

Altena, B., and Kääb, A.: Ensemble matching of repeat satellite images applied to measure fast-changing ice flow, verified with mountain climber trajectories on Khumbu icefall, Mount Everest, J. Glaciol., 66(260), 905–915, doi:10.1017/jog.2020.66, 2020.

Anandakrishnan, S., Voigt, D., Alley, R., and King, M.: Ice stream D flow speed is strongly modulated by the tide beneath the Ross Ice Shelf, Geophysical Research Letters, 30, 2003.

Anderson, R.S., Anderson, L.S., Armstrong, W.H., Rossi, M.W. and Crump, S.E.: Glaciation of alpine valleys: The glacier–debris-covered glacier–rock glacier continuum. Geomorphology, 311, pp.127-142. doi:10.1016/j.geomorph.2018.03.015, 2018.

Aniya, M., Casassa, G., and Naruse, R.: Morphology, Surface Characteristics, and Flow Velocity of Soler Glacier, Patagonia, Arctic Alpine Res., 20(4), 414–421, doi:10.1080/00040851.1988.12002694, 1988.

Antropova, Y., Mueller, D., Samsonov, S., Komarov, A., et al.: Grounding-line retreat of Milne glacier, Ellesmere Island, Canada over 1966–2023 from satellite, airborne, and ground radar data Remote Sensing of Environment, 2024.

Amundson, J. M., Fahnestock, M., Truffer, M., Brown, J., Lüthi, M. P., and Motyka, R. J.: Ice mélange dynamics and implications for terminus stability, Jakobshavn Isbræ, Greenland, J. Geophys. Res., 115, F01005, doi:10.1029/2009JF001405, 2010.

Armstrong, W. H., Anderson, R. S., and Fahnestock, M. A.: Spatial patterns of summer speedup on south central Alaska glaciers, Geophys. Res. Lett., 44, 9379–9388, doi:10.1002/2017GL074370, 2017.

Arthur, J., Stokes, C., Jamieson, S., Miles, B., Carr, J., and Leeson, A.: The triggers of the disaggregation of Voyeykov Ice Shelf (2007), Wilkes Land, East Antarctica, and its subsequent evolution, J. Glaciol, 67(265), 933-951. doi:10.1017/jog.2021.45, 2021.

Atherton, D.: Comparisons of Ogive Systems Under Various Regimes, J. Glaciol., 4(35), 547–557, doi:10.3189/S0022143000028082, 1963.

Banwell, A. F., MacAyeal, D. R., and Sergienko, O. V.: Breakup of the Larsen B Ice Shelf triggered by chain reaction drainage of supraglacial lakes, Geophys. Res. Lett., 40, 5872–5876, doi:10.1002/2013GL057694, 2013.

Banwell, A. F. and Macayeal, D. R.: Ice-shelf fracture due to viscoelastic flexure stress induced by fill/drain cycles of supraglacial lakes, Antarct. Sci., 27(6), 587-597, doi:10.1017/S0954102015000292, 2015.

Banwell, A. F., Willis, I. C., Goodsell, B., Macdonald, G. J., Mayer, D., Powell, A. and MacAyeal, D. R.: Calving and Rifting on McMurdo Ice Shelf, Antarctica, Ann. Glaciol., 58(75pt1), 78-87, doi:10.1017/aog.2017.12, 2017.

Banwell, A. F., Datta, R. T., Dell, R. L., Moussavi, M., Brucker, L., Picard, G., Shuman, C. A., and Stevens, L. A.: The 32-year record-high surface melt in 2019/2020 on the northern George VI Ice Shelf, Antarctic Peninsula, Cryosphere, 15, 909–925, doi:10.5194/tc-15-909-2021, 2021.

Banwell, A.F., Wever, N., Dunmire, D., and Picard, G.: Quantifying Antarctic-wide ice-shelf surface melt volume using microwave and firn model data: 1980 to 2021, Geophys. Res. Lett., doi:10.1029/2023GL102744, 2023.

Banwell, A. F., Willis, I. C., Stevens, L. A., Dell, R. L., and MacAyeal, D. R.: Observed meltwater-induced flexure and fracture at a doline on George VI Ice Shelf, Antarctica, J. Glaciol., 1–14, doi:10.1017/jog.2024.31, 2024.

Bassis, J. N., and Walker, C. C.: Upper and lower limits on the stability of calving glaciers from the yield strength envelope of ice, Proc. R. Soc. A, 468(2140), 913-931, 2012.

Bassis, J. N., Berg, B., Crawford, A. J., and Benn, D. I.: Transition to marine ice cliff instability controlled by ice thickness gradients and velocity, Science, 372(6548), 1342– 1344. doi:10.1126/science.abf6271, 2021.

Batchelor, C. L., Christie, F. D. W., Ottesen, D., et al.: Rapid, buoyancy-driven ice-sheet retreat of hundreds of metres per day, Nature, 617, 105–110, doi:10.1038/s41586-023-05876-1, 2023.

Benn, D. I., Åström, J., Zwinger, T., Todd, J., Nick, F. M., Cook, S., Hulton, N. R. and Luckman, A.: Melt-under-cutting and buoyancy-driven calving from tidewater glaciers: New insights from discrete element and continuum model simulations, J. Glaciol., 63(240), 691-702. doi:10.1017/jog.2017.41, 2017.

Bernat, M., Belart, J., Berthier, E., Jóhannesson, T., Hugonnet, R., Dehecq, A., Magnússon, E., and Gunnarsson, A.: Geodetic mass balance of Mýrdalsjökull ice cap, 1999–2021, Jökull, 73, 35–53, 2023.

Berthier E., Vadon H., Baratoux D., Arnaud Y., Vincent C., Feigl K. L., Rémy F. and Legrésy B. Surface motion of mountain glaciers derived from satellite optical imagery. Remote Sensing of Environment, 95(1), doi: 10.1016/j.rse.2004.11.005, 2005.

Berthier, E., Scambos, T. A., and Shuman, C. A.: Mass loss of Larsen B tributary glaciers (Antarctic Peninsula) unabated since 2002, Geophys. Res. Lett., 39(13), 1–6. doi:10.1029/2012GL051755, 2012.

Bevan, S. L., Luckman, A. J., Kuipers Munneke, P., Hubbard, B., Kulessa, B., and Ashmore, D. W.: Decline in surface melt duration on Larsen C Ice Shelf revealed by the advanced scatterometer (ASCAT), Earth Space Sci., 5, 578–591. doi:10.1029/2018EA000421, 2018.

Borstad, C. P., Rignot, E., Mouginot, J. and Schodlok, M. P.: Creep deformation and buttressing capacity of damaged ice shelves: theory and application to Larsen C ice shelf, Cryosphere, 7(6), 1931-1947, doi:10.5194/tc-7-1931-2013, 2013.

Bozkurt, D., Rondanelli, R., Marin, J. C., and Garreaud, R.L: Foehn event triggered by an atmospheric river underlies record-setting temperature along continental Antarctica, J. Geophys. Res. Atmos, 123, 3871–3892. doi:10.1002/2017JD027796, 2018.

Braun, M., Humbert, A., and Moll, A.: Changes of Wilkins Ice Shelf over the past 15 years and inferences on its stability, The Cryosphere, 3, 41–56, https://doi.org/10.5194/tc-3-41-2009, 2009

Brinkerhoff, D., Truffer, M., and Aschwanden, A.: Sediment transport drives tidewater glacier periodicity, Nat Commun, 8, 90, 2017.

van den Broeke, M.: Strong surface melting preceded collapse of Antarctic Peninsula ice shelf, Geophys. Res. Lett., 32, L12815, doi:10.1029/2005GL023247, 2005.

Brunt, K. M., Fricker, H. A., and Padman, L.: Analysis of ice plains of the Filchner–Ronne Ice Shelf, Antarctica, using ICESat laser altimetry, Journal of Glaciology, 57, 965–975, 2011.

Burgess, E., Forster, R., and Larsen, C.: Flow velocities of Alaskan glaciers, Nat. Commun., 4, 2146, doi:10.1038/ncomms3146, 2013.

Calafat, F. M., Wahl, T., Tadesse, M. G., et al.: Trends in Europe storm surge extremes match the rate of sea-level rise, Nature, 603, 841–845, doi:10.1038/s41586-022-04426-5, 2022.

Cape, M. R., Vernet, M., Skvarca, P., Marinsek, S., Scambos, T. and Domack, E.: Foehn winds link climate-driven warming to ice shelf evolution in Antarctica, J. Geophys. Res. Atmos, 120(21), 11-037, doi:10.1002/2015JD023465, 2015.

Catania, G. A., Stearns, L. A., Sutherland, D. A., Fried, M. J., Bartholomaus, T. C., Morlighem, M., Shroyer, E., and Nash, J.: Geometric controls on tidewater glacier retreat in central western Greenland, JGR Earth Surface, 123, 2024–2038, 2018.

Carrasco, J. F., Bozkurt, D., and Cordero, R.: A review of the observed air temperature in the Antarctic Peninsula. Did the warming trend come back after the early 21st hiatus?, Polar Sci., 28, 100653. doi: 0.1016/j.polar.2021.100653, 2021.

Cassotto, R., Fahnestock, M., Amundson, J., Truffer, M., and Joughin, I.: Seasonal and interannual variations in ice mélange and its impact on terminus stability, Jakobshavn Isbræ, Greenland, J. Glaciol., 61(225), 76-88. doi:10.3189/2015JoG13J235, 2015.

Conway, H., Hall, B. L., Denton, G. H., Gades, A. M., and Waddington, E. D.: Past and Future Grounding-Line Retreat of the West Antarctic Ice Sheet, Science, 286, 280-283, doi:10.1126/science.286.5438.280, 1999.

Cook, A. J. and Vaughan, D. G.: Overview of areal changes of the ice shelves on the Antarctic Peninsula over the past 50 years, Cryosphere, 4(1), 77-98, doi:10.5194/tc-4-77-2010, 2010.

Copland, L. and Sharp, M.: Mapping thermal and hydrological conditions beneath a polythermal glacier with radio-echo sounding, Journal of Glaciology, 47, 232–242, 2001.

Corr, H. F., Doake, C., Jenkins, A., and Vaughan, D. G.: Investigations of an “ice plain” in the mouth of Pine Island Glacier, Antarctica, Journal of Glaciology, 47, 51–57, 2001.

Clerc, F., Minchew, B. M., and Behn, M. D.: Marine ice cliff instability mitigated by slow removal of ice shelves, Geophysical Research Letters, 46, 12108–12116, 2019.

Crawford, A. J., Benn, D. I., Todd, J., Åström, J. A., Bassis, J. N., and Zwinger, T.: Marine ice-cliff instability modelling shows mixed-mode ice-cliff failure and yields calving rate parameterization, Nat. Comm., 12(1), 2701, https://doi.org/10.1038/s41467-021-23070-7. 2021

Datta, R. T., Tedesco, M., Fettweis, X., Agosta, C., Lhermitte, S., Lenaerts, J. T. M., and Wever, N.: The effect of Foehn-induced surface melt on firn evolution over the northeast Antarctic peninsula, Geophys. Res. Lett., 46, 3822– 3831, doi:10.1029/2018GL080845, 2019.

Davies, B., Bendle, J., Carrivick, J., McNabb, R., McNeil, C., Pelto, M., et al.: Topographic controls on ice flow and recession for Juneau Icefield (Alaska/British Columbia), Earth Surf. Process. Landforms, 47(9), 2357–2390, doi:10.1002/esp.5383, 2022.

Davies, B., McNabb, R., Bendle, J., et al.: Accelerating glacier volume loss on Juneau Icefield driven by hypsometry and melt-accelerating feedbacks, Nat. Commun., 15, 5099, doi: 10.1038/s41467-024-49269-y, 2024.

DeConto, R., and Pollard, D.: Contribution of Antarctica to past and future sea-level rise, Nature, 531, 591–597, doi:10.1038/nature17145, 2016.

Doake, C., and Vaughan, D.: Rapid disintegration of the Wordie Ice Shelf in response to atmospheric warming, Nature, 350, 328–330, doi:10.1038/350328a0, 1991.

Dussaillant, I., Berthier, E., Brun, F., Masiokas, M., Hugonnet, R., Favier, V., Rabatel, A., Pitte, P., and Ruiz, L.: Two decades of glacier mass loss along the Andes, Nature Geoscience, 12, 802–808, 2019.

Fahnestock, M., Scambos, T., Moon, T., Gardner, A., Haran, T., and Klinger, M.: Rapid large-area mapping of ice flow using Landsat 8, Remote Sens Environ, 185, 84-94. doi:10.1016/j.rse.2015.11.023, 2016.

Favier, L., Durand, G., Cornford, S. L., Gudmundsson, G. H., Gagliardini, O., Gillet-Chaulet, F., Zwinger, T., Payne, A. J., and Le Brocq, A. M.: Retreat of Pine Island Glacier controlled by marine ice-sheet instability, Nature Clim Change, 4, 117–121, 2014.

Fluegel, B., and Walker, C.: The two-decade evolution of Antarctica's Hektoria Glacier and its 2022 rapid retreat from satellite observations, Geophysical Research Letters, in review, 2024.

Fogt, R. L., and Marshall, G. J.: The Southern Annular Mode: Variability, trends, and climate impacts across the Southern Hemisphere. Rev. Clim. Change, 11(4), 1–24. doi:10.1002/wcc.652, 2020.

Forbes, J. D.: Travels through the Alps of Savoy and other parts of the Pennine chain: with observations on the phenomena of glaciers, A. and C. Black, 1845.

Fox, C., and Squire, V. A.: Coupling between the ocean and an ice shelf. Ann. Glaciol., *15*, 101-108, doi:10.3189/1991AoG15-1-101-108, 1991.

Fox-Kemper, B., Hewitt, H. T., Xiao, C., Aðalgeirsdóttir, et al.: Ocean, cryosphere and sea level change, in Climate Change 2021: The Physical Science Basis. Contribution of Working Group I to the Sixth Assessment Report of the Intergovernmental Panel on Climate Change, [Masson-Delmotte, V. et al. (eds.)], Cambridge University Press, Cambridge, United Kingdom and New York, NY, USA, 1211–1362, 2021, doi:10.1017/9781009157896.011.

Francis, D., Mattingly, K. S., Lhermitte, S., Temimi, M., and Heil, P.: Atmospheric extremes caused high oceanward sea surface slope triggering the biggest calving event in more than 50 years at the Amery Ice Shelf, The Cryosphere, 15, 2147–2165, https://doi.org/10.5194/tc-15-2147-2021, 2021

Francis, D., Fonseca, R., Mattingly, K. S., Marsh, O. J., Lhermitte, S., and Cherif, C.: Atmospheric triggers of the Brunt Ice Shelf calving in February 2021, J. Geophys. Res. Atmos, 127, e2021JD036424. https://doi.org/10.1029/2021JD036424, 2022.

Fraser, A. D., Massom, R. A., Handcock, M. S., Reid, P., Ohshima, K. I., Raphael, M. N., Cartwright, J., Klekociuk, A. R., Wang, Z., and Porter-Smith, R.: Eighteen-year record of circum-Antarctic landfast-sea-ice distribution allows detailed baseline characterisation and reveals trends and variability, Cryosphere, 15, 5061–5077, doi:10.5194/tc-15-5061-2021, 2021.

Fretwell, P., Pritchard, H. D., Vaughan, D. G., et al.: Bedmap2: improved ice bed, surface and thickness datasets for Antarctica, The Cryosphere, 7, 375–393, doi:10.5194/tc-7-375-2013, 2013.

Freer, B. I., Marsh, O. J., Hogg, A. E., Fricker, H. A., and Padman, L.: Modes of Antarctic tidal grounding line migration revealed by ICESat-2 laser altimetry, The Cryosphere, 1–35, 2023.

Friedl, P., Weiser, F., Fluhrer, A., and Braun, M. H.: Remote sensing of glacier and ice sheet grounding lines: A review, Earth-Sci. Rev., 201, 102948, https://doi.org/10.1016/j.earscirev.2019.102948, 2020.

Fricker, H. A., Coleman, R., Padman, L., Scambos, T. A., Bohlander, J., and Brunt, K. M.: Mapping the grounding zone of the Amery Ice Shelf, East Antarctica using InSAR, MODIS, and ICESat, Antarctic Science, 21, 515–532, 2009.

Fürst, J. J., Hogg, A. E., and Phillips, T.: The importance of ice shelf buttressing to the stability of the West Antarctic Ice Sheet, Nat. Commun., 7, 11623, doi:10.1038/ncomms11623, 2016.

Gades, A. M., Raymond, C. F., Conway, H., and Jagobel, R.: Bed properties of Siple Dome and adjacent ice streams, West Antarctica, inferred from radio-echo sounding measurements, Journal of Glaciology, 46, 88–94, 2000.

Gardner, A. S., Moholdt, G., Scambos, T., Fahnstock, M., Ligtenberg, S., Broeke, M.V.D. and Nilsson, J.: Increased West Antarctic and unchanged East Antarctic ice discharge over the last 7 years. Cryosphere, 12(2), 521-547. doi:10.5194/tc-12-521-2018, 2018.

Gardner, A., Fahnestock, M., and Scambos, T.: MEaSUREs ITS_LIVE Landsat image-pair glacier and ice sheet surface velocities. Data archived at National Snow and Ice Data Center, Version 1, 2019.

Gilbert, E., and Kittel, C.: Surface melt and runoff on Antarctic ice shelves at 1.5°C, 2°C, and 4°C of future warming. Geophys. Res. Lett., 48, e2020GL091733, https://doi.org/10.1029/2020GL091733, 2021.

Glasser, N. F. and Scambos, T. A.: A structural glaciological analysis of the 2002 Larsen B ice-shelf collapse, J. Glaciol., 54(184), 3-16, doi:10.3189/002214308784409017, 2008.

Glasser, N. F., Scambos, T. A., Bohlander, J., Truffer, M., Pettit, E., and Davies, B. J.: From ice-shelf tributary to tidewater glacier: continued rapid recession, acceleration and thinning of Röhss Glacier following the 1995 collapse of the Prince Gustav Ice Shelf, Antarctic Peninsula. J. Glaciol., 57(203), 397–406, doi:10.3189/002214311796905578, 2011.

Gomez-Fell, R., Rack, W., Purdie, H., and Marsh, O.: Parker Ice Tongue collapse, Antarctica, triggered by loss of stabilizing land-fast sea ice. Geophys. Res. Lett., 49, e2021GL096156. doi:10.1029/2021GL096156, 2022.

Goodsell, B., Hambrey, M. J., and Glasser, N. F.: Formation of band ogives and associated structures at Bas Glacier d'Arolla, Valais, Switzerland, J. Glaciol., 48(161), 287–300, doi:10.3189/172756502781831494, 2002.

Greene, C. A., Young, D. A., Gwyther, D. E., Galton-Fenzi, B. K., and Blankenship, D. D.: Seasonal dynamics of Totten Ice Shelf controlled by sea ice buttressing, The Cryosphere, 12, 2869–2882, doi:10.5194/tc-12-2869-2018, 2018.

Gudmundsson, G. H., Paolo, F. S., Adusumilli, S., and Fricker, H. A.: Instantaneous Antarctic ice sheet mass loss driven by thinning ice shelves, Geophys. Res. Lett., 46, 13903–13909, 2019.

Hashimoto, S., Shimizu, H., and Nakamura, K.: Glaciological Studies of the Antler Glacier, Alaska, J. Faculty Sci., Hokkaido Univ. Ser. 4, Geol. Miner., 13(3), 237–256, 1966.

Hersbach, H., Bell, B., Berrisford, P., et al.: The ERA5 global reanalysis. Q J R Meteorol Soc., 146. 1999–2049. https://doi.org/10.1002/qj.3803, 2020.

Holmes, C. R., Bracegirdle, T. J., and Holland, P. R.: Antarctic sea ice projections constrained by historical ice cover and future global temperature change. Geophys. Res. Lett., 49, e2021GL097413. doi:10.1029/2021GL097413, 2022.

Howat, I. M., Porter, C., Smith, B. E., Noh, M.-J., and Morin, P.: The reference elevation model of Antarctica, The Cryosphere, 13, 665–674, 2019.

Howat, I., Porter C., Noh, M-J., Erik, H., Samuel, K., Danish, E., Tomko, K., Gardiner, J., Negrete, A., Yadav, B., Klassen, J., Kelleher, C., Cloutier, M., Bakker, J., Enos, J., Arnold, G., Bauer, G., Morin, P.: The Reference Elevation Model of Antarctica - Strips, Version 4.1, Harvard Dataverse, V1, doi:10.7910/DVN/X7NDNY, 2022.

Hugonnet, R., McNabb, R., Berthier, E., et al.: Accelerated global glacier mass loss in the early twenty-first century, Nature, 592, 726–731, doi:10.1038/s41586-021-03436-z, 2021

Hulbe, C. L., Scambos, T. A., Youngberg, T. and Lamb, A.K.: Patterns of glacier response to disintegration of the Larsen B ice shelf, Antarctic Peninsula. Glob Planet Change, 63(1), 1-8, doi:10.1016/j.gloplacha.2008.04.001, 2008.

Huss, M. and Farinotti, D.: A high-resolution bedrock map for the Antarctic Peninsula, The Cryosphere, 8, 1261–1273, 2014.

Intergovernmental Panel on Climate Change: Climate Change 2021: The Physical Science Basis. Contribution of Working Group I to the Sixth Assessment Report of the Intergovernmental Panel on Climate Change (V. Masson-Delmotte, P. Zhai, A. Pirani, S. L. Connors, C. Péan, S. M. Berger, et al. (Eds.)), Cambridge University Press, doi:10.1017/9781009157896, 2021.

Jeffries, M.: The Ellesmere Ice Shelves, Nunavut, Canada. In Copland, L. and Mueller, D. (Eds.), Arctic Ice Shelves and Ice Islands, Dordrecht: Springer, pp. 23–55, 2017.

Jeffries, M. O.: Arctic ice shelves and ice islands: origin, growth and disintegration, physical characteristics, structural-stratigraphic variability, and dynamics. Rev. Geophys. 30(3), 245–267. doi:10.1029/92RG00956, 1992.

Joughin, I., Smith, B. E., and Medley, B.: Marine ice sheet collapse potentially under way for the Thwaites Glacier Basin, West Antarctica, Science, 344, 735–738, 2014.

Khazendar, A., Rignot, E. and Larour, E.: Larsen B Ice Shelf rheology preceding its disintegration inferred by a control method. Geophys. Res. Lett., 34(19), doi:10.1029/2007GL030980, 2007.

King, C. & Lewis, W.: A tentative theory of ogive formation, Journal of Glaciology, 3.29, 912–939, https://doi.org/10.3189/S0022143000027283, 1961.

King, J. C., Turner, J., Marshall, G. J., Connolley, W. M. and Lachlan-Cope, T .A.: Antarctic Peninsula climate variability and its causes as revealed by analysis of instrumental records. Antarct. Res. Ser., 79, 17-30, doi:10.1029/AR079p0017, 2003.

Krischer, L., Hutko, A. R., van Driel, M., Stähler, S., Bahavar, M., Trabant, C., and Nissen-Meyer, T.: On-demand custom broadband synthetic seismograms, Seismological Research Letters, 88, 1127–1140, 2017.

Kwon, H., Choi, H., Kim, B.M., Kim, S.W. and Kim, S.J.: Recent weakening of the southern stratospheric polar vortex and its impact on the surface climate over Antarctica. Environ. Res. Lett., 15(9), 094072, doi:10.1088/1748-9326/ab9d3d, 2020.

Laffin, M. K., Zender, C. S., van Wessem, M., and Marinsek, S.: The role of föhn winds in eastern Antarctic Peninsula rapid ice shelf collapse, Cryosphere, 16, 1369–1381, doi:10.5194/tc-16-1369-2022, 2022.

Langhorne, P.J., Squire, V.A., Fox, C. and Haskell, T.G., 2001. Lifetime estimation for a land-fast ice sheet subjected to ocean swell. Annals of Glaciology, 33, 333, https://doi.org/10.3189/172756401781818419.

Larour, E., Rignot, E., Poinelli, M., and Scheuchl, B.: Physical processes controlling the rifting of Larsen C Ice Shelf, Antarctica, prior to the calving of iceberg A68. PNAS, 118 (40), e2105080118, https://doi.org/10.1073/pnas.2105080118, 2021

Leeson, A. A., Van Wessem, J. M., Ligtenberg, S. R. M., Shepherd, A., Van Den Broeke, M. R., Killick, R., ... and Colwell, S.: Regional climate of the Larsen B embayment 1980-2014. J. Glaciol., 63(240), 683–690. https://doi.org/10.1017/jog.2017.39, 2017.

Lehmann, B., Anderson, R., Cusicanqui, D., Rossi, M., Ochwat, N.: Exploring Holocene climate history and alpine landscape evolution from rock glacier dynamics: Mt Sopris, CO, USA, Journal of Geohphysical Research: Earth Surfaces, submitted, 2024.

Lei, Y., Gardner, A. and Agram, P.: Autonomous Repeat Image Feature Tracking (autoRIFT) and Its Application for Tracking Ice Displacement. Remote Sens, 13(4), 749. doi:10.3390/rs13040749, 2021.

Li, X., Cai, W., Meehl, G. A., Chen, D., Yuan, X., Raphael, M., ... and Song, C.: Tropical teleconnection impacts on Antarctic climate changes, Nat Rev Earth Environ, 2(10), 680–698. doi:10.1038/s43017-021-00204-5, 2021.

Liang, K., Wang, J., Luo, H., and Yang, Q.: The role of atmospheric rivers in Antarctic sea ice variations. Geophys. Res. Lett., 50, e2022GL102588. https://doi.org/10.1029/2022GL102588, 2023.

van Lipzig, N. P. M., Marshall, G. J., Orr, A., and King, J. C.: The Relationship between the Southern Hemisphere Annular Mode and Antarctic Peninsula Summer Temperatures: Analysis of a High-Resolution Model Climatology. J. Climate, 21, 1649–1668, doi:10.1175/2007JCLI1695.1, 2008.

Luckman, A., Quincey, D., and Bevan, S.: The potential of satellite radar interferometry and feature tracking for monitoring flow rates of Himalayan glaciers, Remote Sensing of Environment, 111, 172–181, 2007.

Marshall, G. J., Orr, A., van Lipzig, N. P., and King, J. C.: The Impact of a Changing Southern Hemisphere Annular Mode on Antarctic Peninsula Summer Temperatures. J. Climate, 19, 5388–5404, doi:10.1175/JCLI3844.1, 2006.

MacAyeal, D. R., Sergienko, O. V., Banwell, A. F., Macdonald, G. J., Willis, I. C., and Stevens, L. A.: Treatment of ice-shelf evolution combining flow and flexure, J. Glaciol., 67(265), 885–902, doi:10.1017/jog.2021.39, 2021.

Massom, R. A., Giles, A. B., Fricker, H. A., Warner, R. C., Legrésy, B., Hyland, G., Young, N., and Fraser, A. D : Examining the interaction between multi-year fast ice and the Mertz Glacier Tongue, East Antarctica: Another factor in ice sheet stability?, J. Geophys. Res., 115, C12027, doi:10.1029/2009JC006083, 2010.

Massom, R. A., Scambos, T. A., Bennetts, L. G., Reid, P., Squire, V. A., and Stammerjohn, S. E.: Antarctic ice shelf disintegration triggered by sea ice loss and ocean swell, Nature, 558.7710, 383-389, doi:10.1038/s41586-018-0212-1, 2018.

Matsuoka, K., Skoglund, A., Roth, G., de Pomereu, J., Griffiths, H., Headland, R., and 18 others; Quantarctica, an integrated mapping environment for Antarctica, the Southern Ocean, and sub-Antarctic islands. Environmental Modelling & Software, 140, 105015, https://doi.org/10.1016/j.envsoft.2021.105015, 2021.

McGrath, D., Sass, L., O'Neel, S., Arendt, A. & Kienholz, C.: Hypsometric control on glacier mass balance sensitivity in Alaska and northwest Canada, Earth's Future, 5, 324–336, 2017.

McNeil, C., O'Neel, S., Loso, M., Pelto, M., Sass, L., Baker, E. H., & Campbell, S.: Explaining mass balance and retreat dichotomies at Taku and Lemon Creek Glaciers, Alaska, Journal of Glaciology, 66(258), 530–542, doi:10.1017/jog.2020.22, 2020.

Meehl, G. A., Arblaster, J. M., Bitz, C. M., Chung, C. T. & Teng, H.: Antarctic sea- ice expansion between 2000 and 2014 driven by tropical Pacific decadal climate variability. Nat. Geosci. 9, 590–595, doi:10.1038/ngeo2751, 2016.

Meier, M., and Post, A.: Fast tidewater glaciers, Journal of Geophysical Research: Solid Earth, 92, 9051–9058, 1987.

Meier, W. N., T. Markus, and J. C. Comiso.: AMSR-E/AMSR2 Unified L3 Daily 12.5 km Brightness Temperatures, Sea Ice Concentration, Motion & Snow Depth Polar Grids, Version 1. Boulder, Colorado USA. NASA National Snow and Ice Data Center Distributed, Active Archive Center. Accessed May 2022. doi:10.5067/RA1MIJOYPK3P, 2018.

Melton, S., Alley, R., Anandakrishnan, S., Parizek, B., Shahin, M., Stearns, L., . . . Finnegan, D.: Meltwater drainage and iceberg calving observed in high-spatiotemporal resolution at Helheim Glacier, Greenland. J. Glaciol., 68(270), 812-828, doi:10.1017/jog.2021.141, 2022.

Mercer, J. H.: West Antarctic ice sheet and CO2 greenhouse effect: a threat of disaster, Nature, 271, 321–325, https://doi.org/10.1038/271321a0, 1978.

Messerli, A. & Grinsted, A.: Image GeoRectification and Feature Tracking toolbox: ImGRAFT, Geosci. Instrum. Method. Data Syst., 4, 23–34, doi:10.5194/gi-4-23-2015, 2015.

Millan, R., Mouginot, J., Rabatel, A., & Morlighem, M.: Ice velocity and thickness of the world’s glaciers, Nat. Geosci., https://doi.org/10.1038/s41561-021-00885-z, 2022.

Miles, B. W. J., Stokes, C. R., and Jamieson, S. S. R.: Simultaneous disintegration of outlet glaciers in Porpoise Bay (Wilkes Land), East Antarctica, driven by sea ice break-up, The Cryosphere, 11, 427–442, https://doi.org/10.5194/tc-11-427-2017, 2017.

Miles, B. W. J., Stokes, C. R., and Jamieson, S. S. R.: Velocity increases at Cook Glacier, East Antarctica, linked to ice shelf loss and a subglacial flood event, The Cryosphere, 12, 3123–3136, https://doi.org/10.5194/tc-12-3123-2018, 2018.

Moon, T., Joughin, I., and Smith, B.: Seasonal to multiyear variability of glacier surface velocity, terminus position, and sea ice/ice mélange in northwest Greenland, J. Geophys. Res. Earth Surf., 120, 818– 833. doi: 10.1002/2015JF003494, 2015.

Morlighem, M. (2020). *MEaSUREs BedMachine Antarctica*. (NSIDC-0756, Version 2). Boulder, Colorado USA. NASA National Snow and Ice Data Center Distributed Active Archive Center. https://doi.org/10.5067/E1QL9HFQ7A8M. Date Accessed 09-19-2023.

Morlighem, M., Rignot, E., Binder, T., Blankenship, D., et al.: Deep glacial troughs and stabilizing ridges unveiled beneath the margins of the Antarctic ice sheet, Nature Geoscience, 13, 132–137, 2020.

Murray, T., Selmes, N., James, T. D., Edwards, S., Martin, I., O'Farrell, T., Aspey, R., Rutt, I., Nettles, M., and Baugé, T.: Dynamics of glacier calving at the ungrounded margin of Helheim Glacier, southeast Greenland. *J*. Geophys. Res. Earth Surf., 120, 964–982. doi:10.1002/2015JF003531, 2015

Murty, T. S.: Modification of hydrographic characteristics, tides, and normial modes by ice cover. Mar. Geod., 9(4), 451-468. doi:10.1080/15210608509379538, 1985.

Needell, C., and Holschuh, N.: Evaluating the retreat, arrest, and regrowth of Crane Glacier against marine ice cliff process models. Geophys. Res. Lett., 50, e2022GL102400. https://doi.org/10.1029/2022GL102400, 2023.

Nettles, M., and Ekström, G.: Glacial earthquakes in Greenland and Antarctica, Annual Review of Earth and Planetary Sciences, 38, 467–491, 2010.

Nicholls, K. W., Pudsey, C. J., and Morris, P.: Summertime water masses off the northern Larsen C Ice Shelf, Antarctica, Geophysical Research Letters, 31, 2004.

Nye, J. F.: A theory of wave formation in glaciers, Physics of the Movement of Ice, IAHS Publications, 47, 139–154, 1958.

Nye, J. F.: The deformation of a glacier below an ice fall, Journal of Glaciology, 3(25), 386–408, https://doi.org/10.3189/S0022143000017081, 1959.

Ochwat, N., Scambos, T., Fahnestock, M., and Stammerjohn, S.: Characteristics, recent evolution, and ongoing retreat of Hunt Fjord Ice Shelf, northern Greenland, J. Glaciol., 1–14, doi:10.1017/jog.2022.44, 2022.

Ochwat, N., Scambos, T., Fahnestock, M. and Stammerjohn, S.: Characteristics, recent evolution, and ongoing retreat of Hunt Fjord Ice Shelf, northern Greenland. J. Glaciol., 69(273), 57-70, doi:10.1017/jog.2022.44, 2023a.

Ochwat, N., Banwell, A., and Scambos, T., Larsen B fast-ice breakout and initial glacier response [in “State of the Climate 2023"]. Antarctica and the Southern Ocean, Bull. Amer. Meteor. Soc., 104 (9), S349-S351, https://doi.org/10.1175/BAMS-D-23-0077.1, 2023b.

Olsen, K. G., Nettles, M., Cathles, L. M., Burton, J. C., Murray, T., and James, T. D.: Improved estimation of glacial-earthquake size through new modeling of the seismic source, Journal of Geophysical Research: Earth Surface, 126, e2021JF006384, 2021.

O’Neel, S., Echelmeyer, K., and Motyka, R.: Short-term flow dynamics of a retreating tidewater glacier: LeConte Glacier, Alaska, USA, J. Glaciol., 47, 567–578, 2001.

O’Neel, S., Pfeffer, W. T., Krimmel, R., and Meier, M.: Evolving force balance at Columbia Glacier, Alaska, during its rapid retreat, J. Geophys. Res., 110, 2005JF000292, 2005.

Orr, A., Marshall, G. J., Hunt, J. C. R., Sommeria, J., Wang, C., van Lipzig, N. P. M., Cresswell, D., and King, J. C.: Characteristics of Summer Airflow over the Antarctic Peninsula in Response to Recent Strengthening of Westerly Circumpolar Winds. J. Atmos. Sci., 65, 1396–1413, https://doi.org/10.1175/2007JAS2498.1, 2008.

Parizek, B. R., Christianson, K., Alley, R. B., Voytenko, D., Vaňková, I., Dixon, T. H., ... and Holland, D. M.: Ice-cliff failure via retrogressive slumping, Geology, 47(5):449-452, doi:10.1130/G45880.1, 2019.

Parsons, R., Sun, S., Gudmundsson, G. H., Wuite, J., and Nagler, T.: Quantifying the buttressing contribution of sea ice to Crane Glacier, EGUsphere, 2024, 1–17, 2024.

Pendleton, S. L., Miller, G. H., Anderson, R. A., Crump, S. E., Zhong, Y., Jahn, A., and Geirsdottir, Á.: Episodic Neoglacial expansion and rapid 20th century retreat of a small ice cap on Baffin Island, Arctic Canada, and modeled temperature change, Clim. Past, 13, 1527–1537, doi:10.5194/cp-13-1527-2017, 2017.

Pfeffer, W. T.: A simple mechanism for irreversible tidewater glacier retreat, J. Geophys. Res., 112, 2006JF000590, 2007.

Picard, G., Fily, M., and Gallee, H., 2007. Surface melting derived from microwave radiometers: A climatic indicator in Antarctica. Ann. Glaciol., 46, 29-34. doi:10.3189/172756407782871684

Picard, G., Leduc-Leballeur, M., Banwell, A. F., Brucker, L., and Macelloni, G.: The sensitivity of satellite microwave observations to liquid water in the Antarctic snowpack, Cryosphere, 16, 5061–5083, doi:10.5194/tc-16-5061-2022, 2022.

Pollard, D., DeConto, R. M., and Alley, R. B.: Potential Antarctic Ice Sheet retreat driven by hydrofracturing and ice cliff failure, Earth and Planetary Science Letters, 412, 112–121, 2015.

Porter, C., et al.: ArcticDEM – Strips, Version 4.1, Harvard Dataverse, V1, https://doi.org/10.7910/DVN/C98DVS, [July 2024].

Rack, W., and Rott, H.: Pattern of retreat and disintegration of the Larsen B ice shelf, Antarctic Peninsula, Ann. Glaciol., 39, 505-510, 2004.

Rankl, M., Fürst, J. J., Humbert, A., and Braun, M. H.: Dynamic changes on the Wilkins Ice Shelf during the 2006–2009 retreat derived from satellite observations, The Cryosphere, 11, 1199–1211, 2017.

Raup, B.H., Racoviteanu, A., Khalsa, S.J.S., Helm, C., Armstrong, R., & Arnaud, Y.: The GLIMS Geospatial Glacier Database: a New Tool for Studying Glacier Change, Global and Planetary Change, 56, 101–110, doi:10.1016/j.gloplacha.2006.07.018, 2007.

Reed, B., Green, J. A. M., Jenkins, A., et al.: Recent irreversible retreat phase of Pine Island Glacier, Nat. Clim. Chang., 14, 75–81, doi:10.1038/s41558-023-01887-y, 2024.

Reeh, N., Thomsen, H., Higgins, A., and Weidick, A.: Sea ice and the stability of north and northeast Greenland floating glaciers. Ann. Glaciol., 33, 474-480. doi:10.3189/172756401781818554, 2001.

Reid, P.A., and R.A. Massom.: Change and variability in Antarctic coastal exposure, 1979–2020. Nat Comm, 13, 1164, https://doi.org/10.1038/s41467-022-28676-z, 2022.

Rignot, E., Casassa, G., Gogineni, P., Krabill, W., Rivera, A., and Thomas, R.: Accelerated ice discharge from the Antarctic Peninsula following the collapse of Larsen B ice shelf, Geophys. Res. Lett., 31, L18401, doi:10.1029/2004GL020697, 2004.

Robel, A.A.: Thinning sea ice weakens buttressing force of iceberg mélange and promotes calving. Nat. Comms., 8(1), 14596, doi:10.1038/ncomms14596, 2017.

Robinson, W. H. and Haskell, T. G.: Travelling flexural waves in the Erebus Glacier Tongue, McMurdo Sound, Antarctica, Cold Reg Sci Technol, 20.3, 289-293, doi:10.1016/0165-232X(92)90035-S, 1992.

Rott, H., Skvarca, P. and Nagler, T.: Rapid collapse of northern Larsen ice shelf, Antarct. Sci., 271(5250), 788-792, doi:10.1126/science.271.5250.788, 1996.

Rott, H., Rack, W., Nagler, T. and Skvarca, P.: Climatically induced retreat and collapse of northern Larsen Ice Shelf, Antarctic Peninsula, Ann. Glaciol., 27, 86-92, doi:10.3189/S0260305500017262, 1998.

Rott, H., Rack, W., Skvarca, P., and De Angelis, H.: Northern Larsen ice shelf, Antarctica: Further retreat after collapse, Ann. Glaciol., 34, 277–282, 2002.

Rott, H., Abdel Jaber, W., Wuite, J., Scheiblauer, S., Floricioiu, D., Van Wessem, J. M., Nagler, T., Miranda, N., and Van Den Broeke, M. R.: Changing pattern of ice flow and mass balance for glaciers discharging into the Larsen A and B embayments, Antarctic Peninsula, 2011 to 2016, Cryosphere, 12(4), 1273–1291. doi:10.5194/tc-12-1273-2018, 2018.

Rott, H., Wuite, J., De Rydt, J., Gudmundsson, G.H., Floricioiu, D., and Rack, W.; Impact of marine processes on flow dynamics of northern Antarctic Peninsula outlet glaciers, Nat Comms., 11:2969, doi:10.1038/s41467-020-16658-y, 2020.

Rounce, D. R., et al.: Global glacier change in the 21st century: Every increase in temperature matters, Science, 379, 78-83, doi:10.1126/science.abo1324, 2023.

Royston, S., and Gudmundsson, G. H.: Changes in ice-shelf buttressing following the collapse of Larsen A Ice Shelf, Antarctica, and the resulting impact on tributaries, J. Glaciol., 62, 905–911, 2016.

De Rydt J., Gudmundsson G. H., Rott H., and Bamber J. L.: Modeling the instantaneous response of glaciers after the collapse of the Larsen B Ice Shelf, Geophys. Res. Lett., 42(13):5355-5363, doi: 10.1002/2015GL064355, 2015.

Sakakibara, D., Sugiyama, S., Sawagaki, T., Marinsek, S., and Skvarca, P.: Rapid retreat, acceleration and thinning of Glaciar Upsala, Southern Patagonia Icefield, initiated in 2008, Annals of Glaciology, 54, 131–138, 2013.

Scambos, T., Hulbe, C., and Fahnestock, M.: Climate-induced ice shelf disintegration in the Antarctic Peninsula, in: Antarctic Peninsula Climate Variability: Historical and Paleoenvironmental Perspectives. Antarctic Research Series, 79, edited by: Domack, E., Leventer, A., Burnett, A., Bindschadler, R., Convey, P., and Kirby, M., AGU, Washington, DC, 79–92, doi:10.1029/AR079p0079, 2003.

Scambos, T. A., Bohlander, J. A., Shuman, C. A., and Skvarca, P.: Glacier acceleration and thinning after ice shelf collapse in the Larsen B embayment, Antarctica, Geophys. Res. Lett., 31, L18402, doi:10.1029/2004GL020670, 2004.

Scambos, T., R. Ross, R. Bauer, Y. Yermolin, P. Skvarca, D. Long, J. Bohlander, and T. Haran.: Calving and ice-shelf break-up processes investigated by proxy: Antarctic tabular iceberg evolution during northward drift, J. Glaciol,, 54(187), 579-591. doi:10.3189/002214308786570836, 2008.

Scambos, T., Fricker, H. A., Liu, C. C., Bohlander, J., Fastook, J., Sargent, A., Massom, R. and Wu, A. M.: Ice shelf disintegration by plate bending and hydro-fracture: Satellite observations and model results of the 2008 Wilkins ice shelf break-ups. Earth Planet. Sci. Lett., 280(1-4), 51-60. doi:10.1016/j.epsl.2008.12.027, 2009.

Scambos, T. A., Berthier, E., and Shuman, C. A.: The triggering of subglacial lake drainage during rapid glacier drawdown: Crane Glacier, Antarctic Peninsula, The Cryosphere, 5, 74–82, 2011.

Scambos, T.A., Ross, R., Haran, T., Bauer, R., Ainley, D.G., Seo, K.W., De Keyser, M., Behar, A. and MacAyeal, D.R.: A camera and multisensor automated station design for polar physical and biological systems monitoring: AMIGOS. J. Glaciol., 59(214). doi:10.3189/2013JoG12J170. 2013.

Scambos, T., Moussavi, M. S., Abdalati, W. and Pettit, E. C.: December. Evolution of fast ice thickness from Cryosat-2 radar altimetry data, a case study in Scar Inlet, Antarctica. AGU Fall Meeting Abstracts (Vol. 2017, pp. C21G-1181), 2017.

Scambos, T., Berthier, E., Haran, T., Shuman, C., Cook, A., Ligtenberg, S., and Bohlander, J.: Detailed ice loss pattern in the northern Antarctic Peninsula: widespread decline driven by ice front retreats, The Cryosphere, 8, 2135–2145, 2014.

Scambos, T. A., Bell, R. E., Alley, R. B., Anandakrishnan, S., Bromwich, D. H., Brunt, K., et al.: How much, how fast?: A science review and outlook for research on the instability of Antarctica's Thwaites Glacier in the 21st century, Global Planet. Change, 153, 16-34, 2017.

Schoof, C.: Ice sheet grounding line dynamics: Steady states, stability, and hysteresis, J. Geophys. Res.: Earth Surf., 112(F3), 2007.

Schoof, C.: Marine ice sheet stability, J. Fluid Mech., 698, 62–72, 2012.

Seehaus, T. C., Sommer, C., Dethinne, T., and Malz, P.: Mass changes of the northern Antarctic Peninsula Ice Sheet derived from repeat bi-static SAR acquisitions for the period 2013–2017, The Cryosphere Discuss. [preprint], doi:10.5194/tc-2022-251, in review, 2023.

Sergeant, A., Mangeney, A., Yastrebov, V. A., Walter, F., Montagner, J.-P., Castelnau, O., Stutzmann, E., Bonnet, P., Ralaiarisoa, V. J.-L., and Bevan, S.: Monitoring Greenland ice sheet buoyancy-driven calving discharge using glacial earthquakes, Annals of Glaciology, 60, 75–95, 2019.

Sergienko, O. V.: No general stability conditions for marine ice-sheet grounding lines in the presence of feedbacks, Nat. Commun., 13, 2265, doi:10.1038/s41467-022-29892-3, 2022.

Shields, C. A., Wille, J. D., Marquardt Collow, A. B., Maclennan, M., and Gorodetskaya, I. V.: Evaluating uncertainty and modes of variability for Antarctic atmospheric rivers. Geophys. Res. Lett., 49, e2022GL099577. doi:10.1029/2022GL099577, 2022.

Shuman C. A., Berthier E., and Scambos T. A.: 2001-2009 Elevation and mass losses in the Larsen A and B embayments, Antarctic Peninsula, J. Glaciol., 57(204):737-754. doi:10.3189/002214311797409811, 2011.

Shuman, C., Scambos, T. and Berthier, E.: Ice loss processes in the Seal Nunataks ice shelf region from satellite altimetry and imagery. Ann. Glaciol, 57(73), 94-104, doi:10.1017/aog.2016.29, 2016.

Skvarca, P., Rack, W., Rott, H. and Donángelo, T. I.: Climatic trend and the retreat and disintegration of ice shelves on the Antarctic Peninsula: an overview, Polar Res, 18(2), 151-157, doi:10.1111/j.1751-8369.1999.tb00287, 1999.

Smith, B., Fricker, H.A., Gardner, A.S., Medley, B., Nilsson, J., Paolo, F.S., Holschuh, N., Adusumilli, S., Brunt, K., Csatho, B. and Harbeck, K.: Pervasive ice sheet mass loss reflects competing ocean and atmosphere processes. Science, 368(6496), 239-1242, doi:10.1126/science.aaz5845, 2020.

Smith, B., S. Adusumilli, B. M. Csathó, D. Felikson, H. A. Fricker, A. Gardner, N. Holschuh, J. Lee, J. Nilsson, F. S. Paolo, M. R. Siegfried, T. Sutterley, and the ICESat-2 Science Team: ATLAS/ICESat-2 L3A Land Ice Height, Version 5,. Boulder, Colorado USA. NASA National Snow and Ice Data Center Distributed Active Archive Center. doi:10.5067/ATLAS/ATL06.005. Date Accessed 09-12-2022, 2021.

Spreen, G., Kaleschke, L., and Heygster, G.: Sea ice remote sensing using AMSR-E 89 GHz channels, J. Geophys. Res., 113, C02S03, doi:10.1029/2005JC003384, 2008.

Squire, V.A.,: Of ocean waves and sea-ice revisited. Cold Regions Science and Technology, 49(2), 110, https://doi.org/10.1016/j.coldregions.2007.04.007. 2007.

Streiff-Becker, R.: Probleme der Firnschichtung, Zeitschrift für Gletscherkunde und Glazialgeologie, 2, 1–9, 1952.

Sulak, D. J., Sutherland, D. A., Enderlin, E. M., Stearns, L. A., and Hamilton, G. S.: Iceberg properties and distributions in three Greenlandic fjords using satellite imagery, Annals of Glaciology, 58, 92–106, 2017.

Sun, Y., Riel, B., and Minchew, B.: Disintegration and buttressing effect of the landfast sea ice in the Larsen B embayment, Antarctic Peninsula. Geo. Res. Lett, 50, e2023GL104066. https://doi.org/10.1029/2023GL104066, 2023.

Surawy-Stepney, T., Hogg, A. E., Cornford, S. L., Wallis, B. J.: The impact of landfast sea ice buttressing on ice dynamic speedup in the Larsen-B Embayment, Antarctica, The Cryosphere Discuss. [preprint], https://doi.org/10.5194/tc-2023-128, in review, 2023.

Teder, N. J., Bennetts, L. G., Reid, P. A., and Massom, R. A.: Sea ice-free corridors for large swell to reach Antarctic ice shelves. Environ. Res. Lett., 17(4), 045026, doi:10.1088/1748-9326/ac5edd, 2022.

Teder, N. J., Bennetts, L. G., Reid, P. A., Massom, R. A., Pitt, J. P. A., Scambos, T. A., and Fraser, A. D.: Catastrophic ice shelf calving events follow prolonged amplified flexural strain, Nature Geoscience, in review, 2024.

Torinesi, O., Fily, M., and Genthon, C.: Variability and Trends of the Summer Melt Period of Antarctic Ice Margins since 1980 from Microwave Sensors. J. Climate, 16, 1047–1060, doi:10.1175/1520-0442(2003)016<1047:VATOTS>2.0.CO;2, 2003.

Tuckett, P. A., Ely, J. C., Sole, A. J., Livingstone, S. J., Davison, B. J., and van Wessem, J. M.: Reply to: "Impact of marine processes on flow dynamics of northern Antarctic Peninsula outlet glaciers" by Rott et al., Nature Communications, 11, 2970, 2020.

Turner, J., Lu, H., White, I., King, J. C., Phillips, T., Hosking, J. S., Bracegirdle, T. J., Marshall, G. J., Mulvaney, R. and Deb, P.: Absence of 21st century warming on Antarctic Peninsula consistent with natural variability, Nature, 535, 411–415. doi:10.1038/nature18645, 2016.

Turner, J., Holmes, C., Caton Harrison, T., Phillips, T., Jena, B., Reeves-Francois, T., et al.: Record low Antarctic sea ice cover in February 2022. Geophys. Res. Lett., 49, e2022GL098904. doi:10.1029/2022GL098904, 2022.

Vaughan, D. G.: Investigating tidal flexure on an ice shelf using kinematic GPS, Annals of Glaciology, 20, 372–376, 1994.

Vincent, C., Dumont, M., Six, D., Brun, F., Picard, G., & Arnaud, L.: Why do the dark and light ogives of Forbes bands have similar surface mass balances? Journal of Glaciology, 64(244), 236–246, doi:10.1017/jog.2018.12, 2018.

Voytenko, D., Stern, A., Holland, D. M., Dixon, T. H., Christianson, K., and Walker, R. T.: Tidally driven ice speed variation at Helheim Glacier, Greenland, observed with terrestrial radar interferometry, Journal of Glaciology, 61, 301–308, 2015.

Waddington, E.: Wave ogives, Journal of Glaciology, 32.112, 325–334, https://doi.org/10.3189/S0022143000011990, 1986.

Wallis, B. J., Hogg, A. E., Zhu, Y., and Hooper, A.: Change in grounding line location on the Antarctic Peninsula measured using a tidal motion offset correlation method, EGUsphere, 2024, 1–32, 2024.

Walker, R. T., Christianson, K., Parizek, B. R., Anandakrishnan, S., and Alley, R. B.: A viscoelastic flowline model applied to tidal forcing of Bindschadler Ice Stream, West Antarctica, Earth and Planetary Science Letters, 319, 128–132, 2012.

Walter, F., Amundson, J. M., O'Neel, S., Truffer, M., Fahnestock, M., and Fricker, H. A.: Analysis of low-frequency seismic signals generated during a multiple-iceberg calving event at Jakobshavn Isbræ, Greenland, Journal of Geophysical Research: Earth Surface, 117, 2012.

Warren, C. R., Greene, D. R., and Glasser, N. F.: Glaciar Upsala, Patagonia: rapid calving retreat in fresh water, Annals of Glaciology, 21, 311–316, 1995.

Van Wessem, J. M., Reijmer, C. H., Van De Berg, W. J., van Den Broeke, M. R., Cook, A. J., Van Ulft, L. H. and Van Meijgaard, E.: Temperature and wind climate of the Antarctic Peninsula as simulated by a high-resolution Regional Atmospheric Climate Model. J. Clim., 28(18), 7306–7326. doi:10.1175/JCLI-D-15-0060.1, 2015.

Wellner, J.S., Scambos, T., Domack, E.W., Vernet, M., Leventer, A., Balco, G., Brachfeld, S., Cape, M.R., Huber, B., Ishman, S. and McCormick, M.L.: The Larsen ice shelf system, Antarctica (LARISSA): Polar systems bound together, changing fast. GSA Today, 29(8). doi:10.1130/GSATG382A.1, 2019

White, A., Copland, L., Mueller, D., and Van Wychen, W.: Assessment of historical changes (1959-2012) and the causes of recent break-ups of the Petersen ice shelf, Nunavut, Canada. Ann. Glaciol., 56(69), 65-76. doi:10.3189/2015AoG69A687, 2015.

Wille, J. D., Favier, V., Dufour, A., Gorodetskaya, I. V., Turner, J., Agosta, C., and Codron, F.: West Antarctic surface melt triggered by atmospheric rivers. Nat. Geosci. 12, 911–916, https://doi.org/10.1038/s41561-019-0460-1, 2019.

Wille, J. D., Favier, V., Gorodetskaya, I. V., Agosta, C., Kittel, C., Beeman, J. C., Jourdain, N. C., Lenaerts, J. T. M., and Codron, F.: Antarctic atmospheric river climatology and precipitation impacts. J. Geophys. Atmos., 126, e2020JD033788. doi:10.1029/2020JD033788, 2021.

Wille, J. D., Favier, V., Jourdain, N. C., Kittel, C., et al.: Intense atmospheric rivers can weaken ice shelf stability at the Antarctic Peninsula. Nat. Commun Earth & Environ, 3(1), doi:10.1038/s43247-022-00422-9, 2022.

Winberry, J. P., Huerta, A. D., Anandakrishnan, S., Aster, R. C., Nyblade, A. A., and Wiens, D. A.: Glacial earthquakes and precursory seismicity associated with Thwaites Glacier calving, Geophysical Research Letters, 47, e2019GL086178, 2020.

Wuite, J., Rott, H., Hetzenecker, M., Floricioiu, D., De Rydt, J., Gudmundsson, G. H., Nagler, T., and Kern, M.: Evolution of surface velocities and ice discharge of Larsen B outlet glaciers from 1995 to 2013, Cryosphere, 9, 957–969, doi:10.5194/tc-9-957-2015, 2015.

Young, N., Turner, D., Hyland, G., and Williams, R.: Near-coastal iceberg distributions in East Antarctica, 50-145° E. Ann. Glaciol, 27, 68-74. doi:10.3189/1998AoG27-1-68-74, 1998.

Zagorodnov, V., Nagornov, O., Scambos, T.A., Muto, A., Mosley-Thompson, E., Pettit, E.C. and Tyuflin, S.: Borehole temperatures reveal details of 20th century warming at Bruce Plateau, Antarctic Peninsula. Cryosphere, 6(3), 675-686, doi: 10.5194/tc-6-675-2012, 2012.

APPENDIX I

Supplementary Material for Chapter 1, as published in The Cryosphere.

Table 1: DEMs from Worldview Imagery			
Sensor	Acquisition Date	Sensor	Acquisition Date
WV2	3/9/17	WV3	4/21/21
WV2	4/18/17	WV3	1/15/22
WV1	4/22/17	WV2	2/14/22
WV2	11/27/17	WV3	2/19/22
WV2	3/26/18	WV2	10/3/22
WV2	9/30/18	WV3	11/21/22
WV3	2/9/20	WV3	12/25/22
WV2	3/22/21	WV2	2/16/23

Table A1-S1: Date and sensor of Worldview images used for this study.

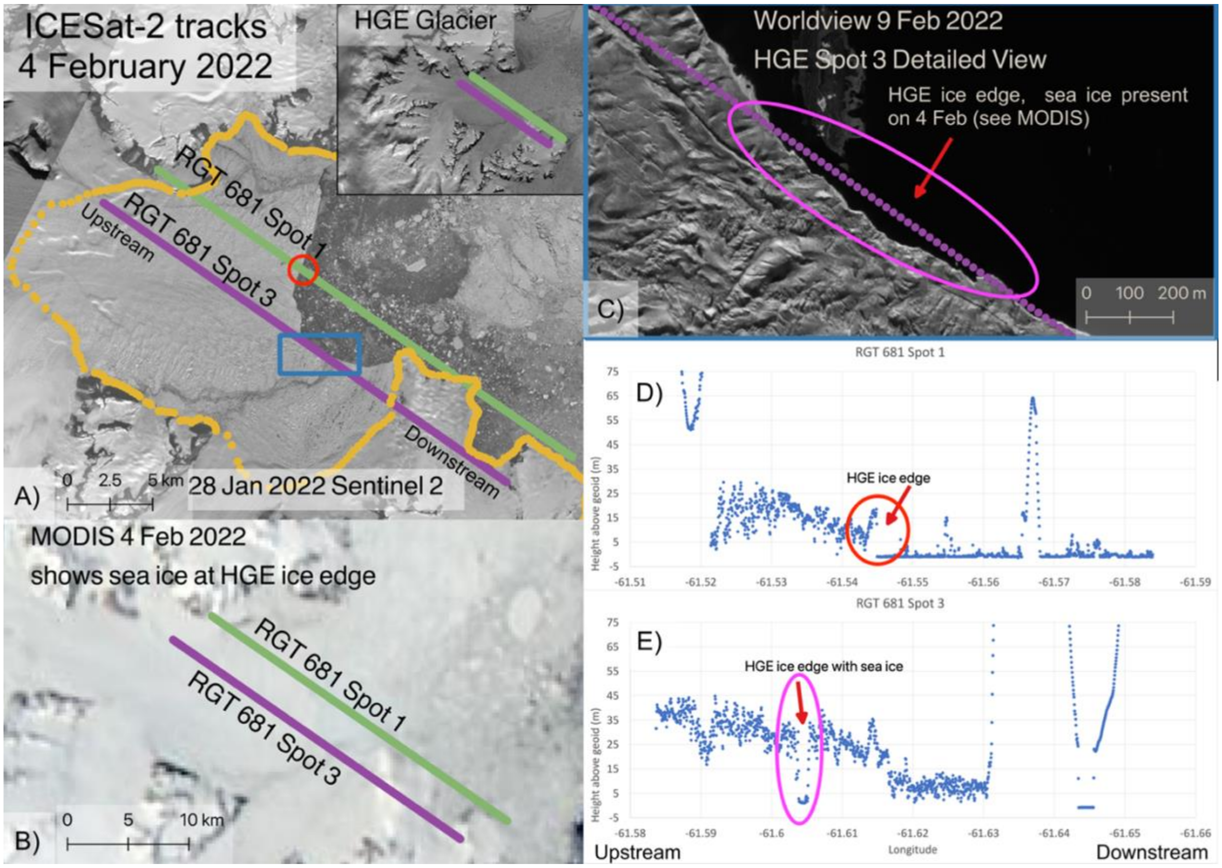

Figure A1-S1: ICESat-2 data showing the freeboard elevation of the outer edge of the HGE floating tongue. A) 28 January 2022 ice edge during a period of open water at the front. B) MODIS image from 4 February 2022, the same day that the ICESat-2 data was acquired, shows sea ice in the embayment during the time the elevation data was collected. C) Worldview image from 9 February 2022 shows a detailed view (blue box on Panel A) of the ICESat 2 Spot 3 track. D) Elevation data collected on 4 February of Spot 1 ICESat-2 track (green), showing the ice edge near the center of the HGE floating front (red circle, red arrow). E) ICESat-2 Spot 3 track (purple track), where an ice edge is present for a small portion of the track (Panel C, pink circles).

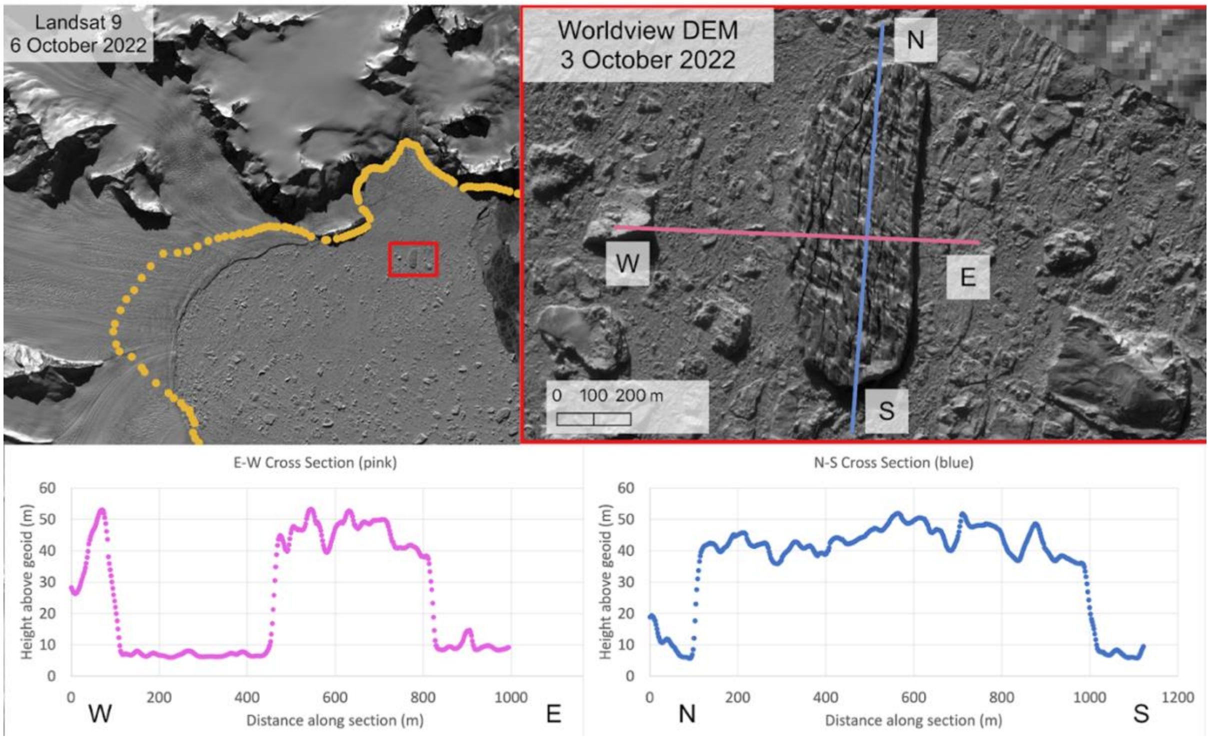

Figure A1-S2: Worldview DEMs from October 2022 show the freeboard of tabular bergs calved from the HGE ice tongue, note that north is Grid North in ESPG: 3031.

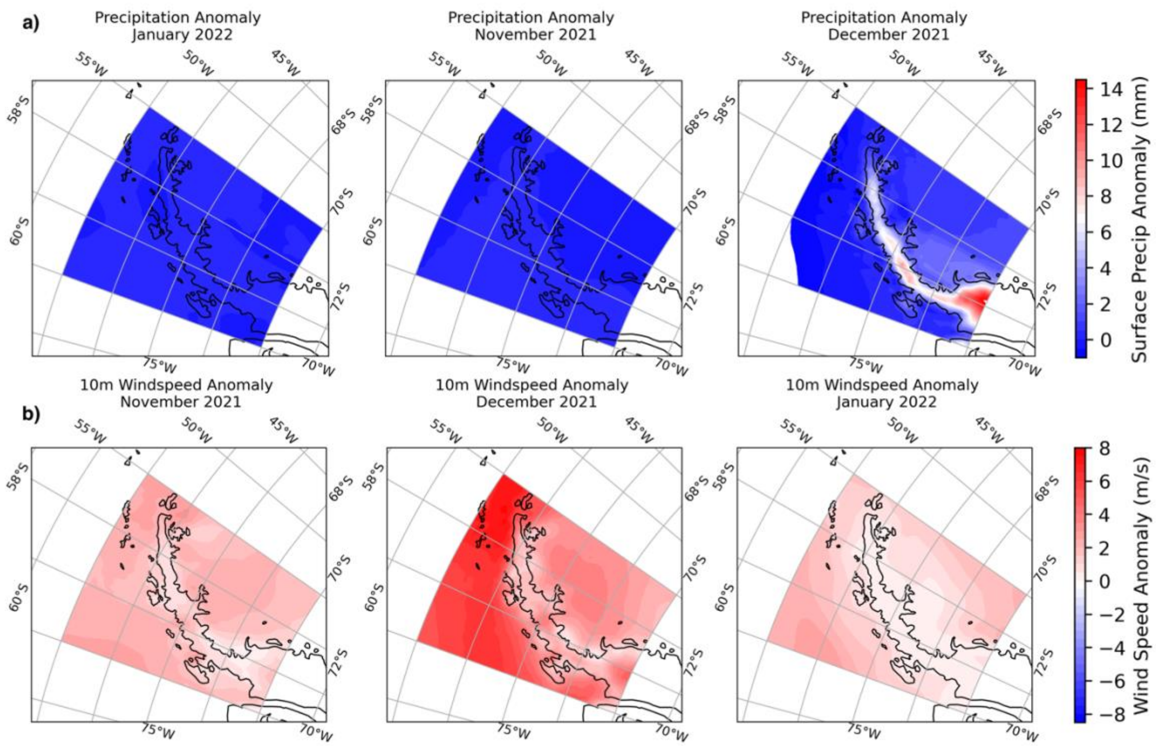

Figure A1-S3: Precipitation and windspeed anomalies (1979-2022) for the AP region in November 2021, December 2021, and January 2022.

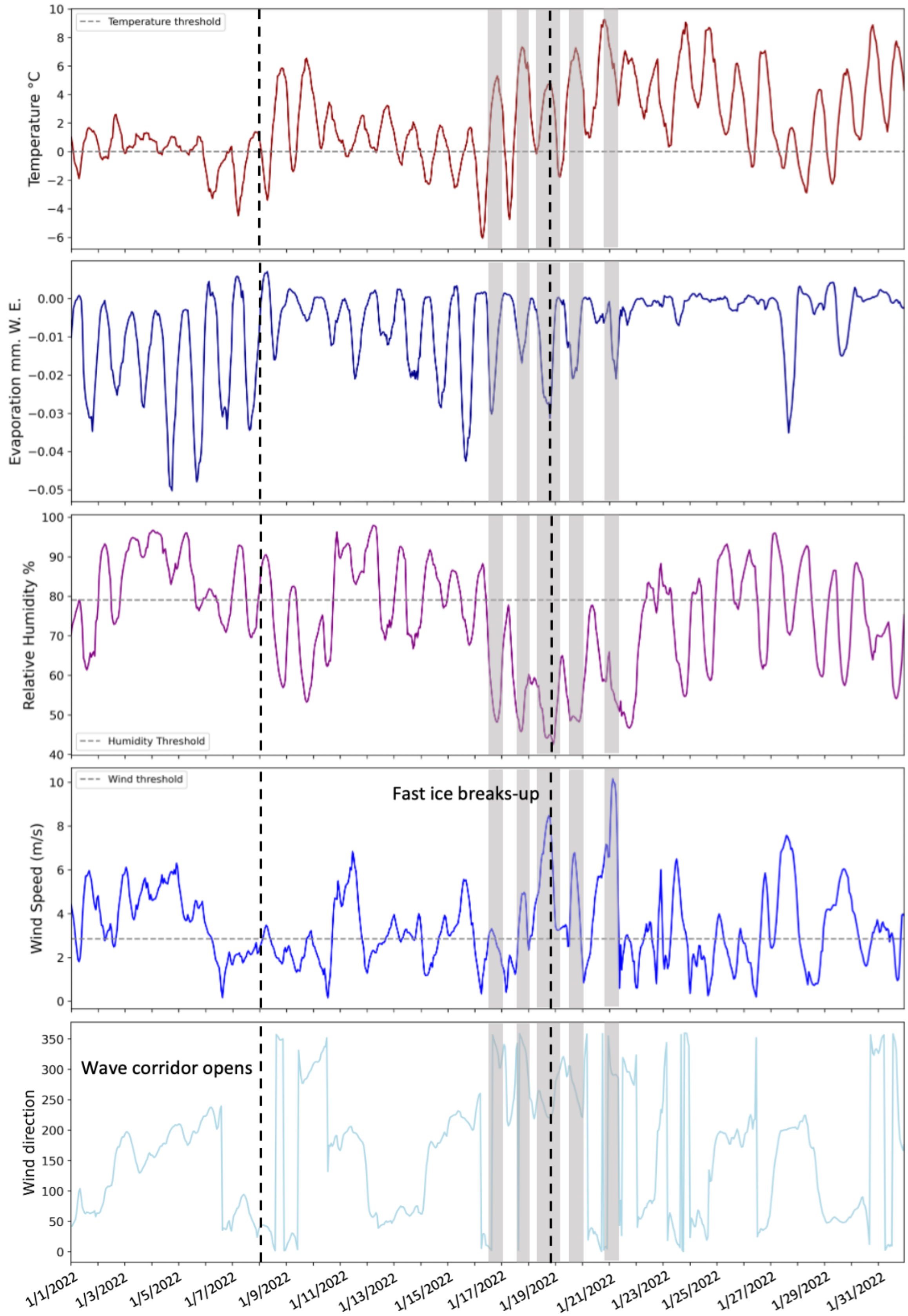

Temperature threshold
Temperature °C
Evaporation mm. W. E.
Relative Humidity %
Humidity Threshold
Wind threshold
Fast ice breaks-up
Wind Speed (m/s)
Wave corridor opens
Wind direction
1/1/2022
1/3/2022
1/5/2022
1/7/2022
1/9/2022
1/11/2022
1/13/2022
1/15/2022
1/17/2022
1/19/2022
1/21/2022
1/23/2022
1/25/2022
1/27/2022
1/29/2022
1/31/2022

Figure A1-S4: ERA-5 climate variables on hourly time scale during January 2022. The horizontal dashed lines indicate foehn wind thresholds determined by Laffin et al., 2022. The vertical dashed lines show the when the wave corridor opened and when the fast ice broke-up. The gray shaded lines indicate periods when all of the foehn wind thresholds were met, suggesting times of foehn wind events.

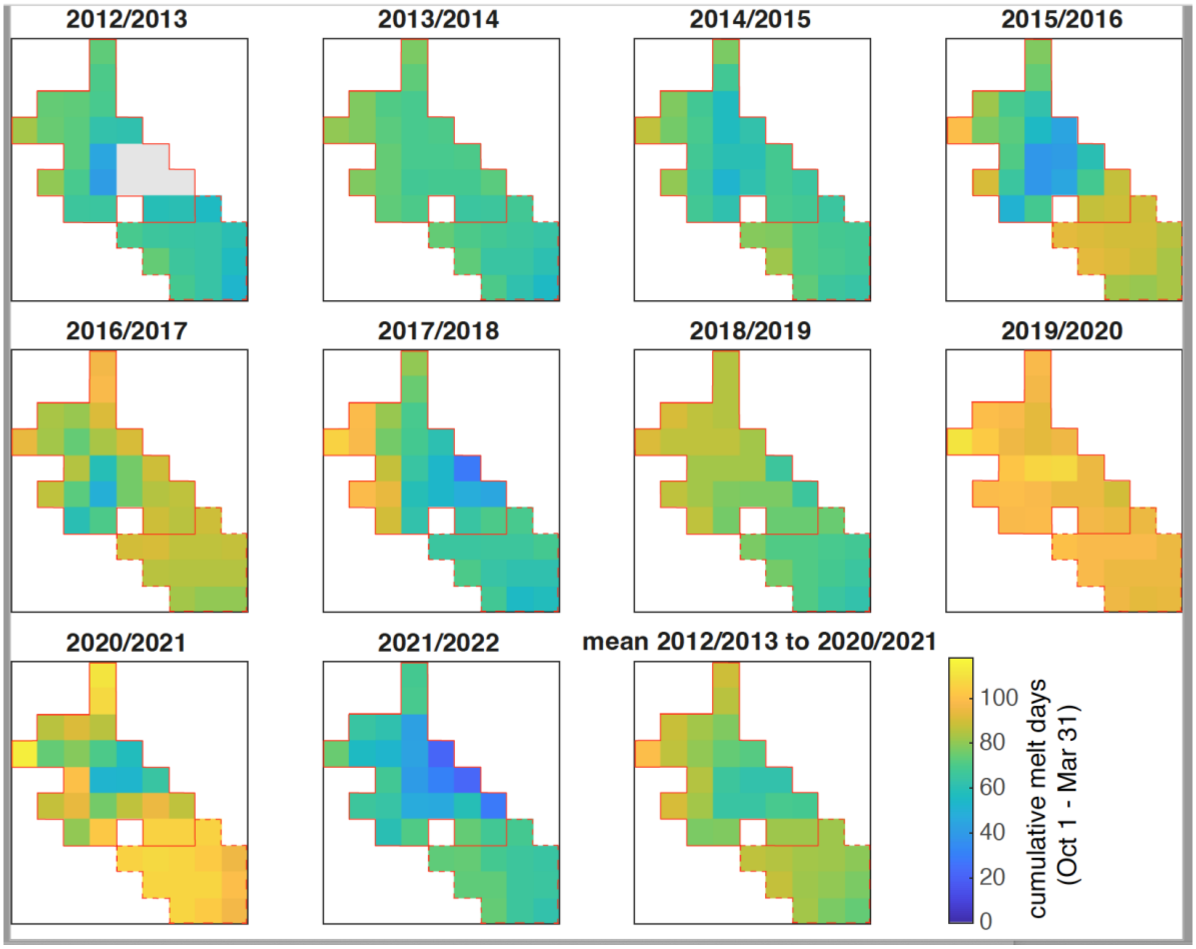

Figure A1-S5: Cumulative melt day maps from 2012/2013 to 2020/2021 for the Larsen B embayment (solid lines) and Scar Inlet Ice Shelf (dashed lines).

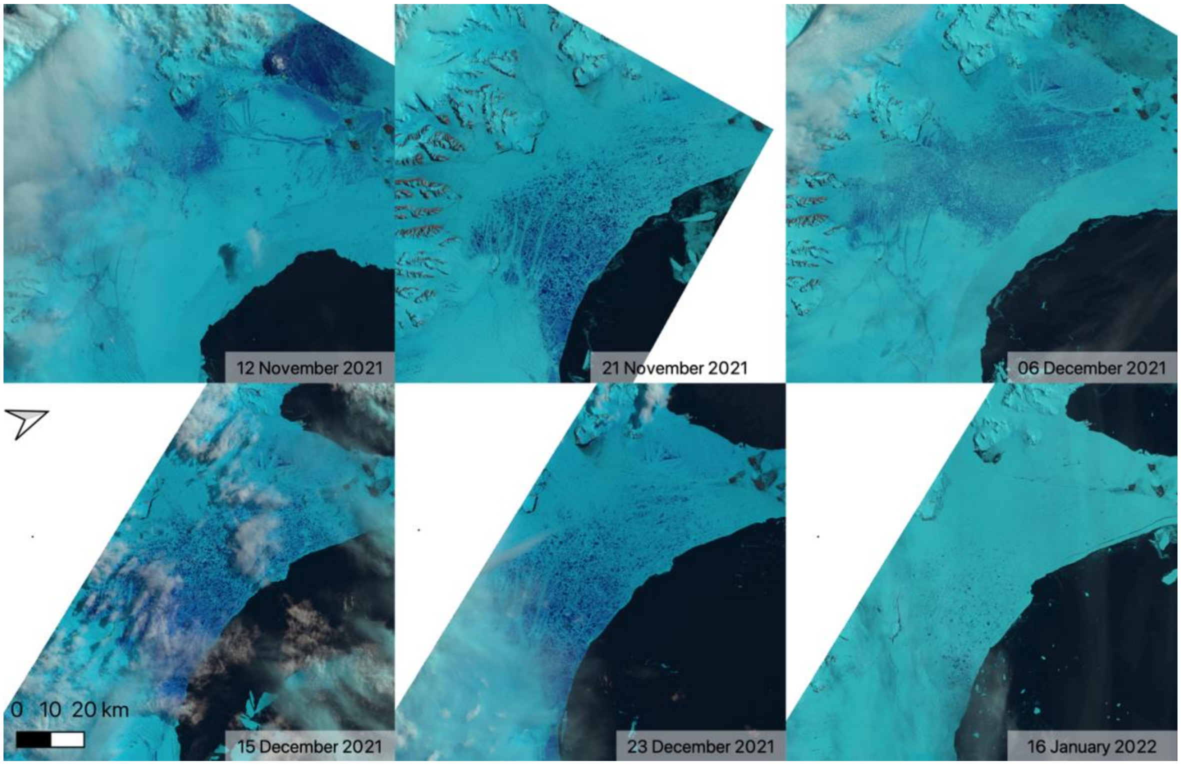

Figure A1-S6: Melt pond evolution using Landsat imagery from November 2021 to January 2022.

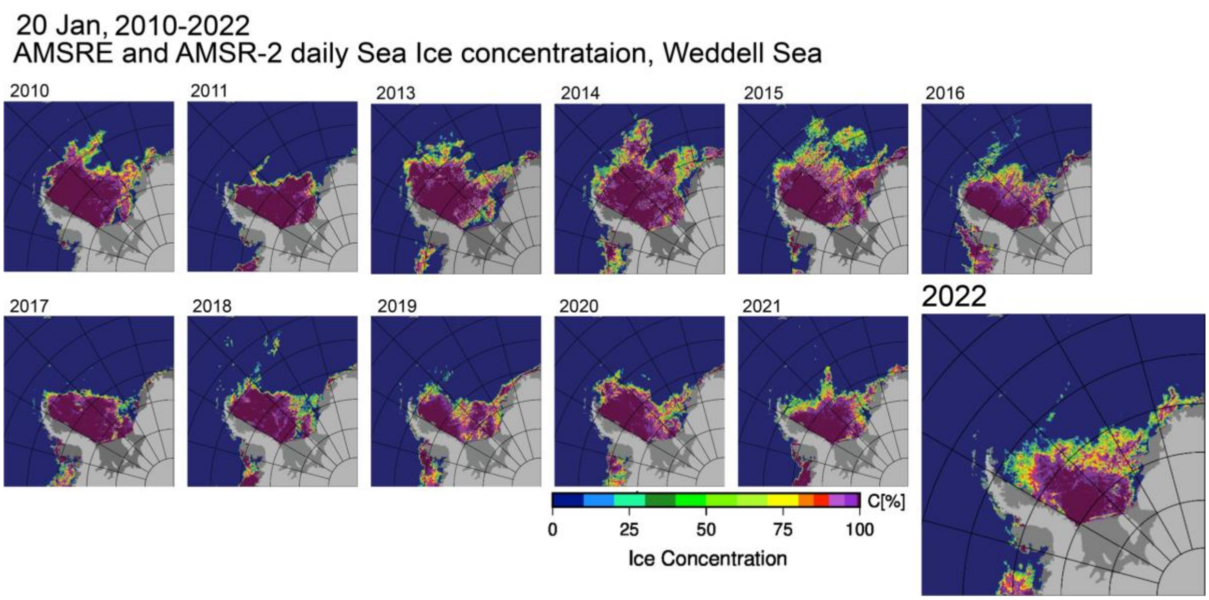

Figure A1-S7: Sea ice concentration in Weddell Sea on 20 January from 2010 to 2011 and 2013 to 2022. The open corridor was not present in any of the previous seasons on record during this time of year.

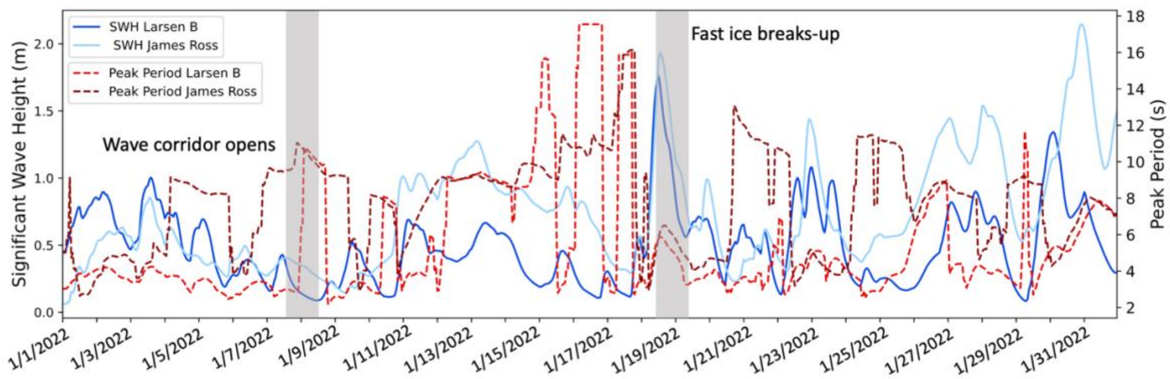

Figure A1-S8: We obtain ocean wave-field data from the WaveWatch III model hindcast from the Collaboration for Australian Weather and Climate Research (CAWCR; Wave Hindcast Aggregated Collection; Durrant et al., 2019). From June 2013 onwards the dataset is generated using WaveWatch III v4.18 wave model forced with NCEP CFSv2 hourly winds and daily sea ice producing gridded spectral wave data on a global 0.4 (24 arcminute) grid. Here we examine an hourly time series of the variables for January 2022, averaging over four grid cells in front of the Larsen B embayment and near the James Ross Island, where a wave corridor was present.

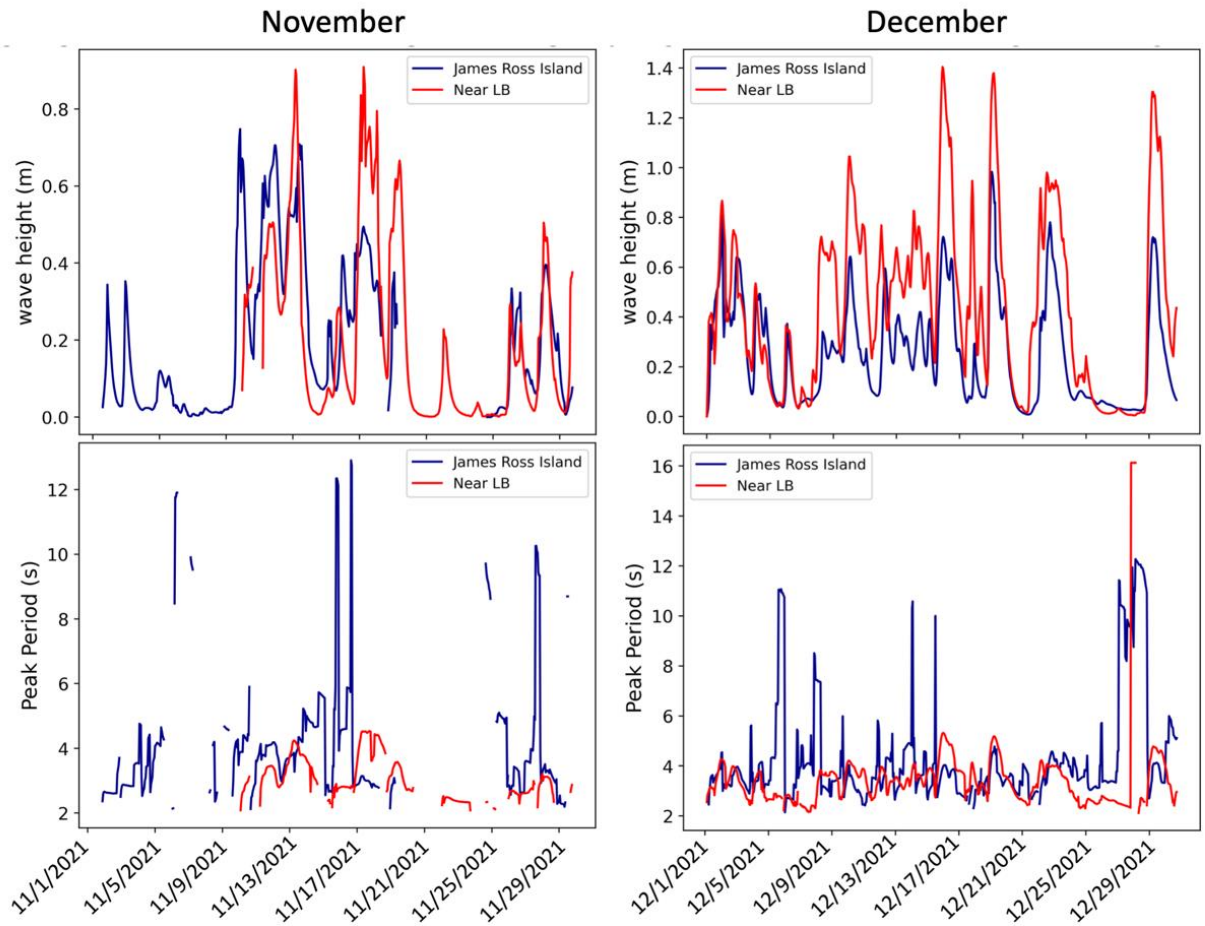

Figure A1-S9: Wavewatch wave data showing the peak period and significant wave height for November and December 2021 for locations near James Ross Island and in front of the Larsen B embayment.

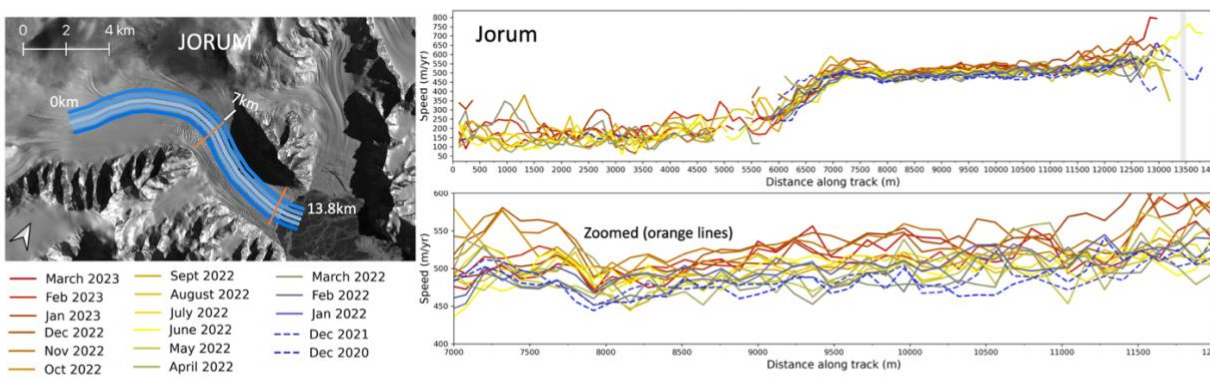

Figure A1-S10: Jorum Glacier speeds derived from the ASF Vertex Tool and Hyp3 pipeline using Sentinel 1 imagery from December 2020 to March 2023.

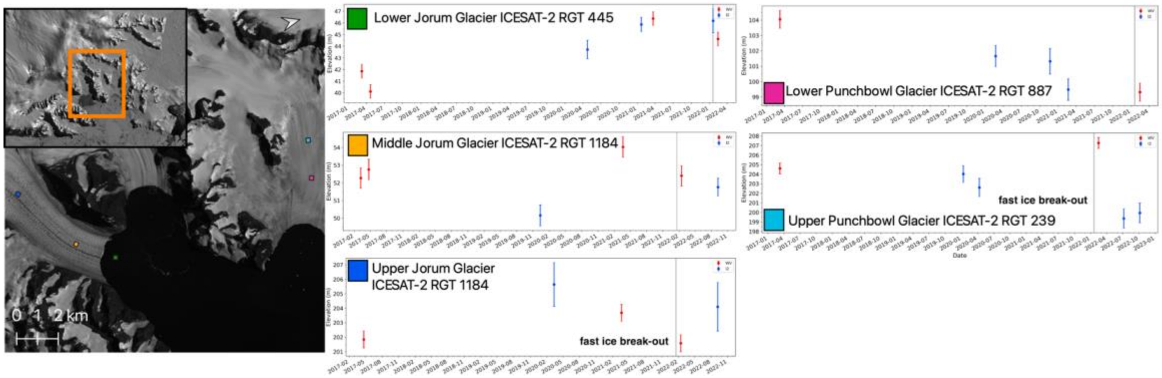

Figure A1-S11: Jorum and Punchbowl elevation changes from ICEsat and Worldview DEMs.

Supplemental Video 1

Evolution of Larsen B embayment from 2012 to 2022 from MODIS imagery.

https://doi.org/10.5446/66845 (Ochwat, 2024).

References:

Durrant, T., Hemer, M., Smith, G., Trenham, C., Greenslade, D.: CAWCR Wave Hindcast - Aggregated Collection. v5. CSIRO. Service Collection. http://hdl.handle.net/102.100.100/137152?index=1, 2019.

Ochwat, Naomi: NASA MODIS imagery time series. Copernicus Publications, 2024. https://doi.org/10.5446/66845

APPENDIX II

Supplementary Material for Chapter 2 for submission in Nature Geoscience.

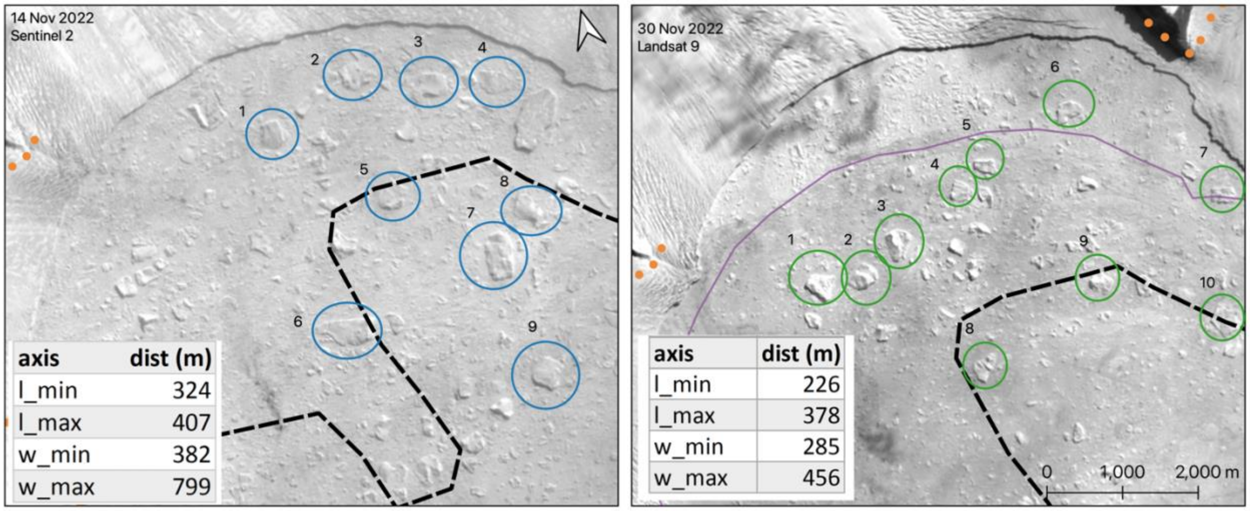

Figure A2-S1: Iceberg distribution size during two episodes of retreat. The black dashed line is the 2021 grounding zone. In Panel A nine icebergs were measured along the primary axes three times and averaged. The maximum length is the minimum ice thickness, which is ~407 m. In Panel B the purple line is the previous ice front (Panel A ice extent) and ten icebergs were measured, showing a minimum ice thickness of ~378 m.

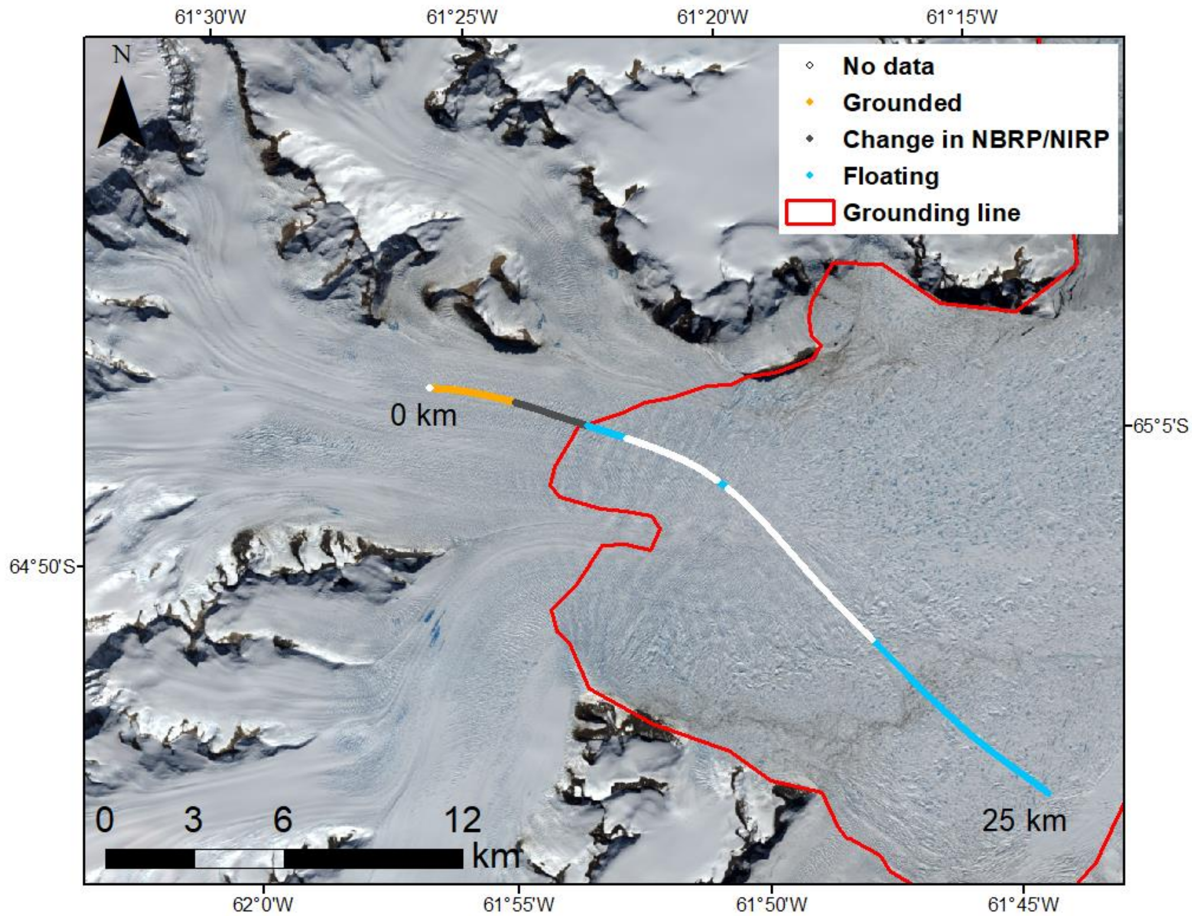

Figure A2-S2: Map of IceBridge dataset acquired over Hektoria Glacier on October 31, 2017 overlying a true-color Landsat-8 optical image acquired on 13 September December 3, 2017. The dataset is classified based on the signal analysis in Figure S3. The red contour is Ochwat et al., (2024) grounding line.

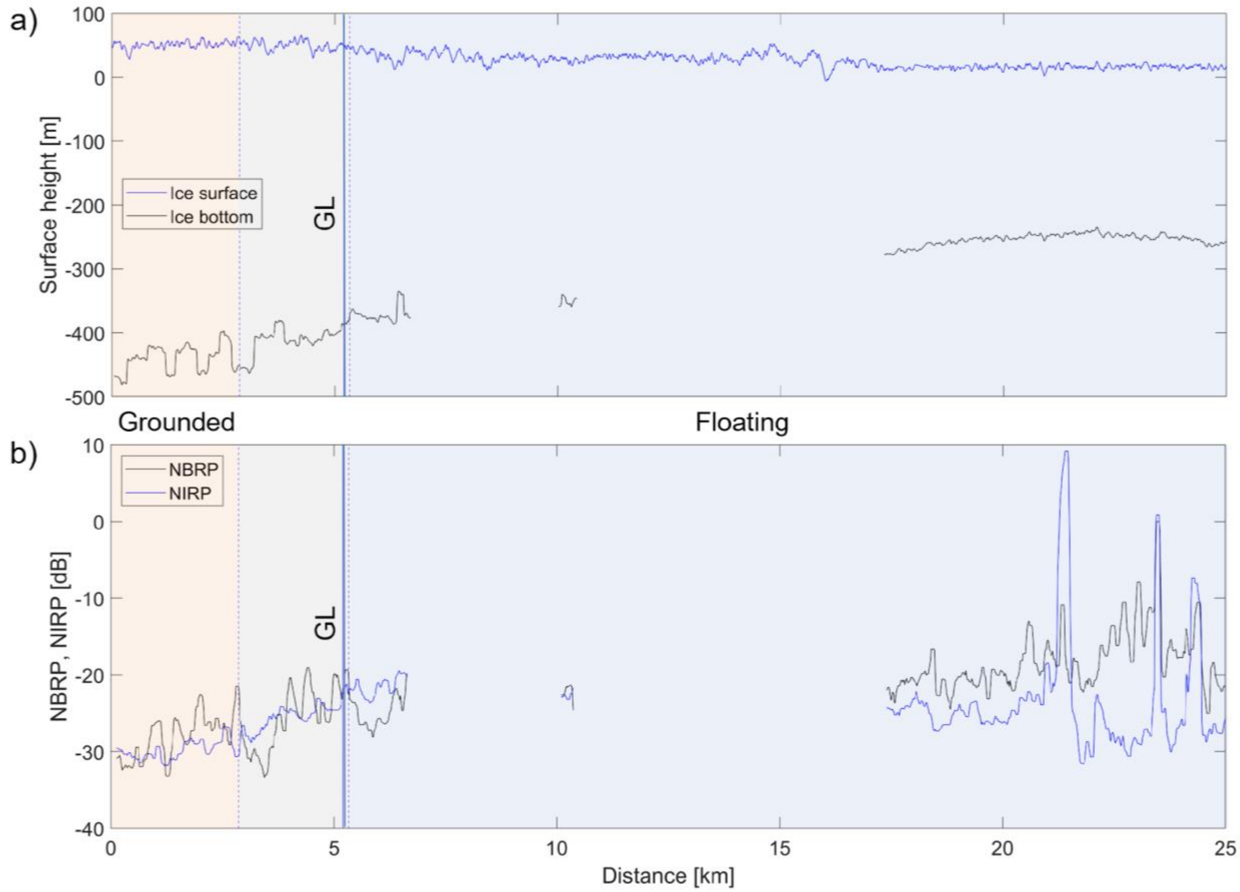

Figure A2-S3: IceBridge data over Hektoria Glacier. a) Ice surface and bottom heights; b) Normalized Bed Reflection Power (NBRP) and Normalized Internal Reflection Power (NIRP). The grounded part of the glacier is highlighted by light orange color, the floating ice is highlighted by blue color, and the region where both NBRP and NIRP values start to increase is highlighted by gray colors. This region is likely associated with the transition of the glacier from grounded to floating, however the bed signal in this zone is obscured by high internal reflection (NIRP > NBRP) associated with the crevasses clearly seen in the Landsat-8 images (Fig. A2-S2).

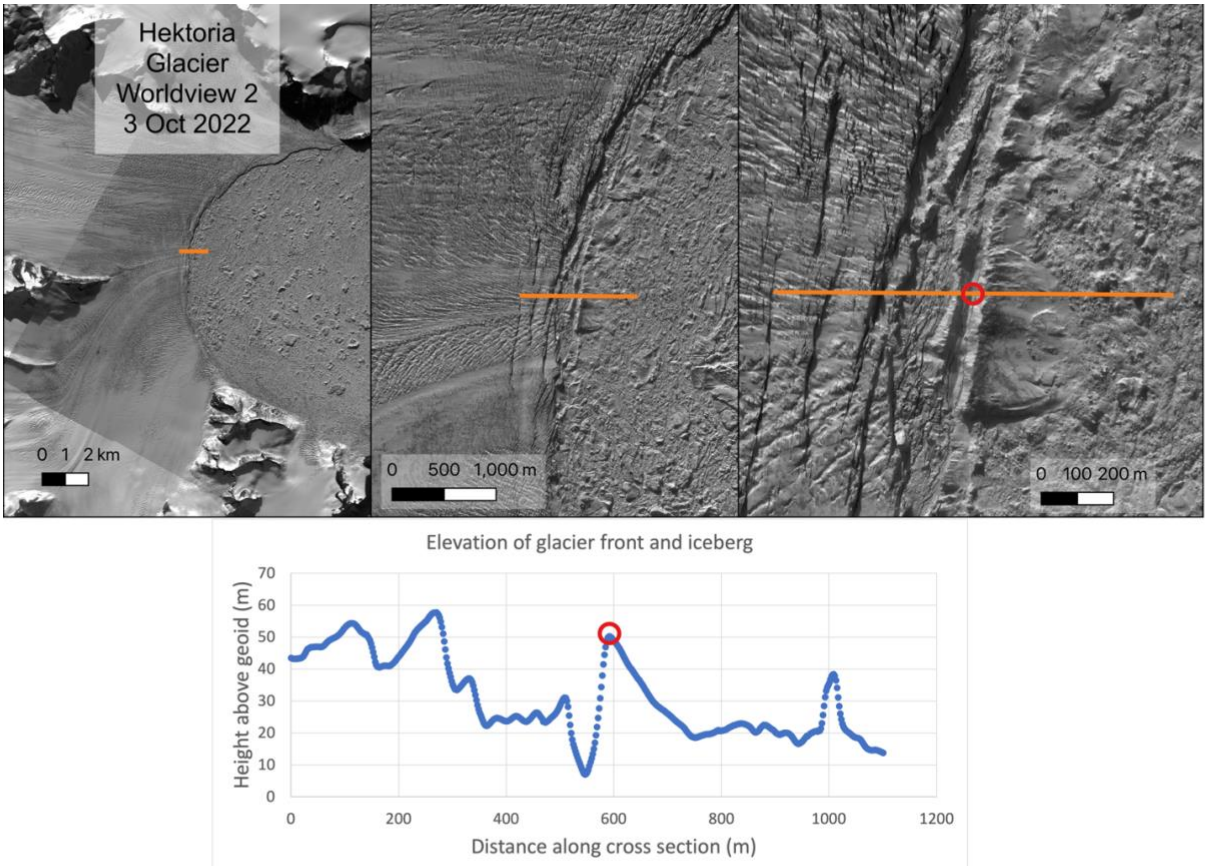

Figure A2-S4: Worldview 2 orthoimage and DEM that show the terminus of Hektoria Glacier on 3 October 2022, prior to the initiation of the rapid calving period. The terminus has a ~50 m high cliff front and displays slumping and rifting upstream of the terminus. The iceberg at the front is clearly rotated "toes-out" indicating it was calved via buoyancy-driven processes.

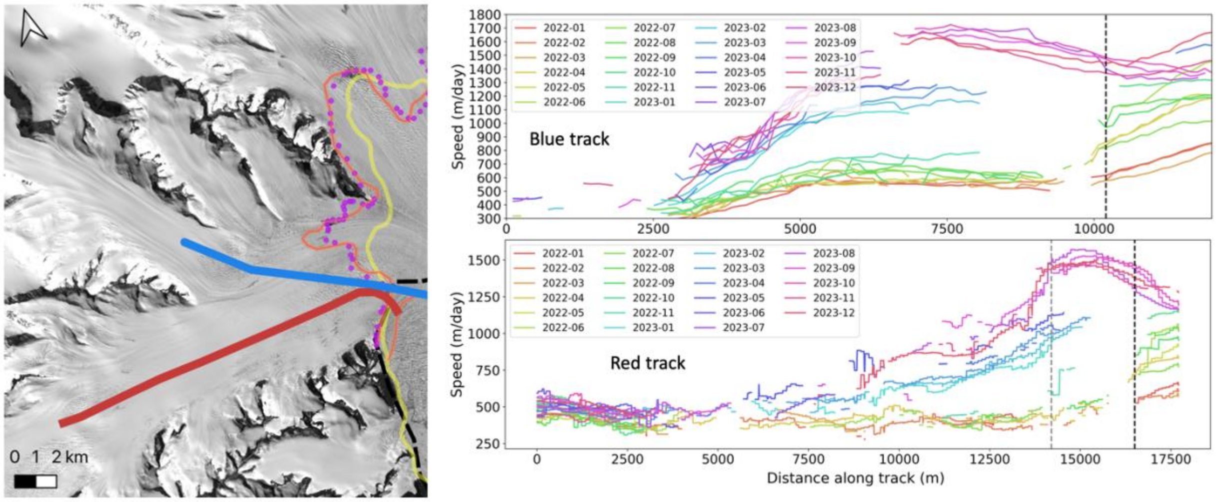

Figure A2-S5: Green Glacier velocity from January 2022 to December 2023. Upper panel depicts the along-flow profile (red line) and the lower panel depicts the Icebridge ATM track profile in order to compare the speeds to those presented in Ochwat et al., (2024).

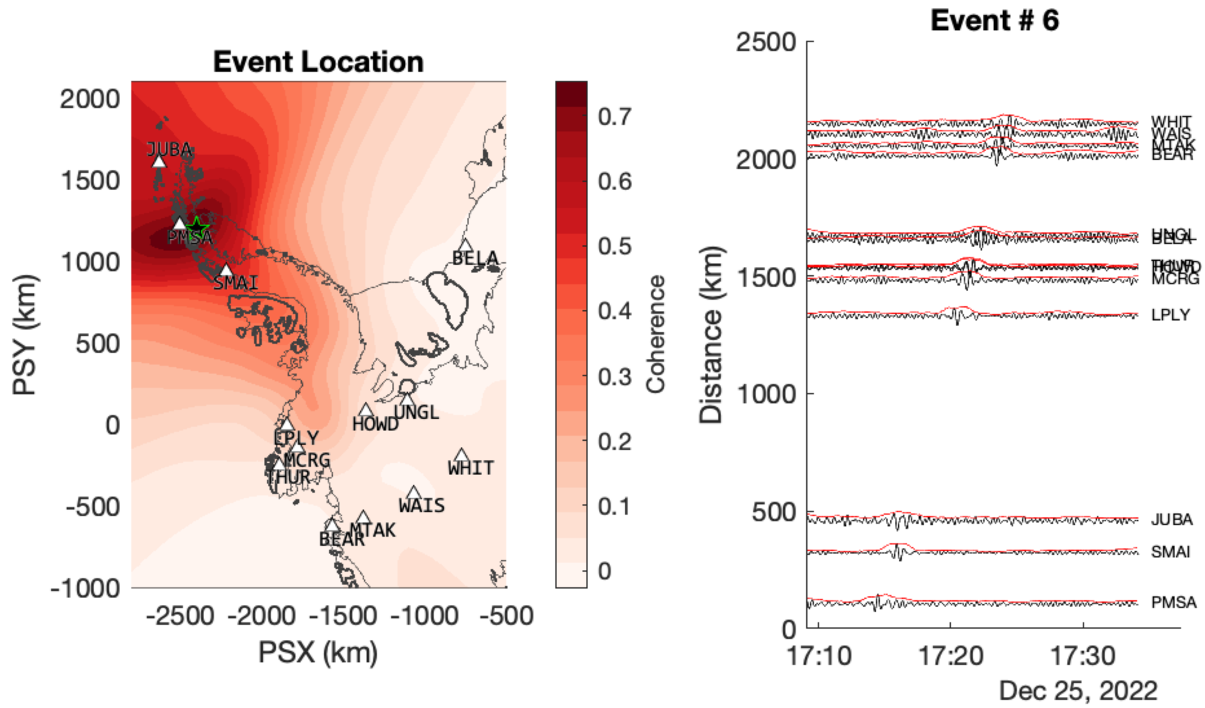

Figure A2-S6: Example glacial earthquake location and waveforms. Glacier earthquakes are identified on 5 separate days that correspond to periods of rapid retreat. As noted in previous studies (i.e. 48), the relatively long-wavelength seismic waves (~100 km for 30 s Rayeleigh waves) generated by glacial earthquakes and the sparse station coverage results in relatively large uncertainties (~50 km) in event location. Thus, while uncertainty remains, the occurrence of these events during the time period of Hektoria glacier's rapid retreat make Hektoria glacier the most plausible source of these events.

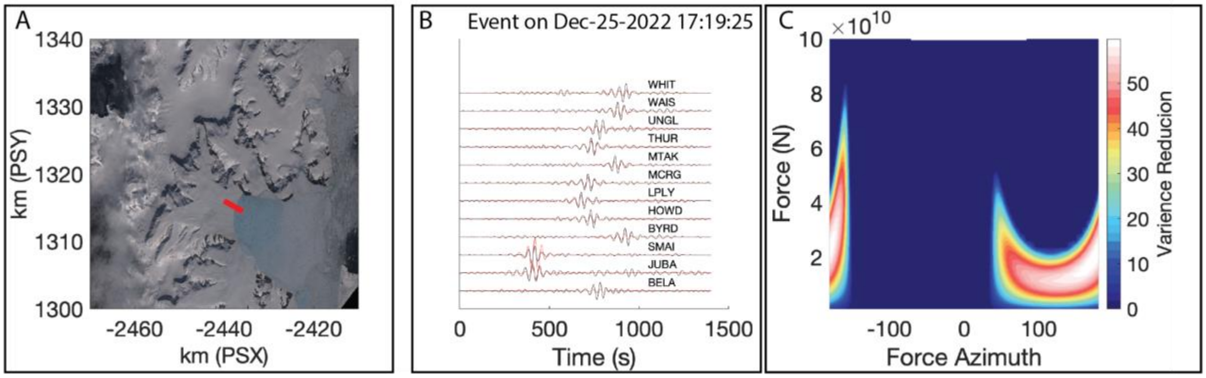

Figure A2-S7: Example of waveform modeling for Dec 25, 2022 Event; A) Landsat image from December 8, 2022 with the force vector inferred from the modeling of the waveforms. Note: force vector has been placed manually near the calving front of Hektoria Glacier for visual clarity; B) the bandpass-filtered (20-50s) observed (black) and synthetic (red) waveforms from a grid search for horizontal force magnitude and direction; C) variance reduction.

Event Arrival Time @LPLY	Peak Force	Azimuth
Nov-6-2022 20:08:32	3.5 X 10^9 N	164
Nov-6-2022 20:49:31	6.1 X 10^9 N	-170
Dec-12-2022 06:02:58	2.1 X 10^{10} N	168
Dec-12-2022 13:15:14	8.6 X 10^9 N	172
Dec-19-2022 05:59:45	1.37 X 10^{10} N	170
Dec-25-2022 17:19:25	1.9 X 10^{10} N	174

Table A2-S1: Event times and estimate force magnitudes and directions for the 6 observed GEQs that we observed to originate from the Hektoria Glacier region.

*We report event arrival time at station LPLY since it is the closest station to the source location(s) of the GEQs for which the seismic arrival is clearly observed for all events.

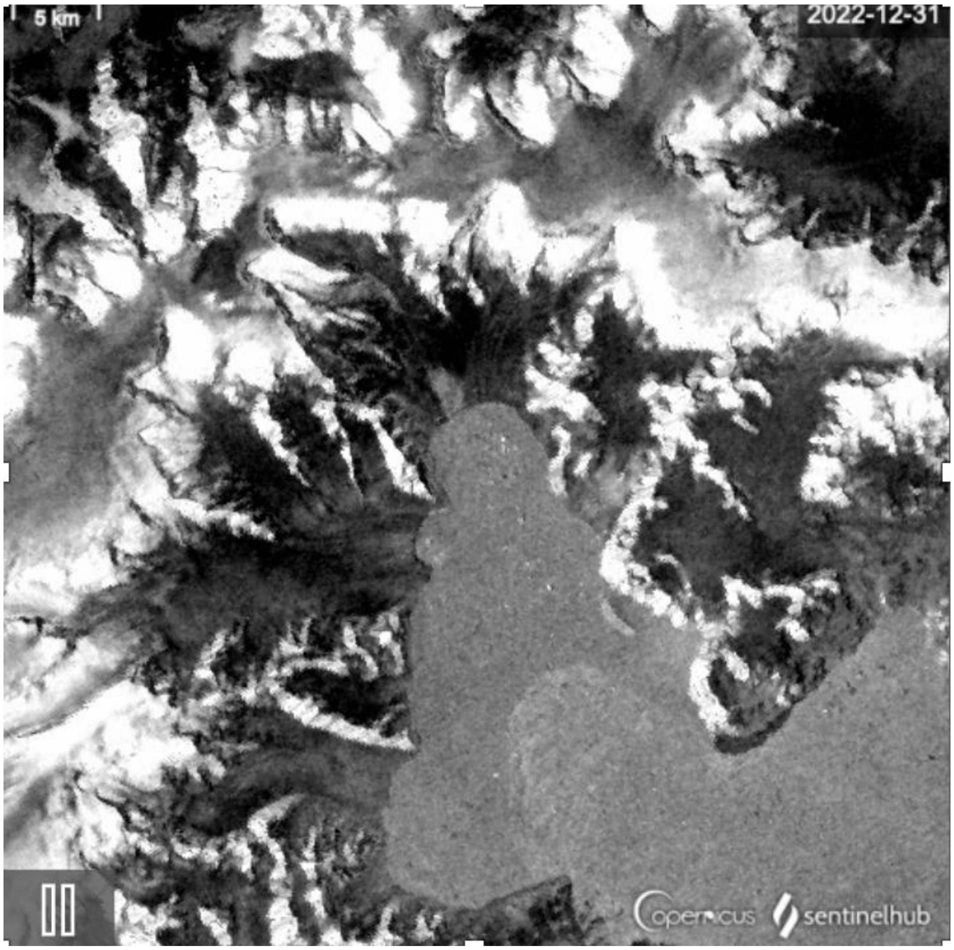

Supplemental Video 1: Timelapse of Sentinel 1 SAR orthorectified S1_AWS_EW_HH imagery from January 2022 to April 2024. Video available upon request.

Supplemental Video 2*:* GoPro footage of Hektoria Glacier reconnaissance flight February 26th 2024 courtesy of Captain Franco Saravalli. Video available upon request.